NATURAL CIRCULATION HEAT TRANSFER IN FLIBE SALT

by

Karl R. Britsch

A dissertation submitted in partial fulfillment of
the requirements for the degree of

Doctor of Philosophy
(Nuclear Engineering and Engineering Physics)

at the

UNIVERSITY OF WISCONSIN–MADISON

2020

Date of final oral examination: December 10th, 2020

The dissertation is approved by the following members of the Final Oral Committee:

Mark Anderson	Assistant Professor	Mechanical Engineering
Kumar Sridharan	Professor	Engineering Physics
Riccardo Bonazza	Professor	Engineering Physics
Gregory Nellis	Professor	Mechanical Engineering
Mario Trujillo	Professor	Mechanical Engineering

EXECUTIVE SUMMARY

Increasing demand for carbon-free electricity to fight global climate change is driving the design of high-temperature nuclear reactors. Several leading designs, like the Fluoride-salt-cooled High-temperature Reactor (FHR), use molten salts because of their unique high-temperature properties. These have the potential to increase safety margins, decrease costs, improve efficiency, and allow flexible plant designs for many different applications. However, there is limited experience working with molten salts after experiments were discontinued in the late 1970's. As new materials, instruments, and experimental methods are developed, there is a growing knowledge gap between modern aspirations and historic data.

To help refresh and expand our knowledge of molten salts, this work designs, operates, and decommissions the University of Wisconsin - Madison (UW) Natural Convection FLiBe Loop (NCFL). As the first halide salt loop in over 40 years, this experiment builds on the seminal corrosion work of the Molten Salt Reactor Program.These historic experiments were driven by natural circulation (NC) loops that tested fuel salts derived from the mixture $2LiF - BeF_2$, called FLiBe. Modern work is considering pure FLiBe and by testing this mixture in the NCFL, this work combines a key historic test-bed with modern designs and measurements. There are 80 thermocouples, two electrochemistry probes, and six fiber optic strain sensors that have never been deployed in salts before. Together, these measurements illuminate the unique NC flow behaviors inside a high temperature flow field under several boundary conditions. Measurements are compiled in a database to aid future simulation or modeling efforts.

A crucial modeling area is the heat transfer behavior of FLiBe. Historic work suggests that salts will behave like "normal fluids," indicating they are similar to water or oil. However, the challenges of working with molten salts leave many uncertainties that require further examination. This work attempts to verify historic heat transfer findings in FLiBe under several boundary conditions. A horizontal air-cooler is used to study heat transfer from freezing salt; highlighting the challenges of accurately measuring wall temperatures. Radiant-mode heaters are used to measured horizontal and vertical heat transfer, proving these rugged, off-the-shelf heaters are capable of decent heat transfer measurements. Improvements were possible using custom strip-heaters that replaced the radiant-mode heaters in later testing. These permit more

accurate surface temperature measurements and reduced heat losses, while also proving to be reliable for long duration testing.

Experimental data from all of these configurations shows that $2LiF - BeF_2$ (FLiBe) has good heat transfer performance and is well predicted by developing flow correlations. Horizontal conditions are also influenced by mixed convection that destroys laminar temperature gradients and mixes the flow. Fiber sensors contrast this mixing with the large temperature gradients in vertical conditions, where mixing is limited. The predominate developing-flow behavior however shows how the closed NC loop can act a forced-convection system, which greatly simplifies heat transfer predictions.

Across several years of testing, results also show a puzzling time dependent behavior that cannot be fully explained. Impurities may play a role; however, metallic impurities only show a strong temperature dependence but no major trends over time. Ultimately the loop is decommissioned, revealing crystal growth inside several legs that may have obstructed flow. These unexpected growths warrant further materials analysis that is ongoing at the conclusion of this work.

ACKNOWLEDGMENTS

In preparing this document, I have been forced to admit that it will always be incomplete. I can only hope to record as much of my experience as possible, with as few errors or typoes as possible.

The reason for this, is that the work recorded here is the result of effort from many people, to whom I owe a sincere debt of gratitude. First, I wish to thank my advisor, Dr. Mark Anderson for giving me this opportunity; and for putting up with me. I also wish to thank Dr. Kumar Sridharan for allowing me to work with many of his wonderful students, including several of my predecessors and co-conspirators.

It is these previous students who I am indebted to for their part in establishing the labs and techniques I rely on. This includes Kieran Dolan, Tony Zheng, Thomas Chrobak, and especially Brian Kelleher – who purified the first batch of salt for this experiment. Those who will continue this work also provided significant assistance and I relied heavily on support and insights from several fellow students including William Doniger, Cody Falconer, Shaun Aakre, Jordan Rein, and Ian Jentz. I especially appreciate all of you who fielded the boneheaded questions and inevitable shenanigans that arise after long isolation in the lab.

Of course, for all the time I spent in the lab, no one works harder than Paul Brooks. I am deeply thankful for his engineering and salt acumen that were vital to this project. I can only hope to retain a small fraction of what he taught me, and I must apologize for the hair he lost on my behalf.

Beyond this, many more people are involved in such a project, to whom I am also very grateful. This includes the faculty and staff of the University of Wisconsin - Madison who have introduced me to so many interesting topics. It includes my friends and family who have made these past five years so wonderful. And it especially includes Emily Roemer, who has put up with all of my late nights and long writing sessions.

Finally, none of this would have been possible without the financial support of the US Department of Energy who started this as an Integrated Research Project `DE-AC07-05ID14517 & DE-NE0008285` and continued funding work under a Nuclear Energy University Program award `DE-NE0008680`. Additionally, the US Nuclear Regulatory Committee graciously supported my schooling through a graduate student fellowship `NRC-HQ-84-15-G-0040`.

Thank you all for your support.

CONTENTS

LIST OF TABLES

LIST OF FIGURES

ABBREVIATIONS

AC . . . . . alternating current

ANP . . . . . Aircraft Nuclear Propulsion

ARE . . . . . Aircraft Reactor Experiment

Be . . . . . beryllium

CFD . . . . . computational fluid dynamics

Cr . . . . . chromium

DC . . . . . direct current

EES . . . . . Engineering Equation Solver

EIA . . . . . U.S. Energy Information Administration

Fe . . . . . iron

FeCrAl . . . . . Iron-Chromium-Aluminum alloy

FHR . . . . . Fluoride-salt-cooled High-temperature Reactor

Gen IV . . . . . Generation-IV

GIF . . . . . Generation-IV International Forum

ICP-MS . . . . . inductively coupled plasma mass spectrometry

ICP-OES . . . . . inductively coupled plasma optical emission spectrometry

Li . . . . . Lithium

MSBR . . . . . Molten Salt Breeder Reactor

MSR . . . . . Molten Salt Reactor

MSRE . . . . . Molten Salt Reactor Experiment

NC . . . . . natural circulation

NCFL . . . . . Natural Convection FLiBe Loop

O&M . . . . . Operation and Maintenance

ORNL . . . . . Oak Ridge National Laboratory

ΔP_l . . . . . loop-wide pressure drop

PPE . . . . . personal protective equipment

RMS . . . . . root mean squared

SAM . . . . . System Analysis Module

ΔT_l . . . . . loop temperature drop

TC . . . . . thermocouple

UCB . . . . . University of California, Berkeley

UW . . . . . University of Wisconsin - Madison

$\bar{v}$ . . . . . velocity estimate

NOMENCLATURE

Symbols

A	Surface area	m^2
c_p	Heat capacity	$J/(kg\,K)$
D	Tube diameter	m
h	Heat transfer coefficient	$W/(m^2\,K)$
k	Thermal conductivity	$W/(m\,K)$
L^*	Dimensionless position $= 1/Gz$	
$\dot{m}$	mass flow rate	kg/s
P	Pressure	W
Q	Heat	W
R	Heat transfer resistance	K/W
T	Temperature	$°C$
t	time	s
v	Velocity	m/s

Greek Letters

Δ	difference between locations	
δ	difference over time	
ϵ_{rad}	Surface emissivity	
μ	Dynamic viscosity	$Pa\,s$
η	Total uncertainty	
ρ	Density	kg/m^3
σ	standard deviation	
σ_B	Stefan-Boltzmann constant	$5.67 \cdot 10^{-8}\,W/m^2/K^4$

Dimensionless Numbers

Gr	Grashof Number	$Gr = \frac{\vec{g}\beta\rho\,(T_w - T_s)\,D_i^3}{\mu_w^2}$
Gr*	Modified Grashof	$Gr^* = \frac{D_i^4\beta\rho^2 g\,Q''}{\mu_w^2\,k}$
Nu	Nusselt Number	$Nu = \frac{hD_i}{k}$
Pr	Prandtl Number	$Pr = \mu c_p/k$
Ra	Rayleigh Number	$Ra = GrPr$
Ra*	Modified Rayleigh	$Ra = Gr^*Pr$
Re	Reynolds Number	$Re = \frac{\rho VD}{\mu}$
Ri	Richardson Number	$Ri = \frac{Gr}{Re^2}$

Superscripts

$\hat{\square}$	Normalized difference $(X_2 - X_1)/X_1$
$\bar{\square}$	Position averaged value

Subscripts

a	Air property
AC	Located in the annular cooler
BC	Located in the bottom cross
i	An inner radial position
K	Temp in Kelvin for radiation heat tranfser
L	At the full tube length
n	A counter
o	An outer radial position
R	Located in the riser
rad	Radiation heat transfer property
s	Salt property
w	Property at the wall

1 INTRODUCTION

Addressing the growing threat from climate change requires increasing production of carbon-free electricity. And while growing solar and wind generation show promise, the 2017 U.S. Energy Information Administration (EIA) statistics show them far behind the world's power demand, supplying only 1% and 3.4% respectively [1]. Most carbon-free electricity is generated with hydroelectric or nuclear power, which together provide 16.3 % of demand. Adding localized sources like geothermal pushes the world-wide combined "green energy" category almost reaches a quarter of the world's electricity supply.

In the US a similar picture has a bleak forecast. Most of our carbon free energy is provided by nuclear power, which over the last 20 years has supplied 19 to 20 % of all US electricity [2]. The remainder is mostly supplied by coal or natural gas, which in 2019 produced a combined 2550 GWh [3]. Replacing this much carbon-intensive electricity is no small task. And it faces many challenges, including grid operators wary of adding 'to much' wind or solar generation, and a distribution network designed for large centralized plants [4], [5].

Given the challenges and rapid pace of climate change, transition away from carbon-intensive energy requires the use of nuclear power, and possibly more of it. However, the US is currently losing its biggest source of carbon-free power. From a peak of 110 reactors, the industry now has only 95 operating with several looming shutdowns [6], [7]. As a result, the EIA predicts nuclear generation in the next two decades will plummet by 20 % [8].

The decline of nuclear power at such a crucial time is due to many complex factors [9], [10] and there are several attempts to address it. One major effort is lead by the Generation-IV International Forum (GIF), which selected six reactor types that are considered best-suited for future development [11], [12]. Merits like safety, proliferation resistance, and technological readiness promise to reduce risks worldwide. However, electricity markets have shifted over the past two decades and many Generation-IV (Gen IV) concepts struggle to compete with mass-produced, compact, high-temperature natural gas plants.

As Gen IV concepts have struggled, the Molten Salt Reactor (MSR), one of the lesser known designs, has recently become a lead candidate for future development. Following an initial revival at universities and national labs in the early 2000's [13]–[19] private industry is now

developing several molten salt reactor designs [20]–[25]. There are a wide range of concepts, including burners and breeders, fissioning uranium or plutonium, with fast, epithermal, or thermal neutrons so they can generate anywhere from 10's to 1000's of *MW* of electricity with either Brayton or Rankine power cycles.

1.1 Overview of Molten Salts

The flexibility, and thus popularity, of molten salt reactors is derived from their namesake fluid. At their most basic, molten salts are just ionic-liquids, with possible types including carbonates, nitrates, chlorides, and fluorides. Halide salts form particularly strong bonds, especially with reactive metal like lithium, that ensure stability and lend fluoride salts their unique properties. These include high melting temperatures, low vapor pressures, large heat capacities, minimal reactivity with air or water, and maximum temperatures that often exceed 1000 °C [14], [26]. In practical terms, these translate to small, high temperature systems operating at atmospheric pressure without stored chemical energy that could be unleashed if exposed to air or water.

Many applications can benefit from these properties, like fuel reprocessing [27], [28], refining or heat-treating metals [29], [30], and concentrated-solar power plants [31]–[33]. However, the defining role of molten salts takes further advantage of their unique chemistry to build a liquid-fuel nuclear reactor [34], [35]. There are several excellent histories [34], [36] and an extensive document archive that trace the more than 40 years of MSR development at Oak Ridge National Laboratory (ORNL). Summarized, work began in late 1940's when halide salts were first selected for use in a nuclear propelled airplane. This required a high-temperature, lightweight, compact, and rugged power plant where molten salts excelled. Their strength was dissolved uranium fuel that deposited fission energy directly into the heat transfer fluid. To prove it, the ground-based Aircraft Reactor Experiment (ARE) demonstrated molten salt fission power in 1954. The test showed great promise for the reactor, but not the plane, which was never built. Luckily, designers grounded their dreams and work shifted to a civilian project that successfully tested the Molten Salt Reactor Experiment (MSRE). This 1965 test further demonstrated the versatility of molten salts; so much so that it is the foundation of many modern concepts. At the time, the MSRE successor was to be the Molten Salt Breeder Reactor (MSBR); a

large central power plant fueled with a thorium-uranium cycle. Unfortunately, this was never constructed before US salt research ended in 1976.

This brief summary highlights a crucial feature of historic work: molten salts were not selected for heat transfer but for their chemistry. This was less about dissolving uranium and more about dealing with the resulting fission products, which only include every other element. While completely dissolving all elements is impossible, salts do a pretty good job at dissolving some of everything.[1] But modern reactors don't need to fly and they may not need liquid fuels either. The recent development of TRISO greatly increases the maximum allowable fuel temperatures, while computer simulations continually improve and simplify hot-spot predictions. Since liquid fuels face several other challenges, like movement of delayed fission precursors [38], recent work is considering using molten salts only for heat transfer.

1.2 Research Overview

The development of salt-cooled reactors has given birth to a new reactor class called the Fluoride-salt-cooled High-temperature Reactor (FHR) [16], [39], [40]. And this, has given rise to many questions about the behavior of pure salts[39]–[41]. Of the quandaries, this thesis concentrates on heat transfer as it follows the construction, operation, and decommissioning the University of Wisconsin - Madison (UW) Natural Convection FLiBe Loop (NCFL). This versatile test bed is designed to couple historic work and modern concepts; starting with a layout similar to the MSBR corrosion loops. The loop also tests $2LiF - BeF_2$ (FLiBe), which was a popular starting point for the MSRE and MSBR fuel salts. Unlike most historic systems however, the NCFL uses 316 Stainless Steel, which is a common in modern nuclear applications and is under consideration for the FHR [42].

A final break from precedent is the instrumentation, because in seeking to revitalize salt work, the NCFL tests several modern instruments and methods for molten salt research. Instruments like fiber optic temperature sensors are deployed for the first time in salts. Building on past work, two generations of electrochemistry probes and two salt sampling mechanisms are tested in flowing salts for the first time in decades. A time-of-flight velocimetry method is researched, with general application to many low pressure drop systems. And the performance of custom

[1] Strong acids can do this, as demonstrated by the gold-plated LAPRE reactors that used pressurized sulfuric acid. However, boiling limits the maximum temperature [37].

strip-heaters are compared to off-the-shelf radiant heaters, showing promise for both methods. All of this work is described in Chapter 3. Measurements are collated in Section D.1 to aid future modeling and simulation efforts with codes like System Analysis Module (SAM) [43].

Focusing on the thesis topic, this work measures heat transfer in FLiBe, anticipating the data will agree with standard mixed convection correlations. Chapter 4 describes calculations for the three NCFL boundary conditions: convection cooling, radiant-mode heating, and conduction-mode heating. Because of the Prandtl Number (Pr), FLiBe has long development lengths but a literature review in Chapter 2 shows that it should be readily predicted as a normal fluid. The influence of mixed convection however complicates the analysis and horizontal flow through the annular cooler and bottom cross heater have elevated heat transfer relative to the vertical riser. Chapter 5 discusses the heat transfer results and notes a few inexplicable phenomena, including a surprising time dependence. This leads to further impurity analysis and a visual inspection of the loop interior after in Chapter 6.

2 MOLTEN SALT HEAT TRANSFER

Molten salt heat transfer is a relatively new study, largely occurring in the mid to late 1900's. Recent planning for several large-scale experiments has revived halide salt work, using both fluoride and chloride salts, but as of this writing, recent experiments focus on nitrate salts. This forces halide salt work to build off historic experiments in system design heat transfer.

Several reviews cover portions of the historic work [14], [26], [44], [45] and all assert that salts will behave as "normal fluids." This shorthand indicates their nondimensional heat transfer characteristics will be identical to other common fluids, like water or oils. Historic data largely support this conclusion; although a modern recalculation is required for some experiments. Hidden among these reports however is a rich history of experiments that do not quite appear "normal." Often, this is due to physical property errors but in some cases there is not enough data to drawn many conclusions. Overall, there is no history that covers all of these results despite the relative youth of the field that makes this entirely possible. And since minor details of experimental work are often critical to success and because many specialists are no longer working, this work thoroughly reviews historic heat transfer experiments. In text, detailed citations provide access to source material for both well-regarded and poorly understood results while the results are compiled into Summary Tables 2.1 and 2.2.

2.1 Established Heat Transfer Studies

From modern literature, there several experiments that seem to have reached a consensus opinion of reliability and accuracy. These are widely reviewed by many authors and concern two halide salts: pure $LiF-NaF-KF$ $(46.5-11.5-42.0\ mol\%)$ $(FLiNaK)$ and several $FLiBe$-based fuel salts.

FLiNaK Studies

MSR Programs

$FLiNaK$ was one of the earliest salts studied during the Aircraft Nuclear Propulsion (ANP) Project, with an initial intention of adding 1 to 3 $mol\%$ UF_4 and confining the salt inside fuel pins[1]. This application required strong natural circulation (NC) characteristics and fluoride

[1] Moltex Energy has revived this fuel-pin concept for their Stable Salt Reactor [23].

salts were hypothesized to act as normal fluids, likely based on their Pr [46].

This expectation was promptly questioned by the first experimental results from Hoffman and Lones in 1952 using pure FLiNaK. The experiment used gas pressure to push salt between two Inconel® pots through a horizontal test section. Heat was provided by "direct heating;" where low-voltage alternating current (AC) current ran through the tube wall. Temperatures were measured by surface mounted thermocouples (TCs) along the test section while fluid temperatures were taken in the mixing chamber at each end. To cover a range of heat fluxes, three different materials were used for the test section: nickel, Inconel®, and 316 SS. Larger heat fluxes in 316 SS and Inconel® test sections allowed higher flow rates, extending across $Re = 2000$ to 10 000.

Unexpectedly though, each material produced different results. Nickel and 316 SS were close to the predictions of the Chilton-Colburn Relation, despite Reynolds Number (Re) falling in the transition regime [47, pg 180]. Inconel® on the other-hand fell below the Colburn predictions by 50 to 60 % [48, pg 100] .

Around the same time, work by Grele and Gedeon observed a similar offset in their FLiNaK data [49]. This pumped experiment also pushed FLiNaK though a horizontal test section under direct heating, except their entire loop was constructed from Inconel-X®. Testing over $Re = 2000$ to 20 000, their data also follows the predicted trend but is again offset 60 % below predictions of the McAdams[2] correlation.

Neither Hoffman and Lones nor Grele and Gedeon could explain the offset. In their 1955 report, Hoffman and Lones suggest it was the result of either a heat transfer resistance or physical property errors [50]. If properties were at fault, the Inconel® data would align for thermal conductivity (k) were $1.6\,W/(m\,K)$ instead of $4.5\,W/(m\,K)$, or if the viscosity was $8.3 \cdot 10^{-6}$ rather than $4.5 \cdot 10^{-3}$ Pa s. At the time, this was considered unlikely since some of the other data aligned and because remeasured properties agreed with accepted values [3] [51, pg 91].

Instead, Hoffman and Lones identified a heat transfer resistance in the form of a thin $\leqslant 10\,\mu m$ green film. This uniform covering, shown in cross section in Fig. 2.1, coated the inside of at least one of the two Inconel® test sections [52, pg 107] and consisted primarily of K_3CrF_6.

[2] heated Dittus-Boelter

[3] It is unclear if they measured a dirty salt sample from their experiment or a clean sample.

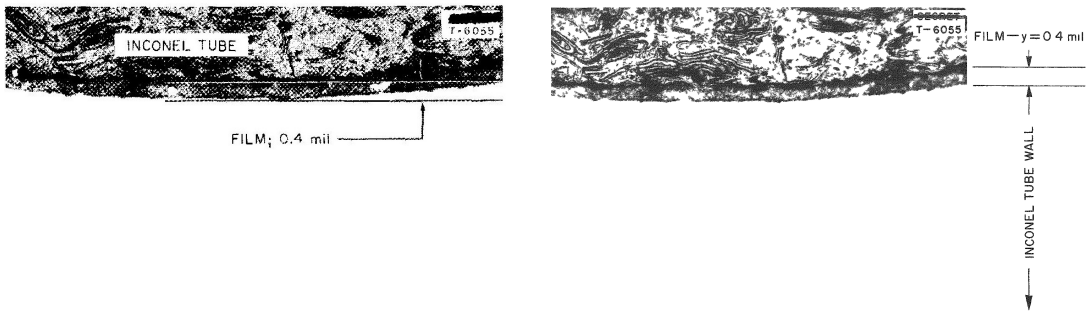

Figure 2.1: What appears to be the same image of the resistive FLiNaK film. The left image is from ORNL report 1771, in Sept 1954 [53, pg 130] while the right is from the published paper in February 1955 [50, pg 26].

Subsequent work found this compound was insoluble in FLiNaK with a melting point above the test conditions [50, pg 24]. Additionally, it has a low thermal conductivity of $0.22\,W/(m\,K)$, which is more than sufficient to correct the errant Inconel® data. To verify their hypothesis, Hoffman and Lones submerged an electrified Inconel® and nickel tube in FLiNaK overnight. In the morning, they found a film growing only on the Inconel® tube [52].

Attempts to reproduce this experiment at UW were unsuccessful and retrospectively, modern literature claims such fluoride films are unlikely. A review by Holcomb and Cetiner blames the strong fluxing ability of fluoride salts, although this is more applicable to oxide-based films [26].

At the time however, there was more debate. Hoffman and Lones even state: "[t]hese corrosion products are typical of those found when KF- and LiF-bearing fluoride mixtures are contained in Inconel" [51, pg 91]. Without a citation it is unclear what "typical" results are being referenced, and this contradicts findings from Grele and Gedeon. Their testing verified the pumped loop with water both before and after salt exposure with good agreement between results and predictions. A minor deviation was present at high Re, which may have resulted from the thin scale found by visual inspection of the inside of the test section after the final water experiment. This scale was not green, and far to thin to account for the 60 % discrepancy, leaving the results in doubt as ORNL transitioned to zirconium based salts for the Aircraft Reactor Experiment (ARE).

Vriesema

Over the next several decades, work at ORNL improved their heat transfer measurements, using other salts. The next FLiNaK experiment in the English literature wasn't until 1979 at TU Delft by B. Vriesema. This thesis explored several aspects of a pumped FLiNaK loop, including thermal pulse velocimetry and pressure drop [54]. Regarding heat transfer, the loop included a counter flow concentric tube air cooler that was likely constructed from a 1 1/2" NPS schedule 40 Inconel® pipe. The large diameter increased Re over 13 000 to 93 000 at the cost of salt temperature drop, which was often only a few °C. Despite the experimental challenge, 33 data points clearly depict a Dittus-Boelter-like trend that is 17 % below predictions. Examining causes, Vriesema found the offset from predictions could be explained if the salt's thermal conductivity were lowered from 1.3 to 1.03 $W/(m\,K)$.

Ignatev

Following this in 1984, work at Russia's National Research Center by conducted by Ignatiev et al. [55], provides the only heated experiment with upward flowing FLiNaK. Unlike previous experiments, this work includes a calming length of $l/d = 20$ prior to the test section. The study also wrapped an electric strip heater around the tube instead of directly passing current through the tube wall. Further differing from previous FLiNaK work, the results are in near perfect alignment with predictions at $Re \geqslant 10\,000$. Below this, the Petukhov-Kirillov correlation requires a transition correction but retains the data within 90 % of predictions down to $Re = 5000$.

Review by Ambrosek et. al.

Together, these four experiments were reviewed in 2009 by Ambrosek et al. [44] who noted a wide range of thermal conductivity (k) across the decades. The latest work by Ignatiev et al. used k measurements from Smirnov et. al. [56] that are still recommended today, with $k = 0.81$ to 0.93 $W/(m\,K)$. Vriesema's calculations were slightly higher, while ORNL was about $\approx 4\times$ larger.

Ambrosek et al. therefore recalculated the Nusselt Number (Nu) from the reported data using a modern k value, and found that almost all results agree with the Dittus-Boelter correla-

tion to within 10 % over $Re = 2000$ to 93 000. Two discrepancies are present for the early nickel and 316 SS test sections, with data now elevated above predictions up to double. Additioanlly, Vriesema's data technically aligns slightly better for $k = 1$ but the 8 % difference with Smirnov's k value is within uncertainty for the Dittus-Boelter correlation. Data from Ignatiev et al. was not available for correction; however, their already close results use the same k as Ambrosek et al., so change is unlikely. Therefore, taken as a whole the data alignment strongly refutes any evidence of insulating films or of unexpected material interactions with Inconel®.

Beryllium Salts

MSR Programs

In addition to agreeing with correlations, Ambrosek et al. finally corrected the FLiNaK data to align with later ORNL beryllium fuel salt results. By far the largest experiment was operation of the MSRE itself, which had both a salt-to-salt and salt-to-air heat exchanger. Over several thousands of hours of operation, there was no change in performance indicative of film growth, nor did post operation examination find any heat transfer resistances [26], [57]–[61]. It should be noted that this performance was in spite of incorrect sizing due to an overestimate of salt thermal conductivity. The calculation used a value $3\times$ too large, over-estimating the heat transfer coefficient by around 20% [57, pg 188]. Fortunately, this was within the design tolerance and did not limit reactor power [62].

Dedicated heat transfer tests with fuel salts took place after MSRE concluded, while designing the MSBR. Experiments by Silverman et al. [63], [64] tested two new fuel salts[4] and the coolant $NaBF_4 - NaF$ $(92 - 8$ mol%), (Sodium Fluoroborate) inside a pumped corrosion loop. Around the same time, Cooke and Cox [65] revived tank transfer experiments for another a fuel salt[5] in both horizontal and vertical orientations [65]. For all these experiments, the apparatus entirely was constructed from Hastelloy–N [66] and impurity data was tracked for most salts.

Data from these experiments agrees well with predictions [64], [65], which by now accounted for temperature variation in the salt viscosity near the wall. Silverman et al. tested $Re \geqslant 2100$, relying on the Hausen correlation up to $Re = 15\,000$ and above that using turbulent Seider-Tate correlation. Cooke and Cox found similar results over this range and fit the custom correlations

[4] $LiF - BeF_2 - UF_4 - ThF_4$ $(68 - 20 - 0.3 - 11.7$ mol%) and $LiF - BeF_2 - UF_4 - ThF_4$ $(72 - 16 - 0.3 - 11.7$ mol%)
[5] $LiF - BeF_2 - UF_4 - ThF_4$ $(67.5 - 20 - 0.5 - 12$ mol%)

given in Table 2.2. Their data included laminar conditions for the first time, with conclusive results over $Re = 400$ to 1000 that agree with the laminar-Seider-Tate predictions.

Of note is the range of data Cooke and Cox did not study, between $Re = 2000$ to 5000. In this range, results were not repeatable because of a heat flux (Q'') dependence that interrupted flow development. Cooke and Cox determined this was caused by re-laminarizing of the velocity profile $(U(x, y))$ due to the temperature dependence of viscosity [67, pg 67]. In short, this arises when heating imposes a negative curvature on the boundary layer, described by Eq. (2.1) [68].

$$\left(\frac{\partial^2 U}{\partial y^2}\right) = -\frac{1}{\mu(T)}\left(\frac{\partial \mu(T)}{\partial y}\right)\left(\frac{\partial U}{\partial y}\right) \tag{2.1}$$

The temperature profile decreases viscosity near the wall, which stabilizes the boundary layer and encourages laminar behavior. Conversely, this suggests cooling salt will not observe transition flow but instead rapidly become turbulent, explaining the results from Vriesema that agree with the Dittus-Boelter correlation instead of the Seider-Tate.

Ignatyev et al.

The final study of beryllium based salts was a wide ranging study by Ignatiev et al. [69] inside natural circulation (NC) thermosyphons. These small circulation cavities were constructed from nickel or a stainless steel-like alloy and used to test a wide range of fluids, including air, water, and three fluoride salts. When normalized against modified Rayleigh Number (Ra_m) , the data aligns well with predictions within a scatter of $\leqslant \pm 12\,\%$.

Nitrate Salt Work

After the experiment by Ignatiev et al. most recent salt work has studied nitrate mixtures for solar applications. Similar results have been found, arguing for viscosity corrections near the wall and the use of transition flow correlations up to $Re = 10\,000$ [31], [32], [70], [71]. A wider range of experimental conditions have been used with a general emphasis towards higher Re; necessary to counter the low thermal conductivity. A recent example close to historic Re ranges is from Wu et al. [72] for cooled nitrate salts. Over $Re = 4100$ to 9850 the data falls within $\pm 15\,\%$ of the Gnielinski or Hausen correlations. At higher flow rates, covering $Re = 17\,000$ to $45\,000$, better agreement was provided by the Dittus-Boelter or Seider-Tate equations [73].

Contrasting this agreement is a high heat flux study by Das. et al. [71] that found Gnielinski correlation over-predicted data by up to 50 %. Examining an annular heater with up-flowing nitrate salt revealed an unusual heat flux dependence at $q'' \geqslant 1 \cdot 10^6\, W/m^2$ and $Re \geqslant 2.0 \cdot 10^5$. It is possible decomposition played a significant role in the data, but the authors do not discuss this, focusing on a proprietary correlation that is unavailable in literature.

In fluoride salts, no similar Q'' dependence has been observed. Table 2.1 shows heat flux data for several experiments, including Cooke and Cox who tested $q'' \leqslant 1.7 \cdot 10^6\, W/m^2$ [65]. Many more nitrate salt experiments are available, with references [14], [26], [72], [74]–[79] offering a selection of recent experiments. Much of the work focuses on novel geometries, offering further support for standard correlations like the Seider-Tate and Hausen equations.

2.2 Additional Fluoride Salt Work

These well established experiments are the basis for most molten salt heat transfer literature reviews. However, many other experiments are available that may offer insight to different geometries or to what can go wrong with fluoride salt experiments.

FLiNaK Fuel Salts

When fluoride salt work first began, it focused on FLiNaK with the intent of making a uranium containing fuel mixture [80]. In 1955, when property errors were wrecking havoc with pure-FLiNaK studies, the tank-transfer method was used to study heat transfer in the mixture $LiF - NaF - KF - UF_4$ $(45.3 - 11.2 - 41.0 - 2.5\ mol\%)$ flowing through an Inconel® tube. Heat transfer fell below the Colburn relation by 40 % and in line with previous FLiNaK work, the test section's inner surface was again coated in a thin green film. Interestingly, "X-ray and petrographic examination" [80, pg 149] of this layer found only salt constituents but no chromium, contrary to previous findings.

Assuming the Inconel® test section was at fault, a 316 SS tube was tested later that year [81], followed by a Hastelloy–B test section [82]. This time, data from different materials agrees, about 40 % below predictions. Furthermore, the Hastelloy–B test section did not show any evidence of a film or deposits [82, pg 170]. The 316 SS test section was destroyed during testing; however, the researchers reportedly did not believe a film existed. This lead to the tentative

theory that "...the NaF-KF-LiF-UF_4 composition contained particulate matter that made it a dilute slurry" [81, pg 149]. Or, as later stated, heat transfer issue stems from "characteristics of the fluid itself" [82, pg 170].

Zirconium Salt Heat Transfer

Agreement between different materials with fuel-baring FLiNaK supports the theory by Ambrosek et al. that incorrect thermal conductivity is to blame for the offset. Likely the same issue plagues the various zirconium salts used in development of the ARE. The reactor experiment operated in 1955 and, like the MSRE it was not designed specifically for heat transfer but the heat exchanger did operate for 24 days [83] without any issues [81], [82], [84], [85].[6]

Preparation for a scaled-up demonstration aircraft reactor included a series of heat exchanger experiments with a zirconium and beryllium salt.[7] A report in 1958 by Amos et al. [86] and in 1960 paper by Yarosh [87] provide data from a counter flow shell-and-tube Inconel® heat exchanger that cooled the salt with the liquid metal NaK . Salt was tested on both the tube and shell side for over 1000 hours and Yarosh notes there was no change in heat exchanger performance [87].

On the shell side, Nu consistently falls about 40 % below the Dittus-Boelter predictions. This is despite turbulence enhancement from the grid spacers that, Yarosh notes, potentially lowered the transition point to $Re \approx 350$. Inside the tubes, Fig. 2.2 shows the results do not follow the Dittus-Boelter trend but do approach it with increasing Re. The data best aligns with a FLiNaK data fit that is likely from Hoffman and Lones.[8] In that case, there are similar property errors between the two salts and indeed, Amos et al. calculate a better agreement if k were $0.6\,W/(m\,K)$ instead of $2.59\,W/(m\,K)$; a factor of 4.3 . This value is close to the modern recommendations from Holcomb and Cetiner, who estimate pure $59.5NaF - 40.5ZrF_4$ ($NaF - ZrF_4$) has $k = 0.49\,W/(m\,K)$ [26] .

The same zirconium salt was also used in a 1953 tank-transfer experiment.[9] The horizontal Inconel® test section results cover $Re = 5000$ to 10 000 and show familiar correlation trends with an offset of only ≈22 % below the Colburn predictions. There was no evidence of a film [88, pg

[6]The ARE salt was $NaF - ZrF_4 - UF_4$ $(53.2 - 40.5 - 6.3 mol\%)$

[7]"Mixture 30:"$NaF - ZrF_4 - UF_4$ $(50 - 46 - 4\ mol\%)$ and "Mixture 130:" $LiF - BeF_2 - UF_4$ $(62 - 37 - 1\ mol\%)$

[8]It is cited: "Hoffman, H. W. Umpublished [*sic*] Data."

[9]Mixture 30: $NaF - ZrF_4 - UF_4$ $(50 - 46 - 4\ mol\%)$

112] and researchers tentatively proposed the salt may not wet the Inconel® and instead form an insulating gas layer [80, pg 150]. However, friction measurements over $Re = 5000$ to 200 000 were within 16 % of predictions, arguing against any gas film.

Shortly after this, a 1954 paper by Salmon examined a pumped salt loop cooled a zirconium salt[10] with NaK inside a counter flow concentric tube heat exchanger [89]. Component availability forced a Frankenstein creation using Inconel® piping, a used 316 SS pump, and a nickel test section. Inevitably, mass transfer deposited a film inside the nickel test section and by the end of testing Nu had decreased 16 %. Salmon used ΔP measurements to identify un-fouled tests, accepting the earliest 19, of 80, for analysis. Surprisingly, over $Re = 4400$ to 21 000 Nu was within 4 % of the McAdams correlation and a more distant 20 % below the Hausen and Seider-Tate predictions. Considering this study used $k = 1.7$ to $3.5\,W/(m\,K)$ turbulent heat transfer must have minimized the impact of thermal conductivity [90]. Heat transfer must have been enhanced at low-Re, either by the cooling salt viscosity relations discussed with Eq. (2.1) or by initial iron deposits, as suggested by Salmon.

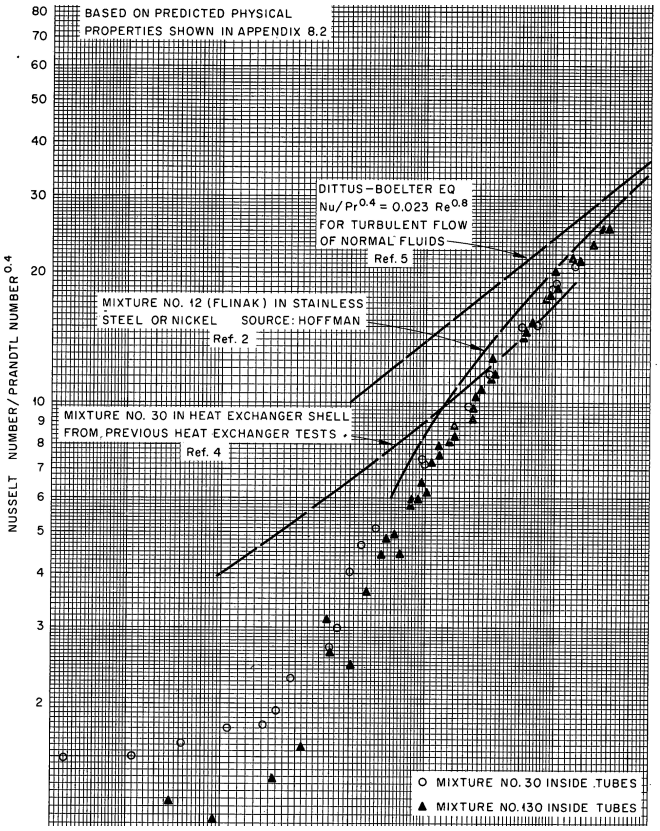

Figure 2.2: Heat transfer in a shell-and-tube Inconel® heat exchanger from ORNL report CNF-58-4-23 by Amos et al. [86, pg 12]

The film itself is interesting.Its thermal resistance was found to be many times larger than calculations predicted [52, pg 109], indicative of a highly porous nature. Furthermore, it does not contain chromium, despite the availability of this element in the Inconel® piping and the 316

[10] Also mixture 30: $NaF - ZrF_4 - UF_4$ (50 − 46 − 4 mol%)

SS pump, which must have supplied the iron. Most mass transfer predictions expect chromium transfer rather than iron, because CrF_2 is energetically favored over FeF_2 [91], [92]. Potentially the used pump had no chromium left, or perhaps the chemistry was so corrosive the chromium remained in solution. Chromium could have plated out elsewhere but unfortunately there is no recorded investigation of components nor is there analysis of the salt chemistry.

Beryllium Salts

Early beryllium salt work was also impacted by properties; however, few heat transfer tests were carried out during the MSRE construction.As previously mentioned, the MSRE heat exchanger was improperly sized due to an over-estimation of k. Luckily the $3\times$ k error was still within the 20 % design tolerance. Another false alarm near the same time came from a pumped bi-metalic loop that initially reported a heat transfer difference between an INOR–8 and Inconel® test section. This was later found to result from an incorrect area calculation [93, p 29] and no subsequent heat transfer differences were found between materials.

After the MSRE heat transfer experiments resumed for the new MSBR salts, as described in Section 2.1. During this time, the tank transfer experiment by Cooke and Cox reported a few exploratory heat transfer studies. Their first examination [61] studied the cover gas, comparing helium and argon.[11] Despite an estimated $10\times$ higher solubility for helium, their data does not show any differences between cover gasses. They next examined vertical orientations and expected to find reduced heat transfer for up-flow and enhanced heat transfer in down-flow. According to their final report [65], the up-flow data agrees with horizontal conditions while down-flow heat transfer is indeed enhanced. Earlier reports [61, pg 88] however claim that systemic errors in fluid temperature measurements affect these results. It is unclear how those were resolved.

Silverman et al. also deviated from strict heat transfer in a chemistry study inside their pumped corrosion loop [12] [94, pg 29]. They made three additions of 1 to 1.6 g of NiF_2 powder into 14 kg of salt.[13] And after each addition, they noticed that returning the loop to its previous flow rate required increased pumping power. In their final addition, this rise was measured from 3.75 kW up to 4.3 kW over three-days.

[11] Using salt $LiF - BeF_2 - UF_4 - ThF_4$ $(67.5 - 20 - 0.5 - 12$ mol%)

[12] During tests of $LiF - BeF_2 - UF_4 - ThF_4$ $(68 - 20 - 0.3 - 11.7$ mol%)

[13] About 4.73 to 7.57 mmol %. 1 mmol % = 10 ppm and clean UW FLiBe has impurities of $\leqslant$30 ppm [95].

After switching to their second fuel-salt,[14] researchers repeated the additions, this time while pump operated [96]. They report: "[i]mmediate pump-power increases of 8 to 10% were again noted with each 0.8-g addition. The salt level in the auxiliary tank decreased with each NiF_2 addition" [96, pg 20]. Interestingly, beryllium additions never caused such issues, despite its viscous nature. Furthermore, there was no change in heat transfer performance, leading researchers to conclude viscosity was not changing. Ultimately, they linked the flow rate change to a 1 % increase in density, driven by rising surface tension. Higher surface tension reduced helium entrainment by the pump and caused the salt level to fall. A higher density also increased drag on the impeller and requiring more pumping power.

Discussion

At this time, there are no similar findings to the NiF_2 deviations observed by Silverman et al. Excluding that and the elevated heat transfer for nickel and stainless in Ambrosek et al. recalculation, historic literature shows that molten salts are well predicted as normal fluids. There is no need for resistive film corrections or slurry-like behavior adjustments. Uncertain property measurements continue to plague many design calculations; however, several reviews recommend similar values without finding any impact from impurities and sources state that fluoride salts are Newtonian fluids [26], [97].

2.3 Heat Transfer in the NCFL

Translating this to the NCFL, heat transfer should follow standard correlations. Cooling salts can likely rely on the Dittus-Boelter equation above $Re \geqslant 2100$ while heating requires a transition correlation over $2100 \leqslant Re \leqslant 10\,000$. Laminar conditions should also be simple to predict; although at this time the only available data is for heated salt from Cooke and Cox, discussed in Section 2.1. This correlates against the laminar-Seider-Tate equation instead of a constant Nu.

Flow development

The NCFL however, is unlikely to exceed $Re = 1000$, placing emphasis on the lower Re data. In laminar conditions, flow development plays a crucial role in heat transfer, and the high Pr of $FLiBe$ ensures a long development length. This can be measured with the the Graetz Number

[14] $LiF - BeF_2 - UF_4 - ThF_4$ $(72 - 16 - 0.3 - 11.7\ mol\%)$

(Gz), which falls as flow develops, or the the Invervse Graetz Number (L^*) that grows along the flow path [98]. In the NCFL, flow will exit most legs with $L^* \approx \mathcal{O}(0.01)$, which approaches fully developed flow. For these conditions, a correlation Shah and London to constant Q'' data from Hornbeck [98] will be used. As flow develops, it trends towards the constant $Nu = 4.36$ but at the NCFL conditions it predicts $5 \leqslant Nu \leqslant 10$.

A second challenge in predicting NCFL heat transfer arises from the lack of any external driving pressure gradient. Instead of a pump, NC flow arises "naturally," driven by density differences between hot and cold fluid when a heat source is located below the cooler. This configuration causes light hot fluid to rise, while cold fluid sinks. Visualizing this is simple but analyzing it can become fiendishly challenging because of coupling between temperature and flow rate. For NC flow to arise, there must be a loop temperature drop (ΔT_l), which sets the density difference and flow speed. However, flow rate determines how long salt will exchange heat and therefore, flow speed impacts ΔT_l.

In the worst case, this coupling can lead to instabilities that include chaotic phenomena and flow reversal [99]–[104]. However, the NCFL is designed to avoid these by sloping the horizontal legs along the flow direction and heating the riser. A bigger issue is coupling's impact on computer models, which become very sensitive and may not converge.

Mixed convection

To further complicate analysis, the NCFL is expected to operate in the mixed convection heat transfer regime. This occurs when both forced and natural convection equally contribute to the flow field. Forced flow is characterized by the ratio of inertia to viscosity, captured by Reynolds Number (Re), while natural convection uses the Grashof Number (Gr) to compare buoyancy and viscosity. However, a NC loop relies on both of these phenomena making it difficult to fully describe the flow environment. The the Richardson Number (Ri) provides one description through the ratio Gr/Re^2, which trends to an extreme when one force or the other dominates. At Ri $\mathcal{O}(1)$, flow is in mixed convection and both forces are equal. This is where NCFL should operate.

Predicting mixed convection depends on orientation. In the bottom cross, flow is perpendicular to gravity and small-scale NC cells rise across the flow and increase heat transfer from the

lower wall [105]–[108]. The mixing reduces development lengths as shown by Meyer and Everts [109]–[111]. According to their flow maps, the NCFL heating rates may cause sufficient mixed convection for turbulent flow; granting short development lengths and increased heat transfer. Another horizontal mixed convection study by Morcos and Bergles includes a wall conduction term to account for internal circulation from the lower wall [107]. This study predicts even higher heat transfer than Meyer and Everts and is far above Shah and London.

By contrast, in vertical heated up-flow wall temperatures are symmetric and heat transfer can decrease in some conditions [105], [112]–[114]. The difference is that gravity accelerates the hot fluid near the walls relative to the colder core. This deforms the velocity profile into an "m" shape that traps hot salt near the walls and decreases heat transfer [112], [113]. With enough viscosity however, the slower core will shear eddies of salt away from the wall, increasing mixing and enhancing heat transfer.

A review by Jackson et. al. [112] indicates the NCFL should see elevated Nu, based on the high power input. Two correlation are provided, one accredited to Martineli and Boelter that relies on wall temperatures through Gr, and another from Hallman that relies on Q'' through the modified Grashof Number (Gr^*). A study by Aicher and Martin also predict elevated heat transfer in the NCFL, based on the term L/D [113]. However, their flow maps predict the NCFL will operate near a transition point and it is possible for laminar conditions to dominate rather than mixed-turbulent. In that case, heat transfer enhancement will not occur and behavior should revert to the correlation from Shah and London.

Table 2.1: Summary of fluoride salt heat transfer experiments.

#	Reference	Salt	Dimensions	q'' $[kW/m^2]$	Notes
1	Hoffman [50]	$LiF - NaF - KF$	ID = 2.9 mm, L/D = 204	73 to 604	Nickel tube
2	Hoffman[50]	$(46.5 - 11.5 - 42 mol\%)$	ID = 4.29 mm L/D = 137	28 to 540	Inconel tube
3	Hoffman[50]	" "	ID = 4.57 mm, L/D = 133	252 to 669	316 SS tube
4	Vriesema[54]	$NaF - LiF - KF$ $(11.5 - 42 - 46.5 mol\%)$	$D_{Friction}$ =41.25 mm		Air cooled, D_{Salt} in HX not given.
5	Ignatiev et al.et. al. [55]	$NaF - LiF - KF$ $(11.5 - 42 - 46.5 mol\%)$	ID = 30 mm, L/D = 60	30 to 60	first $L/D \leqslant 20$ unheated
6	Hoffman[115]	$NaF - ZrF_4 - UF4$ $(53.5 - 40 - 6.5 mole\%)$	ID = 4.57 mm, L/D = 47		Heated in Inconel®
7	Salmon [89]	$NaF - ZrF_4 - UF4$ $(50 - 46 - 4 mole\%)$	ID = 6.83 mm L/D = 40	1113 to 2750	NaK cooled; mass transfer issues.
8	Amos [86]	$NaF - ZrF_4 - UF_4$ $(50 - 46 - 4 mol\%)$	ID = 3.5 mm, L/D = 537	25 to 660	NaK in HX shell. 25 tubes square array, Pitch/OD = 1.165
9	Amos [86]	$LiF - BeF_2 - UF_4$ $(62 - 37 - 1 mol\%)$	ID = 3.5 mm, L/D = 537	168 to 725	NaK in HX shell. 25 salt tubes in square array, , Pitch/OD = 1.165
10	Feb. 1961 Report [116, p. 141]	$LiF - BeF_2 - ThF_4 - UF_4$ $(67 - 18.5 - 14 - 0.5 mol\%)$	L/D = 60	$L/D > 40$	Pumped, I^2R heating. Incorrect fluid properties
11	Cooke [65]	$LiF - BeF_2 - ThF_4 - UF_4$ $(67.5 - 20.0 - 12.0 - 0.5 mol\%)$	ID = 4.57 mm L/D = 136		Tank transfer, I^2R heating
12	Cooke [65]	$NaF - NaBF_4$ $(8 - 92 mol\%)$	ID = 4.57 mm L/D = 136		Tank transfer, I^2R heating
13	Silverman[64]	$LiF - BeF_2 - ThF_4 - UF_4$ $(72 - 16 - 11.7 - 0.3 mol\%)$ & $NaBF_4 - NaF$ $(92 - 8 mol\%)$	ID = 10.5 mm, L/D = 167†	136 to 630	Pumped loop, I^2R heating
14	Ignatyev [69]	$LiF - BeF_2 - ThF_4 - UF_4$ $71.7 - 16 - 12 - 0.3 mol\%$	ID = 36.3 mm, $L_{hot}/D = 5.6$, $L_t = 358$ mm	constant q"	No insert.
15	Ignatyev [69]	$NaF - NaBF_4$ $8 - 92 mol\%$	ID = 40.2 mm, $L_{hot}/D = 6.6$, $L_t = 502$ mm	constant q"	No insert.
16	Ignatyev [69]	$LiF - BeF_2 - UF_4$ $66 - 34 - 0.01 mol\%$	a‡ = 10 mm or 11.5 mm, $L_{hot}/a = 52.6$, $L_t = 1.7$	$\leqslant 25$	With insert

† Max value was 331, 167 used due to interrupted heat flux at the center current tap.

‡ Annular gap size. Diameter unknown.

Table 2.2: Summary of results from fluoride salt heat transfer experiments. Numbers correspond to those in Table 2.1

#	Reynolds Range	Correlation	Notes
1	2459 to 5638		Film
2	2779 to 8337	$j = 0.023 Re^{-0.2}$	Film
3	6586 to 9536		Film
4	13 900 to 93 100	$Nu = 0.137 Re^{0.8311} Pr^{0.4106}$	±1.17%
5	5000 to 10 000	$Nu_t = Nu^* (1 - 1000/Re)$	Valid $Re \geqslant 9 \cdot 10^3$
5	10 000 to 15 000	$Nu^* = \frac{Re\, Pr\, (f_{\mathfrak{F}}/2)}{1.0 + 12.7\left(Pr^{2/3} - 1\right)\sqrt{f_{\mathfrak{F}/2}}}$	
		$f_{\mathfrak{F}} = (1.58 \ln(Re) - 3.28)^{-2}$	Petukhov Friction Correlation [117]
6	5000 to 10 000	$j = 0.023 Re^{-0.2}$	Data 22% below
7	4400 to 21 000	$Nu = 0.023 Re^{0.8} Pr^{1/3}$	Data 4% below
8, 9	400 to 8000	$Nu = 0.023 Re^{0.8} Pr^{0.4}$	Valid $Re > 10000$
10	6000 to 25 000	$Nu = 0.00484\, Re^{0.932}\, Pr^{0.4}$	±10%, Inconel® & INOR–8 tubes
	$\leqslant$1000	$Nu = 1.89 \left[Re\, Pr\, (\frac{D}{L})\right]^{1/3} \left(\frac{\mu_b}{\mu_w}\right)^{0.14}$	±6.6%
11, 12	4000 to 12 000	$Nu = 0.107 \left(Re^{2/3} - 135\right) Pr^{1/3} \left(\frac{\mu_b}{\mu_w}\right)^{0.14}$	±4.1%
	$\geqslant$12 000	$Nu = 0.0234\, Re^{0.8}\, Pr^{1/3} \left(\frac{\mu_b}{\mu_w}\right)^{0.14}$	±6.2%
	1500 to 2100	$Nu = 1.86 \left[Re\, Pr\, (\frac{D}{L})\right]^{1/3} \left(\frac{\mu_b}{\mu_w}\right)^{0.14}$	Inconclusive
13	2100 to 15 000	$Nu = 0.116 \left(Re^{2/3} - 125\right) Pr^{1/3} \left(\frac{\mu_b}{\mu_w}\right)^{0.14}$	
	15 000 to 45 000	$Nu = 0.027\, Re^{0.8}\, Pr^{1/3} \left(\frac{\mu_b}{\mu_w}\right)^{0.14}$	
	Rayleigh Range		
14, 15	$7.6 \cdot 10^4$ to $4 \cdot 10^7$	$Nu_r = 0.195 \left(Ra_m \sqrt{\frac{L - l_h}{l_h}}\right)^{0.236} \left(\frac{Pr_c}{Pr_h}\right)^{0.25}$	<12 %, Normalized by radius.
14, 15	$4 \cdot 10^7$ to 10^{10}	$Nu_r = 0.356 \left(Ra_m \sqrt{\frac{L - l_h}{l_h}}\right)^{0.192} \left(\frac{Pr_c}{Pr_h}\right)^{0.25}$	<12 % Normalized by radius.
16	10^3 to $2 \cdot 10^5$	$Nu_a = 0.24 \left[Ra_m \frac{L - l_h}{l_h}\right]^{0.25}$	±10 % Normalized by annular gap.

Note: Formulas as given by author.

$$j = St Pr^{2/3} = \frac{Nu}{Re Pr^{1/3}} \quad \therefore \quad j = 0.023 Re^{-0.2} \leftrightarrows Nu = 0.023 Re^{0.8} Pr^{1/3}$$

3 EXPERIMENT DESIGN AND BEHAVIOR

3.1 Experiment Overview

To test heat transfer in fluoride salts, this study use the University of Wisconsin - Madison (UW) Natural Convection FLiBe Loop (NCFL), shown in Fig. 3.1. Its layout mimics that of the later generation Oak Ridge National Laboratory (ORNL) corrosion loops [118] and it is constructed from 316 Stainless Steel tubing with a 3 mm thick wall and an outer diameter of 2.54 cm (1 in). To minimize pressure loss the layout uses wide bends that have a centerline radius of 12.7 cm (5 in). An exception is made at top-right corner, where the top cross joins the vertical down-comer at 45° asymmetric-Y to allow sliding a train of material-samples down into the flow path. Neither the top cross nor bottom cross are quite horizontal and incline at 10° or 20° to help drain salt and increase elevation.

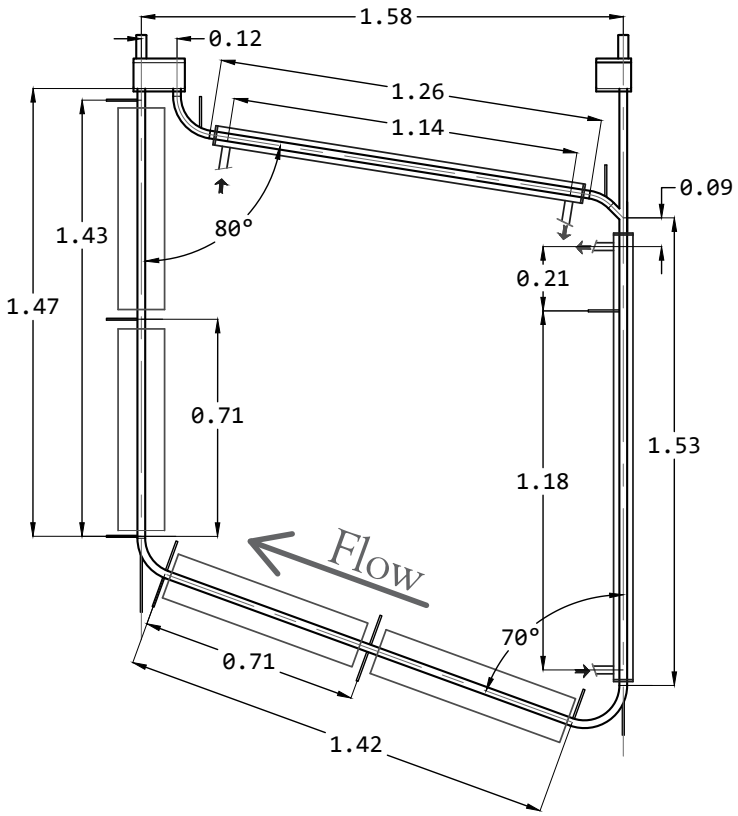

Figure 3.1: Loop geometry with radiant heaters, dimensions in meters.

Power control

Elevation is important because it ties to the flow rate, which is driven by a density difference arising from the loop temperature drop (ΔT_l). Temperature drop is controlled by heat removal in the top cross or down-comer using forced air convection from a variable speed blower. Typically, the top cross cooler provides enough cooling and the counter flow down-comer is blocked off with insulation forming a quais-static air gap.

Heat input along the bottom cross and riser is provided by two different heater generations. The earliest method used 4 sets of radiant-mode heaters, with two on each leg providing up-to 1.7 kW of heat on a proportionally controlled 208 V circuit. All four heaters operated at the same constant-power setting and were monitored by thermocouples (TCs) near the center of the radiant face.

The second heater configuration wrapped strip heaters around the tubing, creating one heater zone per leg. Both legs were operated at the same direct current (DC) voltage supplied by a calibrated Xantrex XDC 40-150 power supply. Current in each heater was similar within ± 4 %, giving a power input of 4.3 kW per leg, which is slightly higher than radiant mode heaters, as tabulated in Table B.1. The 6.4 $mm \times 0.203$ mm Kanthal A1 ribbon was wrapped helically with a 9.5 mm pitch over a layer of electrically insulating silica fabric. To limit voltage, each heater was constructed from eight sub-sections of strip heaters that operated in parallel off a single power supply. Small length differences could create minor current imbalances, and heater supply wires were routinely checked with a clamp-on ammeter to ensure uniform power delivery.

Measurements

Loop operations primarily rely on temperatures monitored with K-type TCs. Several heat transfer relevant locations shown in Fig. 3.2 and more details are given in Fig. B.1. The salt-wetted probes have a 1.6 mm outer diameter and are inserted with their tip just past the tube centerline. The original radiant-mode heaters used similar probes installed halfway along the hot face with their tips protruding just past the radiant face. After switching heater designs, additional surface TCs were welded to the loop at the locations shown in Figs. B.2 to B.4.

More detailed fluid measurements are available using the fiber optic distributed temperature

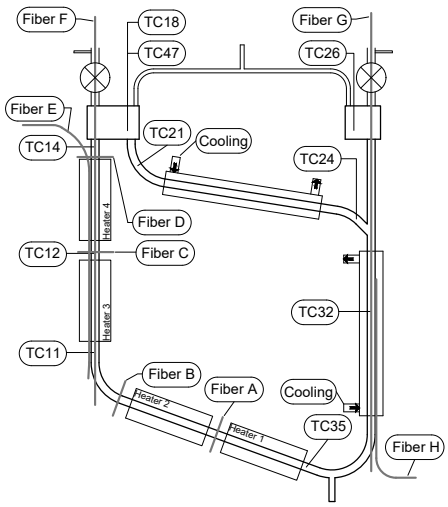

Figure 3.2: Wetted thermocouples and fiber sensor locations.

sensors as the locations in Fig. 3.2. These sensors use an ODiSI-B interrogator from Luna Inc [119] to measure high-resolution strain. By hanging the fibers inside a $0.8\,\mathrm{mm}$ helium filled capillary tube, as shown in Fig. C.6, mechanical loads are eliminated and strain is correlated with temperature [120]–[122]. This provides high resolution measurements every $0.625\,\mathrm{mm}$ at $23\,\mathrm{Hz}$; corresponding to 30 measurements across the tube diameter on Fibers *A-D*. The four long capillaries contain thousands of measurements, located coaxial to the tube centerline on *F* and *G* or embedded in the tube wall on Fiber *E* and *H*.

Additional instrumentation includes two air speed transducers in the air-distribution headers and output measurements by the DC power supplies. For all heater types, voltage, resistance, and current are regularly verified using a calibrated hand-held multi-meter. Furthermore, there are two electrochemical probes [123] and salt samples are withdrawn to monitor chemistry.

Flow rate

Fully quantifying heat transfer also requires measuring the flow rate; however, there is no instrument available to directly log this value. Off-the-shelf instrumentation is limited by the corrosive, high temperature environment combined with the small loop-wide pressure drop (ΔP_l) in natural circulation (NC) flow. Therefore, the NCFL uses a time-of-flight measurement technique based on temperature transients flowing past T_{24}, T_{32}, and T_{35}. Based on the travel distance between each TC pair, given in Table B.2, and the pulse transit time (Δt) three speeds

can be calculated and then averaged into the velocity estimate ($\bar{v}$) for that transient. Averaging multiple transients from the steady state period provides the relevant flow speed (v_s) and its standard deviation (σ_v).

Data Description

Describing the data starts with a steady-state operating period called a "test," which occurs under constant input power and cooling air flow rate. When settings change, loop temperatures show a large initial transient and then settle into quasi-steady values that are allowed to persist at least 1 to 2 days. These temperatures are averaged for heat transfer analysis, with flow rate measurements taken at the end of each associated with it.

Another important identifier is the operating "campaign" (C) during which the test occurs. These multi-week operating periods help track instrumentation and salt quality, as detailed in Section B.2. The first three shakedown campaigns are discarded for heat transfer analysis, leaving C4 - 6 for radiant-mode heater heat transfer studies. The conduction-mode heaters were added for heat transfer analysis of C7 - 9 and were replaced with new heater coils for the 10^{th} and final campaign. Additionally, fresh $2LiF - BeF_2$ (FLiBe) was added after the 7^{th} campaign, 5 years into the project.

3.2 Flow Behavior

Due to NC coupling, unexpected flow behaviors can occur in the loop that are briefly described using a data subset tabulated in Section D.4. Calculations and results use the full data sets contained in Sections D.5 and D.6.

Temperatures

The first step is understanding the flow environment through temperature readings that provide the primary insight to the loop. At a global-level the loop is stable and its operating conditions are repeatable within campaigns without major chaotic transients. However, there is a minor cyclic temperature component. This variation of a few °C over an approximate day-long period is shown in Fig. 3.3. It is synchronized around the loop and although cycles are not carbon copies, they center on a stable average after only a few hours of constant power operation. It is assumed these are linked to the daily fluctuation in room temperature (T_∞), since salt

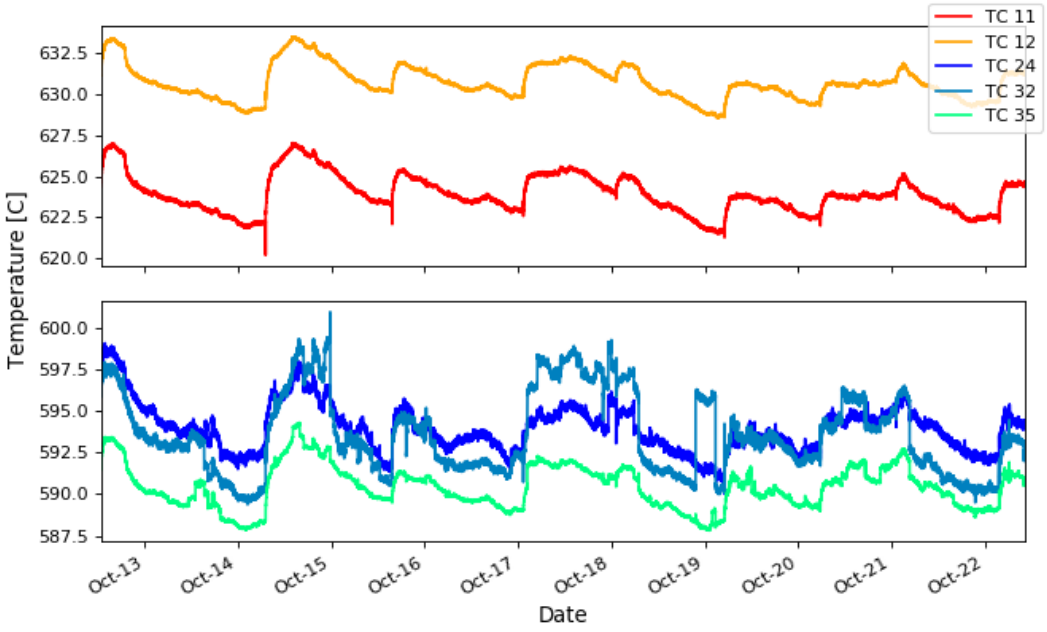

Figure 3.3: Steady state temperatures over several days, showing cyclic profile on all TCs along with a random component at the cooler exit.

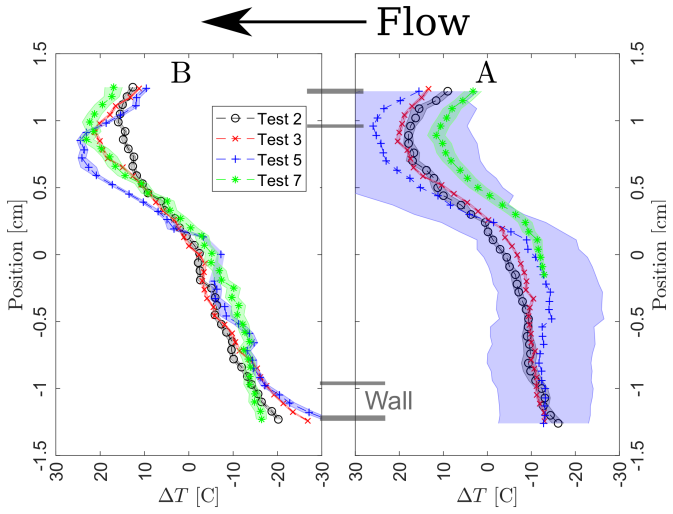

Figure 3.4: Temperatures on Fibers A and B for several tests.

temperatures correlate with T_∞ strongly at the cooler exit on T_{24} ($\rho \approx 0.40$)[1]. Further along the flow path, this correlation weakens slightly and it is possible the air cooler is magnifying daily temperature fluctuations of $\pm 2\,^\circ$C.

Fig. 3.3 also shows features not related to daily temperature swings in the random spikes

[1] All statistics reach $p \ll 0.01$ unless otherwise noted.

and jumps recorded on T_{24}, T_{32}, and occasionally T_{35}. These small 1 to 4 °C transients often rise or fall over 1 s and then either follow an exponential decay to previous values or settle into new plateau value; called a spike or a jump, respectively. Most likely, these result from a shifting flow patterns in the thermally-stratified flow leaving the cooler. Any change in the flow pattern can cause the rapid initial transient by pushing a different-temperature lamina into contact with the TC tip. Because salts have a large the Prandtl Number (Pr), the shifts can be sub-mm and still swing temperatures several °C. The spikes may also arise from eddies, but the jumps require a more sustained effect, possibly from changes in the frozen layer of salt that lines the top cross cooler. Further evidence that spikes and jumps are related to freezing is from the apparent correlation between high cooling rates or low T_{24} and the prevalence of spikes or jumps.

Elsewhere thermal stratification still dominates the NCFL flow but it does not cause the dramatic TC readable effects. Instead, fiber sensors show it helping enhance mixing, as predicted in Section 2.3. Radial temperature profiles show the bottom cross mixing in Fig. 3.4 and the riser in Fig. 3.6 for a selection of tests detailed in Table D.7. Across a wide range of operation conditions, temperature profiles are similar on Fibers A and B. The salt nearest the walls helps contribute to the extreme gradients, which can reach an impressive 10 to 50 °C/cm depending on power input. For a given test, the gradient is relatively stable along the tube length, which indicates the flow is fully developed at Fiber A. This is only 0.75 m from the elbow, much shorter than calculated development lengths, which agrees with the predictions of Meyer and Everts [111]. Test 5 does have a large uncertainty band surrounding Fiber A because of eddies flowing along the tube in a test condition with a low the Invervse Graetz Number (L^*).

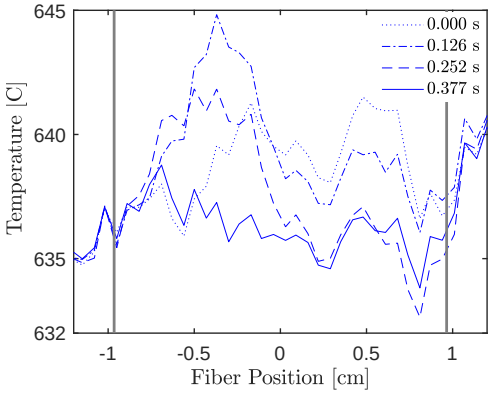

Figure 3.5: Temperature profiles on Fiber D during Test 3 at 8 Hz.

Normally, eddies are reserved for the riser, where the symmetric temperature profile sets up shear that can cause flow breakdown. Again, the profile develops quickly, before the riser midpoint, giving a U-shaped reading on Fiber C in Fig. 3.6. The riser exit however, does not always adhere to this profile, thanks to mixed convection discussed in Section 2.3. Mixing

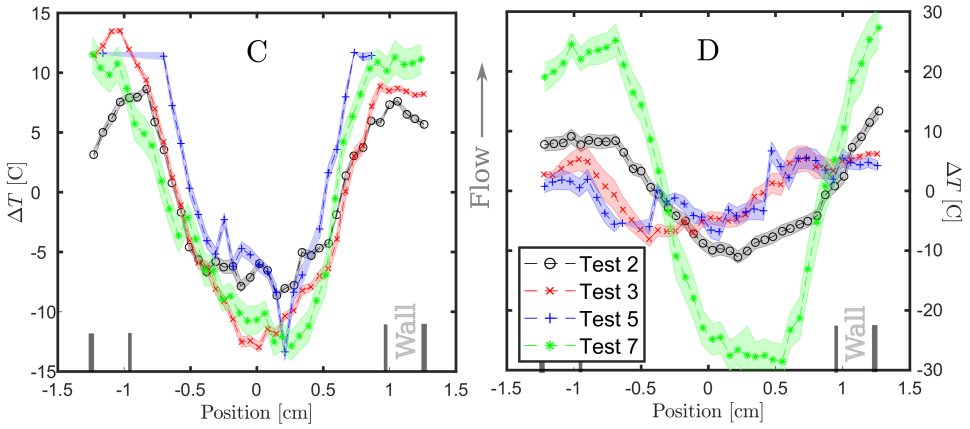

Figure 3.6: Riser temperature profiles for Fibers C and D.

is driven by eddies of hot salt that peel off the wall to mix with the bulk. T_{14} records this as measurement noise, like in Fig. C.2. But at higher speeds, the U-shaped profile will sway left and right on the fiber sensors, with Fig. 3.5 capturing a lamina of hot salt mixing as it flows past. Looking along the tube centerline, Fiber F in Fig. D.4 reveals these eddies are forming $>40\,cm$ below Fiber D. This is near the midpoint of Heater 4 where there are no weld seams, instruments, or internal burrs to disrupt the flow but where the heat flux and temperatures are highest.

Flow rate

Based on the temperature stability, the NCFL flow rate should also be stable. Long term temperature oscillations like in Fig. 3.3 are simultaneous around the loop and will not affect the driving ΔT_l. This is captured in Eq. (3.3) that predicts the expected flow behavior based on losses and driving pressures from Eqs. (3.1) and (3.2).

$$\Delta P_{loss} = \frac{1}{2}\frac{64}{Re}\frac{L}{D_h}\rho v^2 + \Delta P_{minor} \tag{3.1}$$

$$\Delta P_{drive} = \beta g h \rho_0 \Delta T \tag{3.2}$$

$$v \propto \frac{c_1 \Delta T}{c_2 T} \tag{3.3}$$

Analyzing a thousand time-of-flight measurements and plotting v_s for each test in Fig. 3.7 shows the flow rate is indeed stable and predictable. The total average of $5.7\,cm/s$ is slower

than the predicted range of 6 to 10 cm/s, but within acceptable limits. Unexpectedly though, there is a clear $T_{s,in}$ dependence without any impact from ΔT_l. Correlations show v_s depends strongly on T_{21} ($\rho = 0.79$); although, any wetted TC correlates with decreasing strength further along the flow path. Against ΔT_l however, there is no correlation, even when linear regression accounts for other parameters, like temperature or higher-order effects.

This dependence is another result of freezing in the top cross. Large ΔT_l requires a high air flow rate through the cooler, building up frozen salt layers that obstruct the flow path. High $T_{s,in}$ counters this and it does so at the cooler entrance, where the cold cross-flow air removes much of the heat. Further verification is possible using both coolers, with Fig. 3.8 showing a clear outlier compared to single cooler trends. Also visible in Fig. 3.8 are the large error bars for the dual cooler test. These arise because time-of-flight measurements require an isothermal down-comer to allow thermal transients to reach T_{35}. Cooling this leg also reduces the measurement quality at T_{32} and therefore few tests were performed in dual cooler configurations.

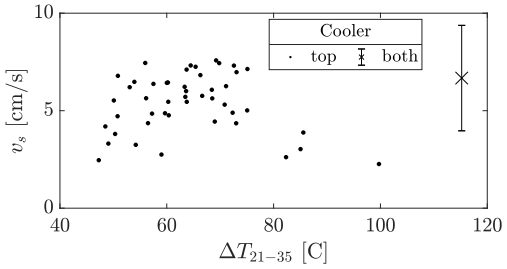

Figure 3.8: Using both coolers permits higher flow rates at large ΔT_l.

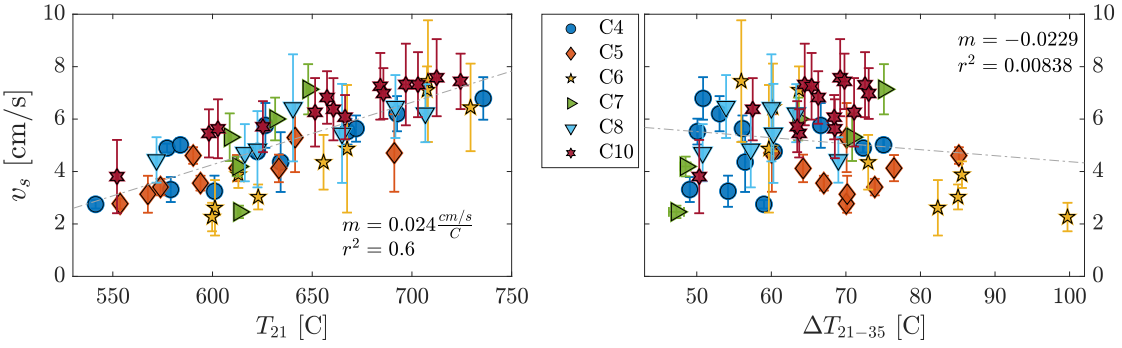

Figure 3.7: Loop flow rates showing a strong dependence on salt temperature but not ΔT_l.

3.3 Operation and Maintenance

Flow rate measurement highlights an important aspect of molten salts; the fact that molten salt instrumentation and Operation and Maintenance (O&M) are a study in their own right. To further experimental work with molten salts this section qualitatively details O&M experience tested in the NCFL.

Flow rate measurements

Flow rates are the most challenging measurement because of the operator experience required to generate accurate time-of-flight measurements. The initial plan was to use the short-term spikes and jumps at the cooler exit as transients for time-of-flight measurements. However, if they are caused by changes in the frozen salt layer, their reading is unlikely to be stable as the flow adjusts to a new ΔP_{minor} in Eq. (3.1). Analysis suggests this may be true, since flow rates vary significantly and lack any clear trends. Without more data about how these transients are produced, a full analysis is not possible and they are omitted from flow rate measurements.

This requires the operator produce short boundary condition transients, called pulses, for time-of-flight measurements. The best approach is to symmetrically oscillate the cooling air flow rate for 5 to 15 s to form a slug of cold salt that traces out the trough shown in Fig. 3.9 on downstream TCs. An alternative, shown in Fig. C.3, is to open the insulation just past the cooler exit and apply a blow torch flame to the tubing for 2 to 7 s.

Ideally these pulses do not impact the underlying flow. Narrow torch pulses cause the least change and normally retain underlying flow noise. However, they diffuse quickly compared to blower cold-pulses that can also retain underlying measurement noise and do reliably pass T_{35}. In both methods experience shows that each test has a range of pulse that yield similar flow

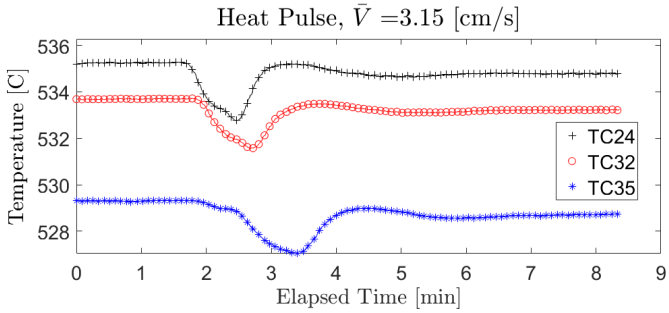

Figure 3.9: Blower driven time-of-flight cold pulse.

rates. The exact range depends on the operating condition and as expected, high cooling rates require larger air pulses while high-temperature tests require longer a blow torch duration. Once identified, pulses inside this range create successive troughs or peaks on each of the three TCs, like in Fig. C.5, without disturbing temperatures elsewhere in the system. Outside this range, large pulses cause simultaneous troughs on hot-side TCs and can decrease T_{14} measurement noise. Based on experience, the selected range was for pulses to disturb only the three time-of-flight TCs and to ensure the temperature transient at each TC was $\Delta T \leqslant 5\,^{\circ}C$. Any pulse outside this range is excluded from the v_s average.

This range however does not answer the question of accuracy for time-of-flight measurements. Very large pulses are clearly unreliable because of a large spread in calculated velocities between TC pairs. Figure 3.10 shows an extreme example from a a loss-of-cooling transient recorded on Fiber D. Flowing salt is quickly restablished once cooling restarts, but the characteristic flow noise takes several more minutes to reestablish.

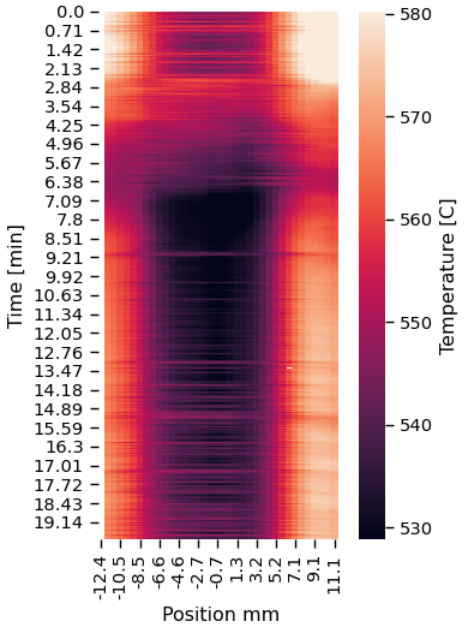

Figure 3.10: Flow stagnation on Fiber D after a loss of cooling air.

For "reasonably sized pulses" avoiding visible flow disturbances and obtaining consistency within $\bar{v}$ are critical for determining the proper pulse size, but are not sufficient to prove the measurement is unbiased. Detailed analysis is not able to definitively show this either because coupling ensures any transient is theoretically felt loop-wide. However, for practical ranges of bias a few tools have offered some insight. The easiest is to correlate pulse size against the measured speed, which was used to show that blower hot-pulses were a poor measurement technique; likely because of the slow ramp-down rate. An additional tool is available in linear-regression analysis that can compare pulse generation methods while accounting for other variables. This also found issue with the blower hot-pulse as well as the air-bypass pulse.

Ultimately, the blower cold-pulse and blow torch methods failed to show significant trends

and were easily repeated across a wide range of test conditions. This does not prove a lack of bias, but at worst the bias is highly variable and can be captured in the standard deviation across many pulses. The error bars in Fig. 3.7 show that even after eliminating bad pulses, time-of-flight measurements are noisy and have a large range. By including many hot and cold pulses in σ_v, analysis shows this method provides a sufficiently reasonable estimate of flow rate for subsequent work.

A secondary flow measurement approach was attempted using Fiber G, and watching flow moving along the down-comer. In Fig. 3.11 several large pulses visibly disturb temperatures as they flow down the down-comer, offering a tantalizing promise. However, two issues arose, the first of which is visible on the right of Fig. 3.11, where the moving standard deviation shows only white noise. Overall, fiber sensor background noise is similar in magnitude to any reasonably small time-of-flight transient. Despite multiple rounds of data smoothing, peak identification and tracking remain difficult and unreliable for use in this work. The second bigger issue is the care and O&M of long fibers, which do not survive long inside the NCFL. In short, this method is promising but further research is necessary.

Fiber sensors

To understand the challenges of working with fiber optic distributed temperature sensors it helps to review their life-cycle, starting with striping off the protective plastic coating. If left on, this melts as the fiber heats and sticks to the capillary, causing mechanical strain as the metal undergoes thermal expansion. This invalidates the thermal-strain correlation and makes future fiber replacement difficult. However, without the coating, bare glass fibers are exceptionally fragile and they eventually break near their hottest location. This is true even for flat fiber sensors like Fibers *C* and *D*; although their survival time may be longer than vertical sensors. The long centerline fibers have a tendency to break during shutdown. This may indicate they are not free-hanging in the capillary such that contracting steel pushes them to break. However, they do not show any indications of sticking inside the capillary and this remains a frustrating puzzle.

Nominally, replacing fiber sensors is not a big issue, except that at the NCFL operating temperatures, fibers suffer an unexplained "annealing" phenomena over the first $\approx$72 h at

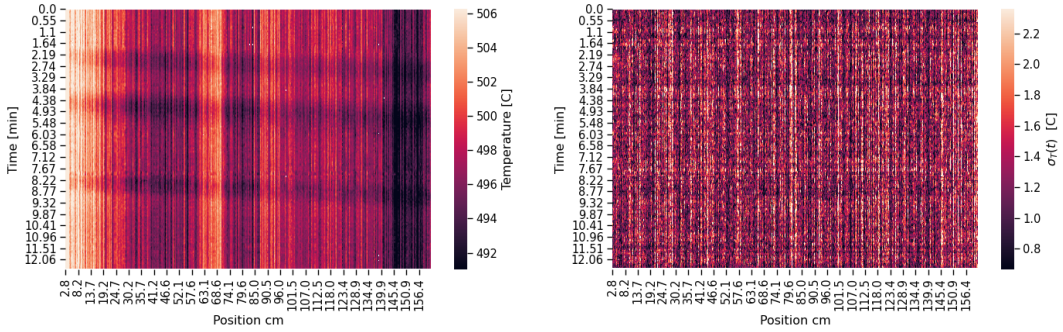

Figure 3.11: Fiber G time-of-flight thermal transients in temperature data (left) and the standard deviation over time (right).

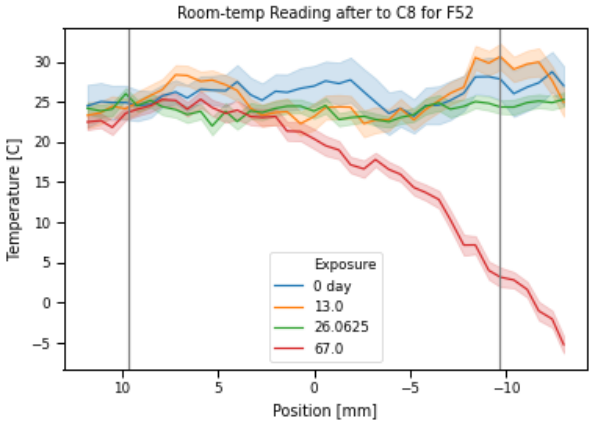

Figure 3.12: After a total of 67 days at temperature, the initial Fiber C key is biased at room temperature, compared to more recent keys taken after the sensor "annealed."

temperature [120], [121]. This remains an area of active research that is beyond the scope of this work but for this study its impact was a change in the the room-temperature key from which measurements are based. Figure 3.12 shows room temperature readings using a key taken 67 days previously in comparison to keys taken more recently after the loop was operated with salt in it. There is a clear bias using the original key and its shape is not easily corrected. Therefore, the NCFL procedure was to install a new fiber sensor and operate a full campaign before using it for quantitative analysis in the next campaign.

Additional studies

Obviously, this plan does not work if fiber breaks on shutdown. Therefore, the centerline fibers were mostly used for qualitative measurements. One such reading was monitoring the melting of a freeze plug in the down-comer cooler. Figure 3.13 shows the melting front slowly

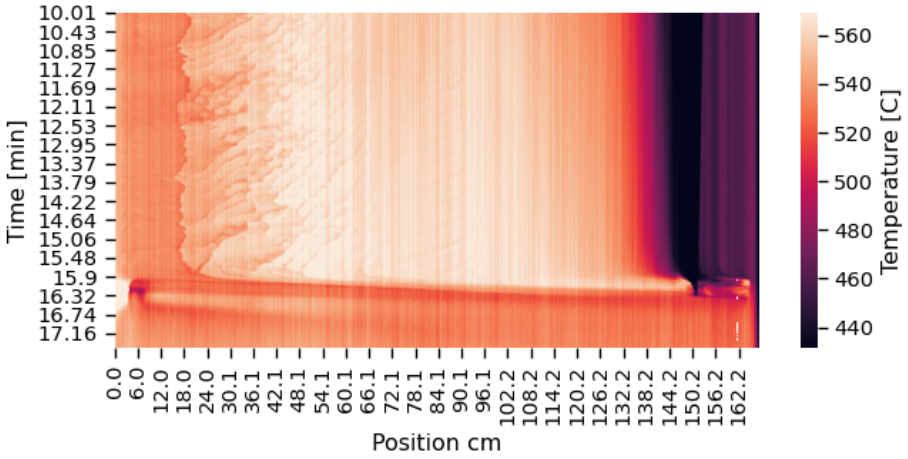

Figure 3.13: Fiber G observing a freeze plug melting in the down-comer.

propagating down the fiber while above, NC cells move up the centerline towards T_{24}. This caused visible measurement noise similar to that on T_{14}. Once the plug melted, the fiber shows a fast transient that rapidly develops back to the standard forced convection temperature profile; offering a unique transient simulation problem, for codes like System Analysis Module (SAM) [43].

Similar to the freezing analysis, the NCFL performed frequency response testing, following similar methods developed by University of California, Berkeley (UCB)[124], [125]. In conjunction with Dane de Wet[126] a series of frequency response tests were performed on the NCFL, like shown in Fig. 3.14. Coupling meant that the response was limited and the frequency data was too noisy for a full analysis. Future testing may be possible with more cycles; however, this will extend each test over multiple weeks or possibly months.

A similar issue of complex coupled behaviors limits the present analysis of the electrochemistry probes. These grew out of work by Brian Kelleher [95] and Keiran Dolan [127] that was followed up by Will Doniger [123], [128] performing measurements in the NCFL. The initial probe design used un-shielded electrodes and suffered measurement noise that was tentatively identified as electrical interference. During one set of cyclic-voltametry tests in Campaign 3, a reverse polarity sweep accidentally deplated about half the radius off a molybdenum electrode, as shown in Fig. C.10. Luckily this was in the small tank so its impact on the flow should be minimal but before campaign 4, nearly a gram of beryllium metal was added to the dump tank

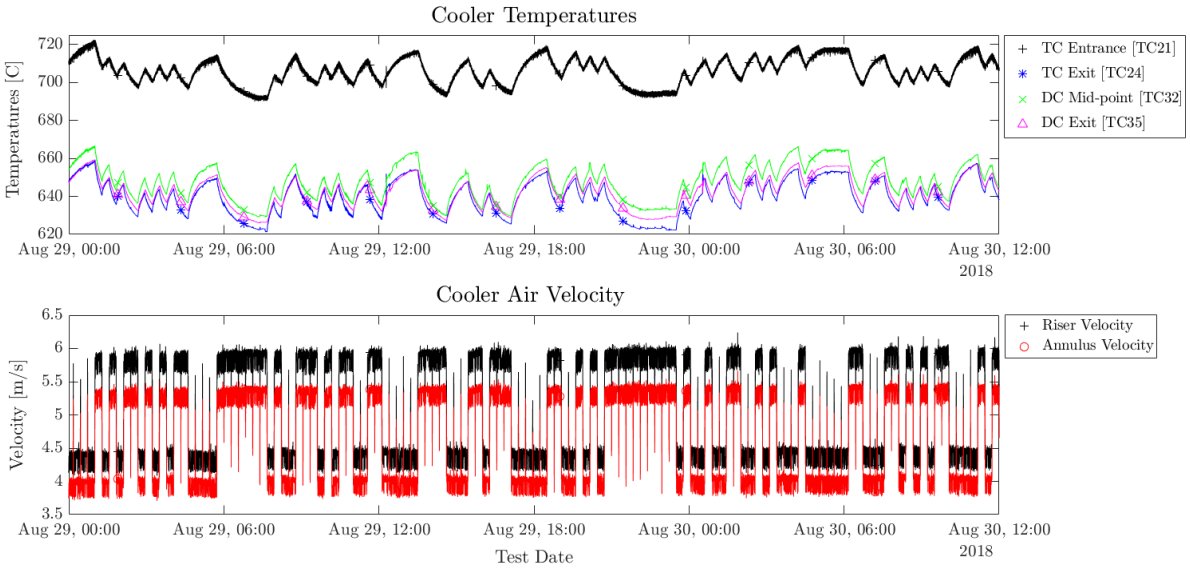

Figure 3.14: Temperature and oscillation history for a blower-driven frequency response test.

and allowed to melt into the salt over 72 hours to try and reduce impurities. As a result of this accident and the noise, a second generation of shielded probes, shown in Fig. C.11, were developed for later testing through C10.

Care of salt-wetted instrumentation

The lack of moving parts means that NCFL maintenance is limited to instrument replacement and salt sampling. However, unlike designs for easily replaced fiber sensors, major loop instrumentation is hard to maintain because of beryllium contamination and the oxygen-free loop environment. UW has a detailed beryllium control exposure plan used in this work that is built on experience from B. Kelleher [95]. Contaminated work includes the use full-face respirators, personal protective equipment (PPE), and monitoring for air and surface contamination.

Replacing instruments is easier if the instrument accesses salt through a gas interface. The two tanks were designed specifically for this purpose and hosted two generations of electrochemistry probes and two different level sensors that were all accessed at various times. Because the of the gas interface, these instruments can be accessed with the loop in cold-shutdown using a sealed glovebag attached to the instruments thermal stand-off. This adds further protection for workers and, by replacing the atmosphere with argon, it limits oxygen ingress to the loop.

Experience shows that, once the large Swagelok fittings can be coaxed lose, instruments

Figure 3.16: A stainless tube showing the green coating in the gas space compared to the matte color for the salt-wetted section.

can be removed easily. In fresh salt, a small amount of condensate, known as "snow," does collect on instrument sections inside the thermal stand-off, like shown in Fig. 3.15. The coating is durable enough to not fall-off unless the instrument is scraped. As the salt in the loop became "dirty" over time, like at the end of C6, black salt deposits tend to adhere near the salt interface and there is perhaps marginally more snow.

Removed stainless components that were only exposed to the gas-space often have a green hue, like that shown on the left side of Fig. 3.16. Submerged 316 SS can have dark salt clinging to it, but is otherwise matte-colored 316 SS that looks like most post-corrosion steel coupons [123], [129]. A nickel mesh shown in Fig. C.11, does not change as dramatically but it too lost some luster. More obvious are the occasional clear, bright salt crystals, also visible in Fig. C.11 and on the right of Fig. 3.16. These contrast well against a dark salt background and show that some segregation mechanism exists for salts depending how they cool.

In the event that a salt-wetted instrument must be replaced, like fiber capillaries when the coating isn't removed or salt-wetted TCs the process is much more challenging because of frozen salt in the instrument port. Experience shows that FLiBe forms an annoyingly durably seal between metal components that will not melt-free unless parts are heated well above 450 °C, to account for thermal losses. Such temperatures preclude

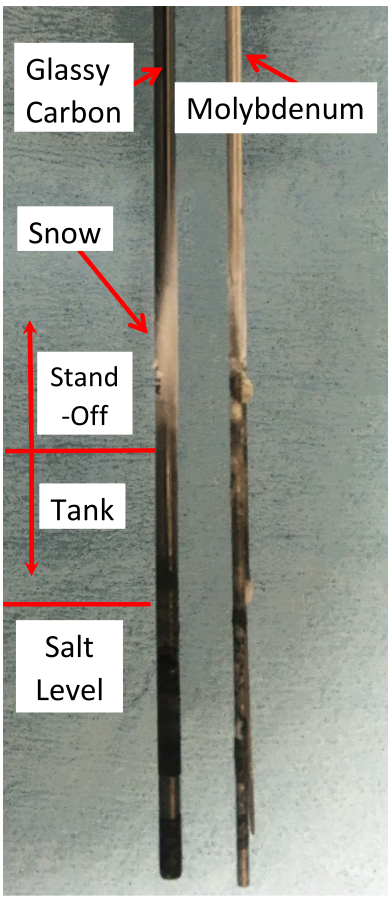

Figure 3.15: Snow coating the glassy-carbon above the salt level.

the use of plastic bags to control the atmosphere and must operate the loop below atmospheric pressure to ensure operator safety. Even with careful heating, this is harsh and all three TCs removed for calibration checks were destroyed in the process.

Salt sampling

To draw salt samples, a different method is required to access the tank gas space during operations. Instead of glove bags, a "double-ball valve" system is employed, with one valve permanently mounted to the loop and a second sealing the detachable sample chamber. A Teflon Swagelok at the far end of the chamber allows a sampling rod to slide down into the salt while a gas port provides clean, positive pressure argon. With the chamber designed to contain all salt-wetted components, only the clean length of sampling rod emerges beyond the Swagelok for cleaning prior to transport to a glove box for further analysis.

The salt wetted components used two sampling methods to draw salt from the tank. The earliest relied on a thick-walled 6.35 mm tube and a vacuum chamber to draw salt into the cold steel until it froze. Simple to construct and operate, this method proved that "cool" FLiBe is perfectly capable of traveling through >1 m of cold stainless without freezing; however, it does not readily navigate needle valves.

An improved sampling method was designed by Paul Brooks [130] to lower a small bucket into the salt. Buckets are pressed from 316 SS shim-stock and they must fit inside a carefully machined sampling rod, all of which complicates setup. The payoff is better control of sample size and quality, since shim-stock is easier to clean than a tube interior. Additionally, the foil can be peeled off after use, revealing a uniform frozen puck, like in Fig. D.3. The vacuum method required melting salt from the tube and occasionally the slow-cooling furnace allowed impurities to segregate, like in Fig. 5.17.

4 ANALYSIS

Based on these observations the NCFL flow can be analyzed for heat transfer. Different calculations are used for each boundary condition, split by location into the the air cooler, riser and bottom cross, which are noted using subscripts: AC, R, and BC. Results in the heaters are further split for the radiant heaters in Campaigns 3 to 6, analyzed using the radiation equations in Section 4.3, and the conduction heaters studied in C7 to C10, detailed in Section 4.4.

4.1 General Heat Transfer Calculations

Initial heat transfer steps all follow the same process that starts with data ingest using MATLAB 2019b® [131]. Salt flow speeds (v_s) is calculated next and the steady-state window for each test is identified. This duration is based on constant input power and cooling air flow rate, and is then trimmed to remove any transient from the previous operating state. Acceptance for heat transfer calculations requires σ_T and $\sigma_{\Delta T_l} \leqslant 2\,^{\circ}C$ for six or more hours. Tests are finally averaged for use in all further calculations. MATLAB 2019b® calculations also obtain the standard deviation (σ) over the test window for each measurement and combine any additional uncertainties into the total uncertainty (η), as described in Section A.1. Ultimately, η is propagated through the following equations by Engineering Equation Solver (EES) [132].

Heat transfer calculations use the inlet and outlet TCs $(T_{in}$ & $T_{out})$ to calculate the average bulk salt temperature $\left(\overline{T}_s\right)$. Most fluid properties, like density (ρ) and viscosity (μ) are calculated at $\overline{T}_s$ from correlations recommended by Romatoski and Hu[1] [97]. Mass flow rate calculations use the cold fluid density and some correlations require properties at the film temperature, which is taken as the average inner wall temperature $\left(\overline{T}_{w,i}\right)$ for the given zone.

Together, fluid properties and mass flow rate feed into the energy balance

$$Q = \dot{m}\,(T_{out}\,c_p - T_{in}\,c_p) \tag{4.1}$$

which, should equal the external heat load Q_{ext}. This is the loss-corrected energy input from heaters (Q_{htr}) or removed by air convection (Q_a) . Losses (Q_{loss}) are predominately through the insulation (Q_{insul}) as calculated in Section A.2. Additional losses from fin conduction

[1] thermal conductivity (k) and heat capacity, (c_p) are temperature independent.

along TC or fiber sensor ports is also included, as described in Section A.2.

Finally, Q_{ext} is used to calculate the h through Eq. (4.2).

$$Q_{ext} = h A_i \left(\bar{T}_s - \bar{T}_{w,i}\right) \tag{4.2}$$

where A_i is inner wall surface area and $\bar{T}_{w,i}$ is the average inner-wall temperature. Finally, h is converted to the Nusselt Number (Nu) :

$$Nu = \frac{hD_i}{k} \tag{4.3}$$

using the inner diameter (D_i) and k for comparison with correlations.

Against Nu, several different non-dimensional terms can be used, defined after Chapter 7. Most common for this analysis are the Reynolds Number (Re), the Prandtl Number (Pr), and modified Grashof Number (Gr^*), defined as:

$$Re = \frac{\rho D_i v_s}{\mu} \tag{4.4}$$

$$Pr = \frac{\mu c_p}{k} \tag{4.5}$$

$$Gr^* = \frac{g \beta \rho^2 D_i^4 Q''}{\mu^2 k} \tag{4.6}$$

4.2 Annular Cooler Analysis

The TCs annular cooler is shown in Fig. 4.1. Salt flows in past T_{21} to record $T_{s,in}$ and then flows down the central tube parallel to the air flow. Exiting the cooler, salt passes T_{24}, T_{32}, and T_{35}, which are averaged into $\bar{T}_{s,out}$ to alleviate biasing from thermal stratification.

Cooling air from a variable speed blower pass through a distribution header where its speed (v_a) and inlet temperature $(T_{a,in})$ are measured. It enters the annulus through two-2 cm inner-diameter tubes, oriented perpendicular to the flow with their centerline tangent to the top or bottom of the tube. Exiting through the same geometry, the outlet air temperature $(T_{a,out})$ is measured in the elbow. All air physical properties are calculated at $T_{a,in}$ and $T_{a,out}$ from EES correlations for humid air with a 10 °C dew point.

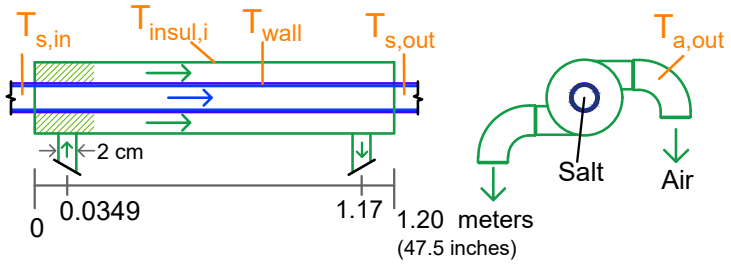

Figure 4.1: Layout of the top cross cooler flow path and temperature measurements.

The air heat balance includes the convected energy measured as the temperature rise

$$Q_a = \dot{m}_a \left(T_{a,in}\, c_{p,in} - T_{a,out}\, c_{p,out} \right) \tag{4.7}$$

plus the losses. Losses are calculated from equations in Section A.2 to account for Q_{insul}, fin conduction, and a change in stagnation enthalpy of the air. In combination, Eq. (4.8) gives the total energy convected by the air, which is equivalent to that lost from the salt.

$$Q_{ext} = Q_a - Q_{insul} + \Delta Q_0 + Q_{fin} \tag{4.8}$$

Q_{ext} is used to calculate h in Eq. (4.2), given $\bar{T}_{w,i}$. However, there is no way to measure the wall temperature because air flow would bias any welded TC and corrosion concerns prevented embedded TCs in the tube wall. Instead, $T_{w,i}$ and the outer wall temperature $(T_{w,o})$, are calculated from Q_{ext} and $\bar{T}_a$. This applies Eq. (4.2) and requires the air-side heat transfer coefficient (h_a).

After considering many correlations, h_a was ultimately obtained from simulations using Release 19.0 of ANSYS® Fluent® [133]. These were performed on a simplified cooler geometry with a constant-temperature inner wall surrounded by adiabatic boundaries. The provided Transition SST Model with default settings [134] was used after an initial set of straight annuls simulations showed performed better than other solvers against a developing annular-flow correlation [98].

Straight annulus simulations were also used to converge the mesh, which is composed of swept linear hexahedral elements. Its final parameters include 20 inflation layers, a characteristic element length of 2 mm, and a normal angle of $\leqslant 3°$. In the final model, the mesh is broken to include the side-wise entrance and exit ports, using an unstructured tetrahedral elements that were constructed using same characteristic dimensions and inflation settings. The central straight annulus retains the initial swept mesh for a total of $7.2 \cdot 10^6$ elements.

This model performed 74 simulations covering the operational range of $\dot{m}_a$ and T_{hot} given in Table B.1. The constant temperature wall ranged from 600 to 1000 K, while $\dot{m}_a$ was driven by an inlet pressure ranging from 100 to 800 Pa. All other conditions were held constant, including the inlet air temperature at 300 K and the exit to atmospheric pressure. No surface-to-surface radiation model was used because the adiabatic outer wall limited its impact to $\leqslant 5\,\%$ of the inner wall heat flux (Q''_w).

The results are 2.5 to 5 times larger than the straight annulus correlation and agree with Q_{ext}. EES calculations use lookup tables for h_a based on experimental $\overline{T}_a$ and $\dot{m}_a$. This forms an iterative process using Eqs. (4.9) and (4.10) to calculate $T_{w,o}$ and include radiation heat transfer (Q_{rad}). Equation (4.10) uses temperatures converted to Kelvin and a surface emissivity $(\epsilon_{rad}) = 0.5$ based on measurements by Cao et. al. [135].

$$Q_a - Q_{rad} = A_o\, h_a \left(\overline{T}_{w,o} - \overline{T}_a\right) \tag{4.9}$$

$$Q_{rad} = \frac{A_o \sigma_B (\overline{T}^4_{w,o,K} - T^4_{insul,i,K})}{1/\epsilon_{rad} + 1/\epsilon_{rad} - 1} - Q_{insul}. \tag{4.10}$$

Finally, from $\overline{T}_{w,o}$, the cylindrical conduction equations in Section A.2 are used to calculate $\overline{T}_{w,i}$. A $\overline{T}_{w,i} < 460\,°C$ indicates a layer of frozen salt coats the inside of the tube. In this case, $\overline{T}_{w,i}$ is replaced with the freezing temperature when solving Eq. (4.2). This allows the radial conduction equations to calculate the average frozen-layer thickness and adjust D_i and A_i.

4.3 Radiant-mode Heater Analysis

The hot-side of the loop is broken into the bottom cross and riser, each of which is further subdivided by its two radiant-mode heaters. Four salt-wetted TCs are available, starting with

T_{35} at the bottom cross entrance, T_{11} at the start of the riser, T_{12} in riser midpoint, and T_{14} at the riser exit. Additional measurements are taken in each heater hot face ($T_{htr,n}$) and T_{13} measures the tube wall temperature under heater 4.

The salt side energy transfer is again calculated from Eq. (4.1). Starting in the bottom cross and following Section 4.2, $T_{s,in}$ is an average of T_{24}, T_{32}, and T_{35}. In the riser, $\bar{T}_{s,out}$ is also an average of T_{14} and T_{18} in the tank.

The input power ($Q_{htr,n}$) is calculated for each heater from the resistance and voltage in Section A.2. Subtracting the insulation losses gives $Q_{ext,n}$ and allows $h_{s,n}$ to be calculated once the wall temperature under each heater is known. One wall temperature is measured on T_{13} under heater 4. Then, using the heater 4 temperature difference:

$$\Delta T_{htr,4} = T_{htr,4} - T_{13} \tag{4.11}$$

the other $T_{w,o,n}$ values can be calculated for the measured heater temperatures.

It is also possible to calculate $T_{w,o,n}$ using $Q_{ext,n}$ and the radiation heat transfer equations in Eq. (A.10). For the tests analyzed here, these methods agree well with an average difference of only 20 °C. However, the radiation equation introduces a lot of uncertainty and noise because of its sensitivity to small changes in Q_{ext}.

$T_{w,o,n}$ is used to calculate $T_{w,i,n}$ for each heater and the two heaters on each leg are averaged together into ($\bar{T}_{w,i,BC/R}$) for the bottom cross (BC) or riser (R). The heat transfer equations for h are then calculated along each leg using the combined input of both heaters and the average bulk salt temperature for that leg ($\bar{T}_s$).

4.4 Conduction-mode Heater Analysis

Directly wrapping the heater coils around the tubing simplifies the later heat transfer calculations by removing the radiation component. Each heater is composed of six coils run in parallel by a calibrated DC power supply. The output voltage and current give $Q_{htr,BC/R}$, from which the external load to the salt (Q_{ext}) is calculated by subtracting out the losses. As before, Q_{loss} is primarily through the insulation, calculated in Section A.2, except the conduction heaters use MICROTHERM® instead of Pyrogel® HPS to reduce losses. Heat is conducted along thermocouple and fiber ports is also calculated using fin conduction equations for Section A.2,

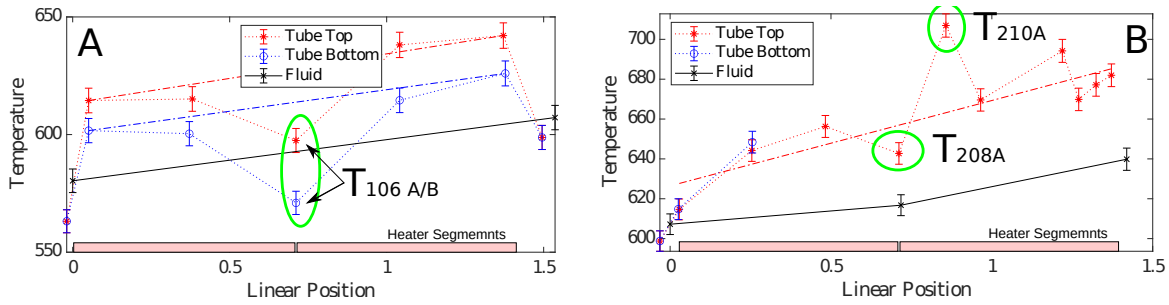

Figure 4.2: High power input temperature profiles the salt and tube surface for the first generation contact heaters. On the left, **A** is the bottom cross, while right is the riser in **B**.

adding at most a few percent to the total losses.

As before, h is calculated from Eq. (4.2), using the inner wall temperature ($\overline{T}_{w,i}$) and average salt temperature ($\overline{T}_s$). $\overline{T}_s$ is again the average of measured inlet and outlet salt temperature across either the bottom cross or riser. $\overline{T}_{w,i}$ is calculated from the outer wall temperature using radial conduction equations in Eq. (A.3).

The outer wall temperature $(\overline{T}_{w,o})$ is different. It averages the surface TCs shown in Figs. B.2 to B.4 over the leg-length (L), through:

$$\overline{T}_{w,o} = \frac{1}{L}\int_0^L T_{w,o}(x)dx. \tag{4.12}$$

Ideally, both $T_s(x)$ and $\overline{T}_{w,i}$ follow similar linear trends; however, analysis showed heat losses along fiber and thermocouple ports reduces local surface temperatures substantially. This drop is shown in Fig. 4.2 for $T_{106A\&B}$ and T_{208A} for the first generation of conduction heaters. Replacing the heaters allowed additional TCs to be added 12.7 mm to either side of the port. This revealed the temperature drop was localized and can be safely excluded from Eq. (4.12).

In contrast to the lower temperatures at ports, Fig. 4.2**B** shows an unusual high temperature on T_{210A} that may result from the heater coil contacting the TC wires or raised weld bead. Heaters are electrically isolated from the metal with silica cloth that has a low thermal conductivity. Retrospectively, teardown shows this cloth shrinks at temperature, while the heater coils expand and shift; allowing heat to conduct along the TC wires or weld beads.

The possibility of an electrical short was considered because this would increase the local heat flux. However, analysis shows this is unlikely because the same current is supplied to each

heater coil. Additionally, the heater alloy forms resistive alumina oxide at high temperatures. This limits shorting to early in the heater life, like the self-short visible in Fig. C.9 where the alloy never oxidized.

Based on these observations, high-temperature readings are excluded from Eq. (4.12). The resulting temperature profiles are plotted as shown in Fig. 4.2**B**. Based on similar slopes for the surface and fluid temperature rise, the surface temperatures are averaged into $\bar{T}_{w,O}$ and MATLAB 2019b® statistical toolbox [136] is used to obtain a best-fit linear trend and calculate the root mean squared (RMS) fit of $T_{w,O}(x)$ to predictions for error-propagation in EES.

5 RESULTS AND DISCUSSION

5.1 Campaigns 4 to 6

Heat balance

Quantitatively analyzing the NCFL starts with an energy balance between convected heat (Q_s) and the external load (Q_{ext}) for each of the three zones shown in Fig. 5.1. In the cooler, Fig. 5.2**A** shows good agreement ($\rho = 0.81$),[1] and inherits a large Q_s uncertainty from the salt flow rate. The heaters in Fig. 5.2**B** also agree well ($\rho = 0.78$) but add uncertainty in Q_{ext} from reliance on $\Delta T_{htr,4}$.

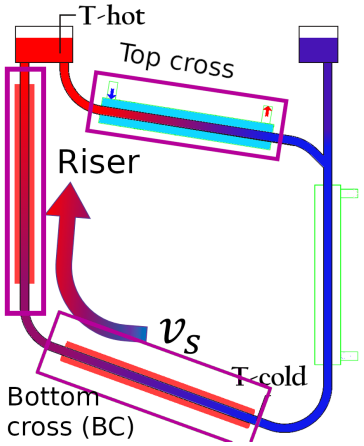

Figure 5.1: Locations for heat transfer analysis.

The heated data is subject to a correlation between the heat input and flow rate that causes visible deviation from the $y = x$ line in Fig. 5.2**B**. Defining excess heat input as $Q_{ext} - Q_s$ reveals the two calculations converge as salt flow rate increases ($\rho = -0.69$). The challenges of measuring flow rate are magnified for slow moving flows, verifying this correlation and indicating the slow flowing tests underestimate Q_s. For cooling salt, the same correlation does not hold. Instead, the difference in energy transfer corresponds to with decreasing wall temperature ($\rho = 0.47$). This is visible in the color map

[1] $p \ll 0.01$ for all stats unless otherwise noted.

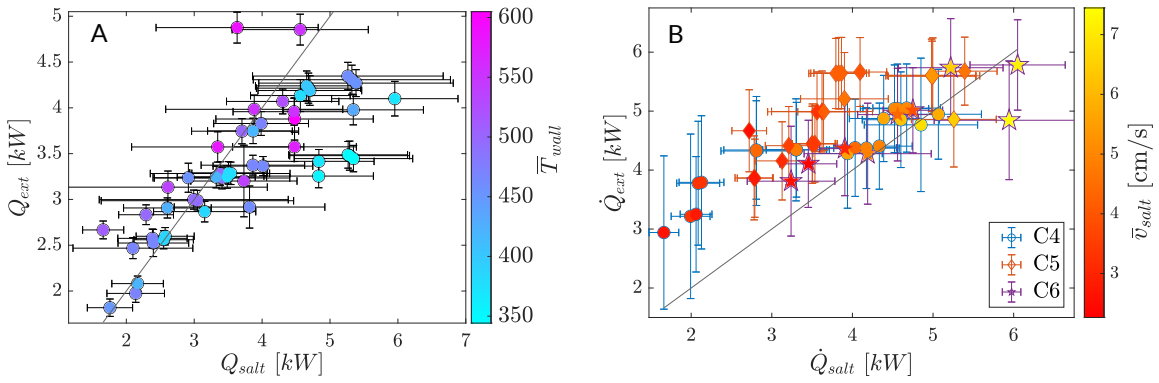

Figure 5.2: Heat balances for Cooler (a) and Heater (b) split by campaign: ◯ = C4, ⋄ = C5, & ⋆ = C6.

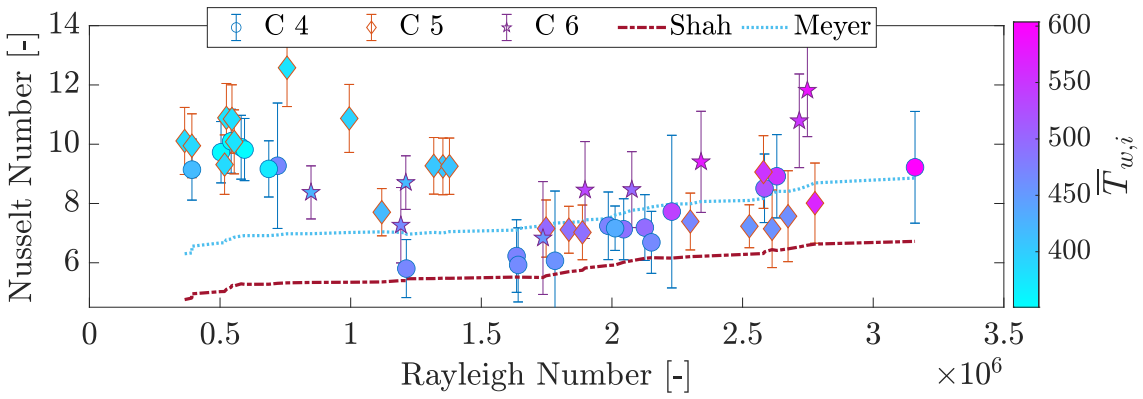

Figure 5.3: Cooling salt Nusselt data colored by $T_{w,o}$.

and corresponds to a worse heat balance as air flow rate increases ($\rho = 0.58$).

Nusselt results

Nu data in Figures 5.3 and 5.4 show Nu >5 for all results with some of the expected developing-flow trends. Cooling salt appears to best fit the mixed convection correlation from Meyer and Everts, or at minimum to meet the developing flow predictions from Shah and London. Heated salt in Fig. 5.4 has less difference between correlations and overall fits the developing correlation from Shah and London best.

Across these results, the uncertainty, given in Table D.3, is at minimum $Nu = \pm 0.72$ and is largely tied with property uncertainty. Figure 5.4 is notable for the large σ_{Nu} in horizontal heat transfer during C4. Elevated σ_{Nu} arises from a larger σ_T during this campaign, the cause of which is not clear.

This is one of two notable features, where campaign 4 Nu is elevated compared to later tests. Table 5.1 shows later horizontal Nu agrees well with the developing flow correlations at ±10 %. The second feature is in Fig. 5.3 where cooling Nu appears split into two groups at the Rayleigh Number (Ra) $\approx 1.5 \cdot 10^6$. The low-Ra has elevated Nu compared to a second, higher-Ra group that clusters near the constant-heat flux (Q'') developing flow correlation.

Discussion

Analyzing the Ra split in the cooling salt data shows it is a result of calculation bias in the simulated h_a. Parametric simulations studied a range of air flow rates and T_w; assuming the wall temperature was uniform along the entire air interface. This was done to decouple the salt

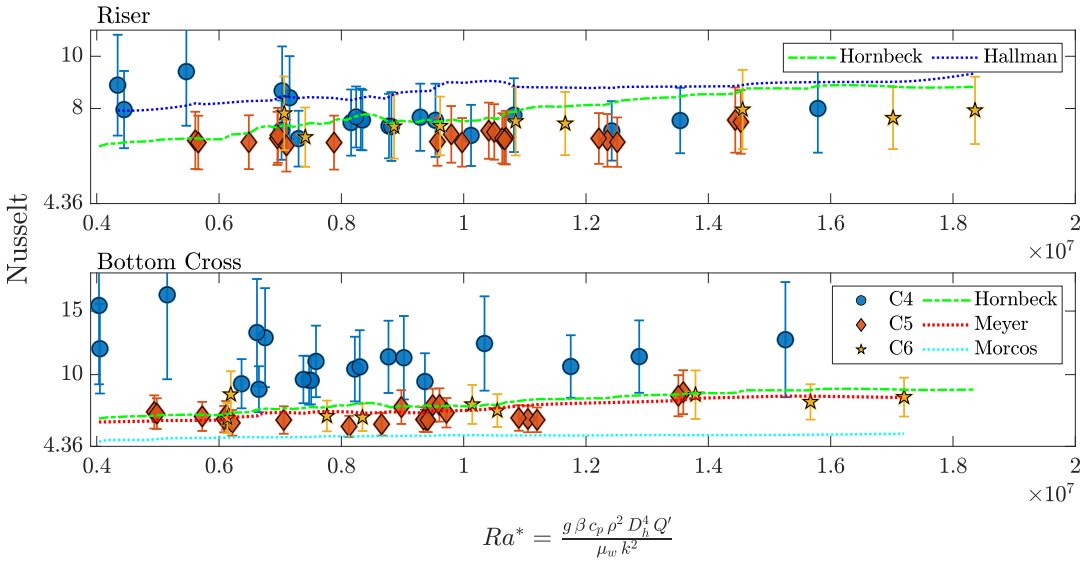

Figure 5.4: Heat transfer in the heaters broken by operating campaign. Ra uncertainty averages 17 %.

and air analysis, since it allowed the salt-side solution to use the salt and air heat balances to iteratively narrow-in on h_a and $T_{w,o}$. This works when $\bar{T}_{w,i} \geqslant 460\,°C$ because the T_a is lower than $T_{w,o}$ and simulated T_a matches the experimental. When frozen salt limits heat transfer however, T_a from the experiment falls below the simulated value because frozen salt insulates high heat transfer cross-flow zone at the cooler entrance. Reducing air-side heat transfer and the experimental T_a causes the analysis to select a low h_a based on simulated air temperatures. Ultimately, this over-predicts $\bar{T}_w$ and elevates Nu, as shown by the coloring of Fig. 5.3.

While a coupled salt-and-air simulation should be able to eliminate this bias, molten salt phase-change simulations are beyond the scope of this work. Other discretization methods for $T_{w,o}$ were considered but all require additional assumptions and limit the analysis range to a subset of the data. Therefore, the best method for analyzing the data, as done above, is to simply exclude data where $T_w \leqslant 460\,°C$, or approximately at $Ra \leqslant 1.5 \cdot 10^6$.

Building on these results, developing laminar conditions appear to accurately describe NCFL heat transfer for both heating and cooling and across a large Ra range. This is unexpected because Ra describes natural circulation forces and a high Ra test should correlate with higher Nu. Further analysis reveals this behavior is due to coupling between flow rate and power input that ties Re to Ra, as shown in Fig. D.1. Overall, the effect is to decrease the Richardson

Number (Ri) at elevated Ra ($\rho_R = -0.56$), or in other words, the high power increases ΔP_l and shifts flow towards laminar forced convection behavior. This correlation holds in each location, with cooling salt correlating for the data at Ra $\geqslant 1.5 \cdot 10^6$ ($\rho_{AC} = -0.71$). In the bottom cross C4 follows this separately from C5 & C6 ($\rho_{BC,C4} = -0.87$, $\rho_{BC,C5\&C6} = -0.75$).

Time dependence

The campaign-level split in the bottom cross is harder to explain than the split in cooling data. As mentioned, the uncertainty difference is coupled to a larger σ_T; however, this does not impact Nu. A few repeated test conditions offer some clues when comparing the C6 data to C4, a difference denoted δ. The most prominent change is lower $\bar{T}_s$ by $\delta_T = 2$ to 30 °C.

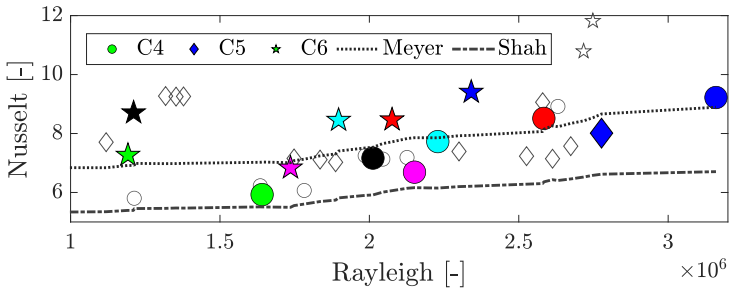

Figure 5.5: Cooling Ra and Nu colored by boundary condition. C4 = ○, C5 = ◇, C6⋆.

The colder temperatures alone should not change salt properties enough to modify the flow behavior; however, changes in the temperature difference between the salt and wall (ΔT_{s-w}) do indicate changing flow behaviors. In non-dimensional terms, the Ra change, shown in Fig. 5.5 is quite large. Normalizing its change as: $\hat{\delta} = (Ra_{C6} - Ra_{C4})/Ra_{C4}$, reveals a change in Ra by

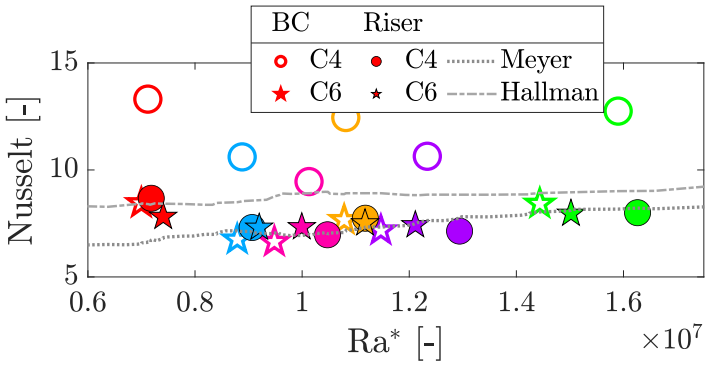

Figure 5.6: Heated $\hat{\delta}$ Ra_m and Nu colored to differentiate boundary condition. Open symbols are horizontal, closed vertical flow, ○ = C4, ⋆ = C6.

as much as $-40\,\%$. In the the heat flux based Rayleigh Number (Ra^*) shown in Fig. 5.6, the impact is reduced, proving the difference is based on ΔT_{s-w} and not Q''.

The reason δNu shows up in the bottom cross is because there is minimal change in Nu_R. Here, $\overline{T}_s$ and $\overline{T}_w$ change by a similar amounts and limit $\hat{\delta}Nu_R$ to -10 to $5\,\%$. In the bottom cross however, wall temperatures remain stable while $\overline{T}_s$ falls, resulting in an average $\hat{\delta}Nu_{BC} = -35\,\%$.

To explain these results, the system was checked for errors that might explain δT but no changes found in T_∞, heater resistance and supply voltage, nor changes to the insulation. Infrared images of the loop were used to verify the insulation performance, while TC accuracy was verified by comparing their response to that of new, calibrated instruments. Air flow transducers were validated also in a wind tunnel, without showing any discrepancy. The only change is a thin layer of oxide dust that collected at the bottom of vertical heaters as shown in Fig. C.8 or settled onto the lower face of the bottom cross heaters. It is not clear how much this affects heat transfer from the lower radiant face, since as discussed in Section A.2 the emissivity is similar, but this could reduce heat flux and may be responsible for the temperature drop.

Additional qualitative difference in loop operation were noted however, including changes in the diffusion of time-of-flight velocity pulses and increased stability of temperature profiles at the riser exit on Fiber D. These suggest a second possible explanation that salt behavior changed in such a way to reduce mixed convection heat transfer in the bottom cross. If this were the case, it is expected to result from changing salt properties like μ or ρ. While radiation heat transfer may play a role [137], [138], it is not well understood in FLiBe at this time, rendering it impossible to analyze.

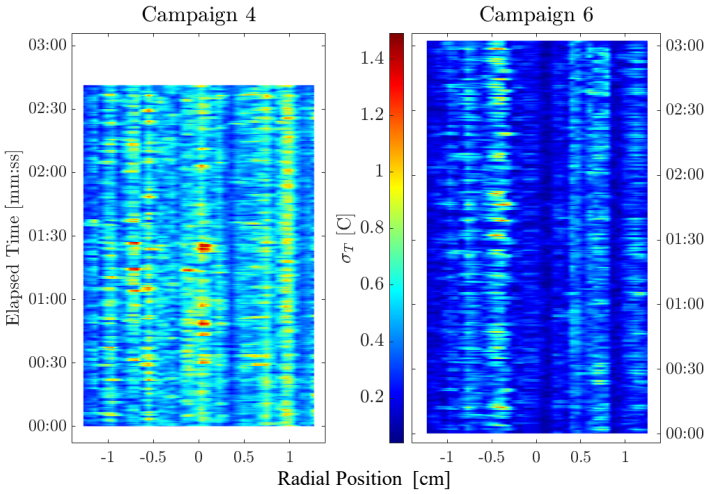

Figure 5.7: $\sigma_T(t)$ on Fiber D showing the noise reduction between C4 and C6 under the same operating conditions.

Changes in viscosity or density should be visible in other measurements, like the aforementioned fiber sensors. Figure 5.7 shows the change in $\sigma_{T(x)}$ measured on Fiber D during a C6 repeated test. There is a clear reduction in noise during the later campaign indicating laminar behavior with fewer eddies. Interestingly, the time-averaged Fiber D temperature profile is constant for both campaigns at $\Delta T(r) \approx 8\,^{\circ}C$ between the tube centerline and the wall. This is not true at Fibers B and C however, which both record $\hat{\delta}\Delta T_r = 12$ to 25 % or $\approx$3 °C.

5.2 Campaigns 7 to 10

To study possible changes in the salt, two improvements were made starting with new conduction-mode heaters and additional TCs to improve $T_{w,o}$ measurements. Campaign 7 tested these heaters with the old salt that was replaced with fresh salt for campaign 8. Further upgrades to increase the number of surface TCs, discussed in Section 4.4 were performed prior to campaign 10.

Upgrades improved the heat balance compared to the radiant mode heaters, as shown in Fig. 5.8. There is a slight skew off $y = x$ ($\rho = 0.962$) but fewer losses through the MICROTHERM® improved Q″ measurements. Uncertainty in Q_s is still dominated by σ_v with a clear outlier visible at the highest power level from the dual-cooler tests to obtain Fig. 3.8. Fortunately, σ_v does not impact Q_{ext} or heat transfer calculations allowing Nu to be calculated as described in Section 4.4.

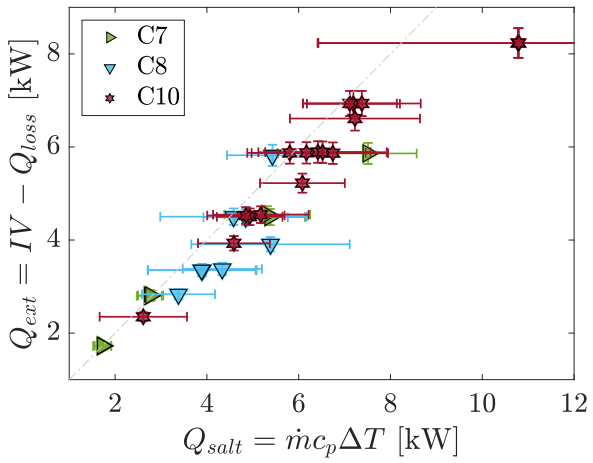

Figure 5.8: Heat balance across bottom cross and riser.

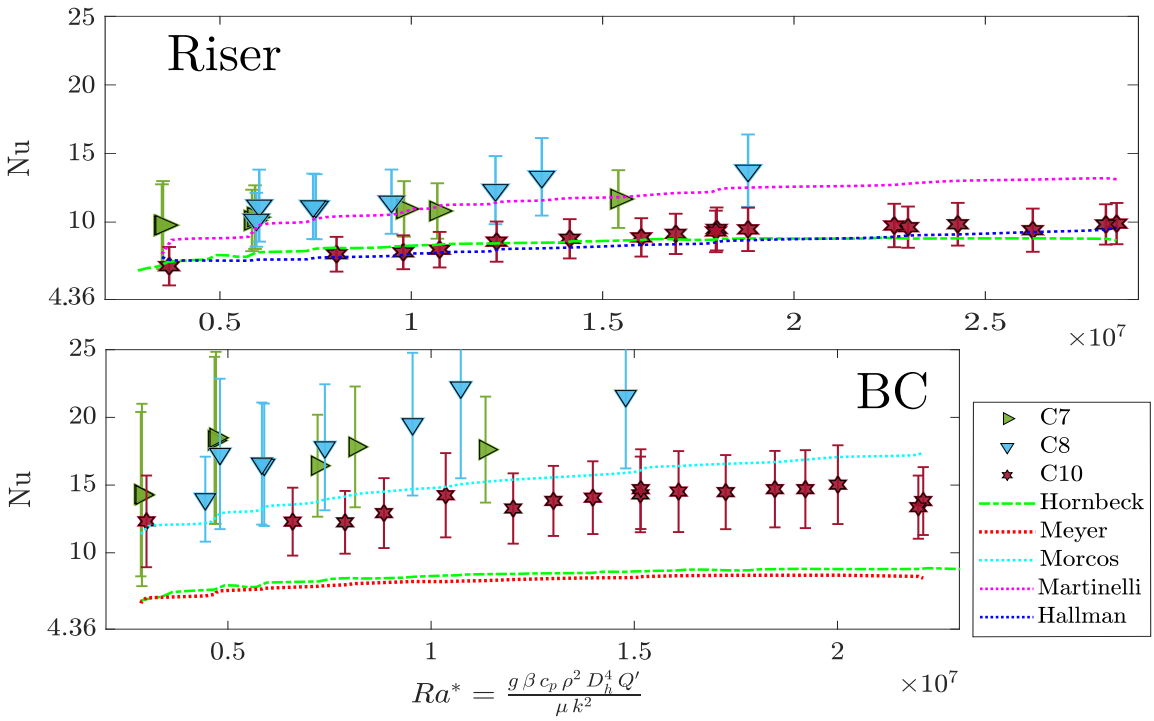

Figure 5.9: Nusselt data for the riser (top) and bottom cross (bottom).

Nu results in Fig. 5.9 show familiar trends, starting with $Nu > 5$ for all tests. Uncertainty, shown in Table D.3, is still dominated by σ_μ but there is less variation between campaigns this time. Horizontal heat transfer is elevated above the predictions of Meyer and Everts, falling closer to the correlation from Morcos and Bergles, which corrects for wall-conduction. Vertical flow again shows Nu is well predicted by Shah and London's constant-Q″ developing-flow correlation. Results also agree with the mixed convection constant-temperature correlation from Hallman.

Once again however, there is a prominent campaign-dependent split with a lower Nu during C10. Table 5.1 shows data and correlations are at a similar offset for campaigns 4 and 10, while C7 & 8 fall well outside previous ranges. Comparing the two conduction heater generations, C10 has a larger ΔT_{w-s} than the previous generation. This is from a higher $\overline{T}_{w,o}$ that may result from additional TCs improving the average. To check temperature readings are normalized through

$$\theta(x) = \frac{T_{w,o}(x) - \overline{T}_s}{T_{s,out} - T_{s,in}} \tag{5.1}$$

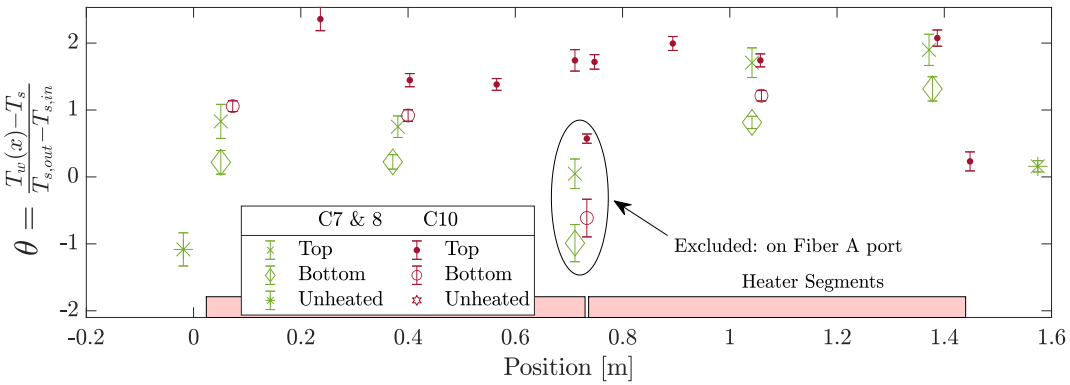

Figure 5.10: Normalized bottom cross $T_{w,o}$ from C7 to 10.

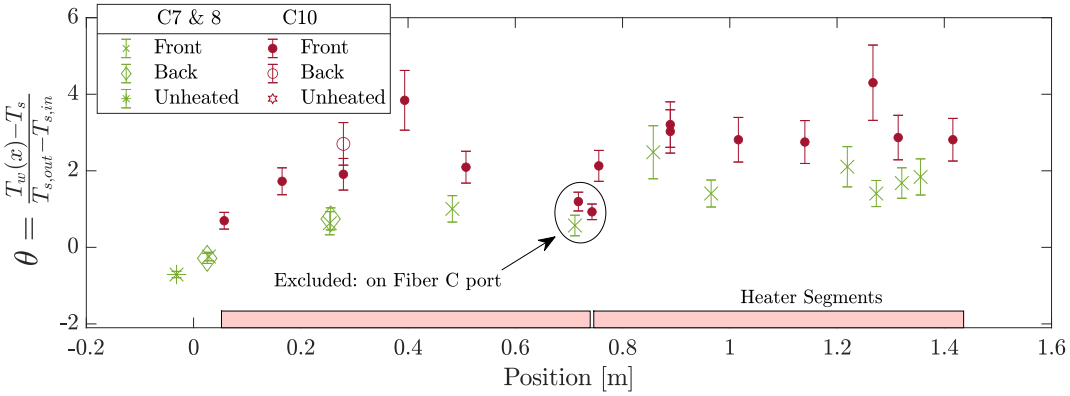

Figure 5.11: Normalized $\overline{T}_{w,o}(x)$ measurements comparing C7 & 8 to C10.

to collapse power and ΔT_{w-s} differences.

As shown in Fig. 5.10, bottom cross TCs in the same locations read only a slightly higher than C7 & 8. However, several additional TCs near Fiber *A* would raise $\overline{T}_{w,o}$ compared to earlier averages. In vertical flow however, Fig. 5.11 shows that θ is more variable within each campaign and that its underlying measurements are significantly higher during C10 at most locations.

Salt comparison

Combined with the slight offset in the bottom cross, it appears that wall temperatures are higher in the later campaign, without any clear cause. Flow rates between campaigns do not significantly differ and instruments passed their verification checks. As discussed in Section 4.4, an electrical short could increase the local heat flux; however, it is considered unlikely. Heater resistances were stable across the campaigns and teardown revealed the heaters are uniformly

oxidized except for one cold-region near the bottom cross entrance, similar to Fig. C.9.

Previously, a change in salt chemistry was proposed to explain heat transfer changes. This lead to testing a new batch of salt during C8, which in Fig. 5.9 appears similar to old salt tested during campaign 7. Quantitatively, there is no difference, even in other non-dimensional terms like Ra and Ri. And qualitatively, the loop behavior was also similar between C7 & 8, with features like blower cold pulses behaving more like during C5 than C6 testing.

One qualitative note was an increase in measurement noise at the riser exit. Flow breakdown was suspected during C7 and 8; however, Fiber D was broken for both campaigns. In C9 & 10 however, plots $\sigma_{T(t)}$, like in Figure 5.12, verify the return of flow breakdown at the riser exit. Much like early campaigns, temperature fluctuations are widespread with a high frequency. $\sigma_T(t)$ magnitude actually increased in C10; however this could be from the conduction heaters applying Q'' closer to the Fiber D port.

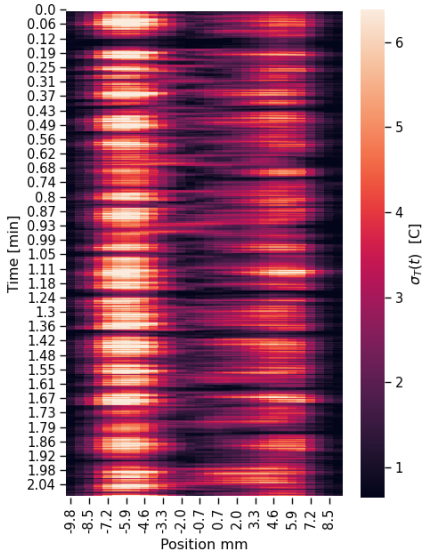

Figure 5.12: C10 $\sigma_T(t)$ on Fiber D shows more noise than C6.

5.3 All Nu data

Comparing Nu data across all campaigns in Fig. 5.13 clearly shows that Nu is, at minimum, well predicted as constant-heat flux developing laminar flow. Table 5.1 shows the differences between various correlations with Shah and London correlation to Hornbeck's data offering the best overall fit. Literature recommends the laminar Seider-Tate correlation and it performs almost as well, falling slightly below the developing flow correlation, as shown in Fig. 5.13.

The bottom cross does appear to behave as mixed convection but in this geometry the predictions from Meyer and Everts fall close to those of Shah and London. Higher predictions by Morcos and Bergles are promising for the conduction mode heaters but are not easy to compute for early C5 & 6 data due to limited wall temperature measurements. Ultimately, fiber sensors provide the best indication of turbulent mixing like that predicted by Meyer and Everts. A summary of fiber readings in Fig. 5.14 clearly indicate NC convecting hot salt to the upper

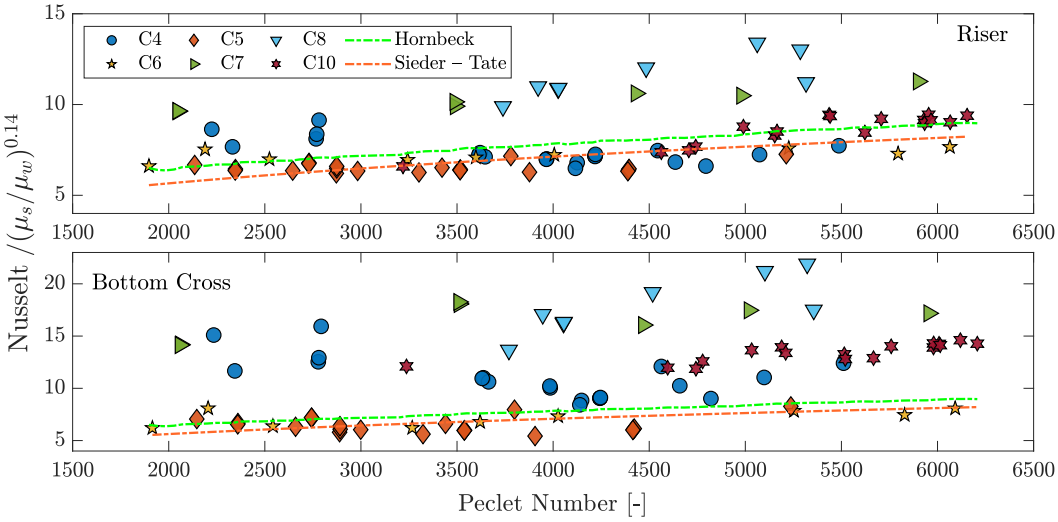

Figure 5.13: All Nusselt results against Pe.

Table 5.1: RMS percent deviation of heated Nu_s from correlations. RMS distance of: $100\% \times (Nu_{exp} - Nu_{corr})/Nu_{exp}$

	BC (%)			Riser (%)		
Campaign	Hornbeck	Meyer	S-T	Hornbeck	Hallman	S-T
4	33.9	36.9	37.1	13.8	11.2	14.6
5	13.9	10.8	14.3	11.8	29.4	8.25
6	9.48	9.27	10.8	10.9	22.3	11.3
7	55.1	57.3	58.5	28.0	27.7	33.8
8	55.5	57.8	58.4	31.4	34.0	36.2
10	38.5	41.9	41.8	6.93	7.19	10.6

tube wall and allowing cold salt to sink down along the bottom. Additionally, the upper half of the profile is mostly constant at $\Delta T_{w-s} \approx 20$ to 40 °C between Fiber *A* and *B* and it varies only with power input but not L^* .

The lower half of the flow however may still have some development after Fiber *A*, since the lower temperature gradient to the wall increases between Fiber *A* and *B*. This is likely due to the Ri coupling that permits correlation against both Ra and Pe.

In the riser, Heat transfer may benefit slightly from mixed convection, especially considering σ_T at the riser exit; however, overall Fig. 5.15 shows that laminar behavior dominates . Time-

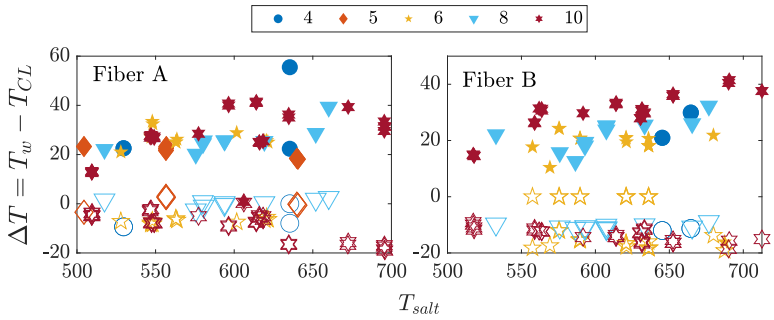

Figure 5.14: Radial temperature gradients in the bottom cross, measured with respect to the centerline temperature.

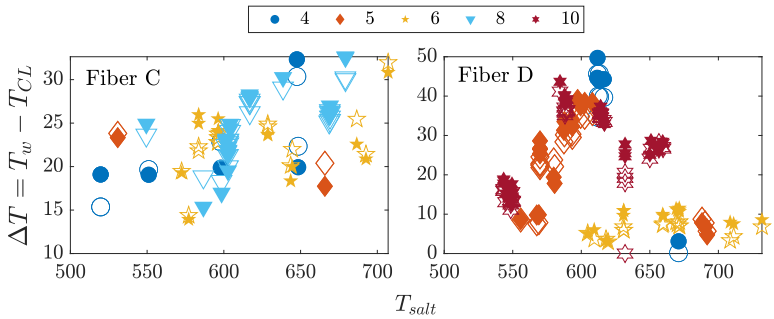

Figure 5.15: Radial temperature gradients in the riser, measured with respect to the centerline temperature.

averaging removes the high-speed fluctuations on Fiber *D* showing that ΔT_{w-s} increases along the riser. Temperature profiles are azimuthally symmetric and depend slightly on L^* , both of which are laminar features. From literature, this behavior is consistent with the predictions of Aicher and Martin [113] whose flow maps predicted the NCFL would operate near a laminar-to-turbulent transition point. However, Nu is best predicted as developing laminar flow.

Of course, none of these claims are without a caveat, as Fiber *D* helpfully demonstrates during Campaign 6 with inexplicable collapse of ΔT_{w-s} in Fig. 5.15. This may explain the lack of noise in Fig. 5.7 but it gives no indication of its cause. To explore this further, salt impurities levels are examined before a final postmortem examination when tearing down the loop.

5.4 Impurity data

Impurity effects on heat transfer have remained an underlying question throughout this analysis. While any changes to salt properties would be unexpected, equipment to measure the

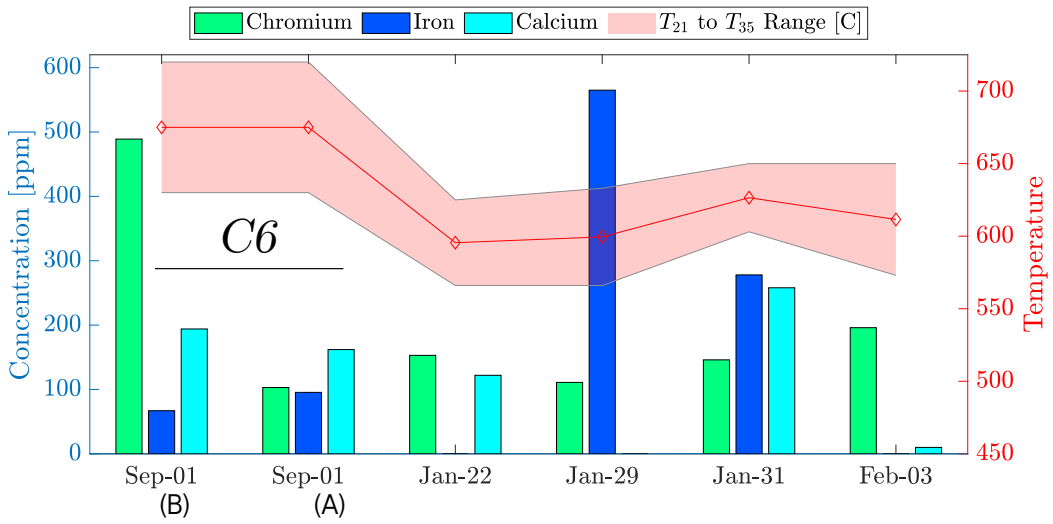

Figure 5.16: Impurities data from campaigns 6 and 7 with sampling temperatures. The temperature band represents the coldest (T_{35}) and hottest (T_{21}) values. The Sept. 1 duplicate corresponds to sections of the sample shown in Fig. 5.17.

NCFL salt is not available to provide firm answers. Currently, the only solution is to correlate trends between flow measurements and the impurity data collated in Table D.6.

For discussion, Figs. 5.16 and 5.18 track two important elements in chromium (Cr) and iron (Fe) that historically were demonstrated to be subject to thermal-gradient corrosion. Cr should be the most susceptible and was the subject of extensive corrosion work during the Molten Salt Reactor (MSR) program [91], [92]. A simple treatment of NCFL corrosion expects Cr levels to initially increase until they reach saturation. After this, they would steadily decline as thermal-gradient corrosion depletes the hot legs and plates Cr in the cold legs. Other elements, likely Fe in the NCFL, could be transported but at a lower rate because it forms a less-stable fluoride than Cr does. In contrast, impurities like sodium or calcium should not be subject to thermal-gradient corrosion because they are scarce in 316 SS and they form more-stable fluorides than Cr.

Early samples consistently showed the presence of both Fe and Cr but failed to elucidate any long term trends. Part of the issue may stem from the use of frozen salt that was found clinging to removed instruments. These tended to be white or clear and had low impurity concentrations. During campaign 6 however, a vacuum-sample shown in Fig. 5.17 visually

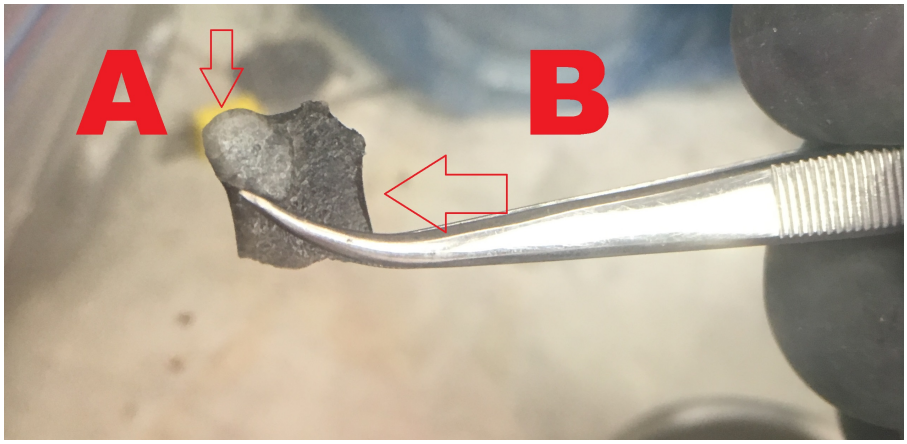

Figure 5.17: Campaign 6 salt sample showing segregation after melting out of vacuum tube. Portions A and B were broken off for separate analysis while the remaining salt was ground, per standard procedure. The results are shown in Table D.6.

segregated while cooling pushing impurities to the darker portion of the sample, as shown in Fig. 5.16. This uncertainty combined with a switch from inductively coupled plasma optical emission spectrometry (ICP-OES) to inductively coupled plasma mass spectrometry (ICP-MS) makes it challenging to analyze early salt samples.

Later dip-samples improved the accuracy, as shown by measurements of stable readings fluorides like calcium and sodium. These samples also revealed a temperature dependent trend, in Fig. 5.18 that saw Fe impurities replaced by Cr at higher temperatures. This obscures any long-term trends and may indicate there is an exchange reaction between Fe impurities and Cr that was previously deposited in the cold leg. If that is happening, analyzing thermal-gradient corrosion for any realistic system may depend on the its temperature history; adding significant complexity. However, further conclusions must await materials analysis to determine if cold leg coupons are coated in Cr and if hot-leg samples show Cr depletion.

For heat transfer, these results are interesting, but they are not expect to cause issues with the salt. Recalling historic experiments with NiF_2 in Section 2.2, the NCFL nickel impurities averaged 11 ppm, which is below the levels studied by Silverman et al. Additionally, nickel impurities were stable, with only minor changes between campaigns, and one outlier from grinding a C6 sample in a nickel crucible, which makes them an unlikely cause for any changes in NCFL behavior. Recalling the iron film observed by Salmon, [89] impurities suggest the loop interior may have iron deposits. These likely will not impact heat transfer at our flow rate but

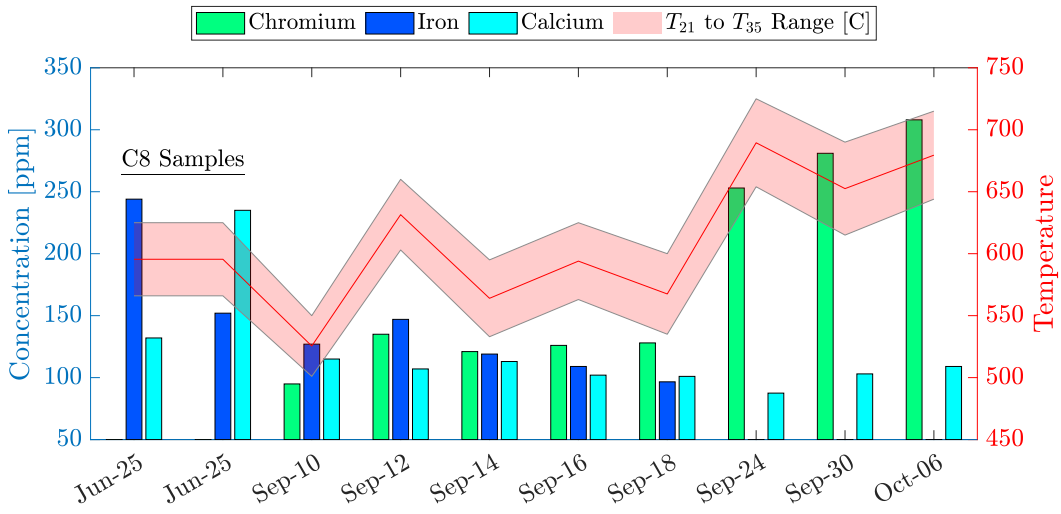

Figure 5.18: Impurities data from campaigns 8 & 10 with sampling temperatures. The temperature band represents the coldest (T_{35}) and hottest (T_{21}) values.

they could increase pressure drop and slow the flow rate.

A final note for this analysis is that it lack oxygen measurements. ICP-MS is accurate for metallic elements only and it does not provide information about their state in the salt. The state of metallic impurities and the role of oxygen in fluoride salts remain open questions. The best we can provide is that the loop was maintained under positive pressure from high-purity argon at all times. After any operation opened the loop, this was vacuumed out and replaced with argon three times in an effort to remove any oxygen ingress.

6 DECOMMISSIONING

The final job of the NCFL is to provide material samples for analyzing thermal-gradient corrosion of 316 SS by FLiBe. Decommissioning began with removal of salt-free components like insulation, wiring, and instruments that could be disposed, or cleaned for wipe-sampling. This revealed the blackened loop metal shown in Fig. C.12 that, all things considered, is in good condition. None of the tubing reacts to a strong magnet, indicating the austentic structure still dominates after 4600 hours at $\geqslant$300 °C. Visually, it is a uniform color that is slightly roughened, like in Fig. 6.1. Its texture is smoother than that of cast pipes because the pits tend to be wide and shallow with softened edges. This is especially true in the top cross cooler, where pits appear slightly wider and more numerous likely from forced air convection.

Figure 6.1: Riser surface roughness.

Close examination reveals minor color variations for different heating levels, most notably in Fig. C.4 at the blow torch test location. Another exception was found when removing insulation from the old salt storage tank, which appears to have rusted. The two tanks in Fig. 6.2 are twins from the same material and neither suffered the extreme temperature limits or duration that

Figure 6.2: Post-operation salt storage tanks.

the loop metal encountered. Because of this, the rusting is concerning, especially since the salt chemistry in these tanks dictates the conditions when the loop is filled.

Teardown of the beryllium contaminated tubing followed the UW Beryllium Disease Prevention Plan for air monitoring and full body PPE. Each step involved sliding a bag over the tube and then gently slicing the metal with a tube cutter to avoid making dust. These cuts proved the 316 SS retains its strength and ductility, since cuts required similar effort to the as-received material. After each cut, the open tube ends were capped with tape and the bags were sealed.

Table 6.1: Time-averaged temperature for samples in Section D.2.

	Temperature [C]	
Sample	Surface	Fluid
A	659	612
B	627	640
C	728	684
D	648	684
E	609	614
F	607	608
G	707	651

Further analysis took place on a downdraft table to cut material samples from the locations shown in Fig. D.2. During this, an endoscopic camera was inserted inside the tubes for visual inspection. Overall, this revealed steel that retains a uniform gray color without obvious roughness, streaks, or cracks, much like new material. The tank floors are coated in a layer of dark salt while the walls remain fairly

Figure 6.3: Post-operation views inside the large (left) and small tank (right).

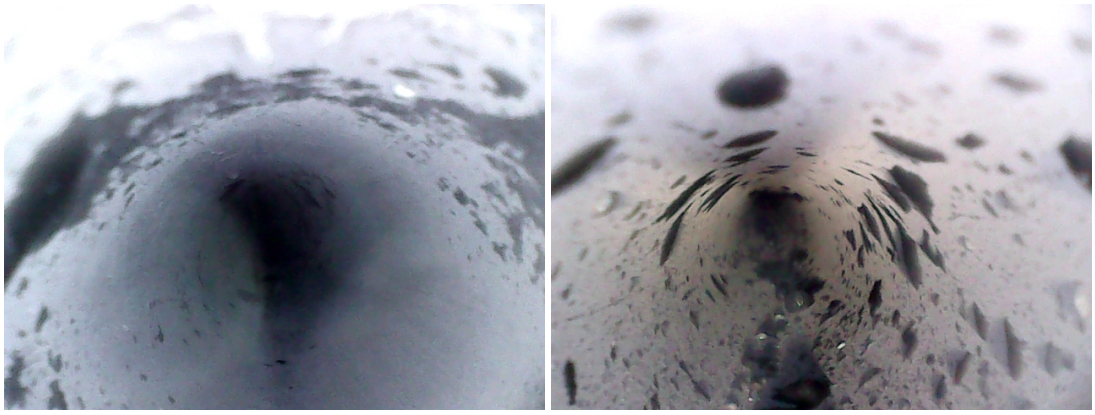

Figure 6.4: Views inside the bottom cross show sparse patches of black salt.

clean, as shown in Fig. 6.3. The small tank has more salt on the walls than the large tank and some possible snow deposits. This difference between tanks may result from the static nature of the small tank, or from its 600 °C shutdown temperature instead of 700 °C for the large tank.

Inside the loop tubing, the steel is also flat-gray color and speckled in dark salt. However, there are a few additions in several locations. Starting at the bottom cross inlet and traveling up into riser, the camera reveals patches of what appears to be black salt. These are dispersed along these legs without obscuring the underlying steel, as shown in Fig. 6.4. Horizontal flow created more patches on the bottom of the tube, while the riser has fewer spots with azimuthal symmetry.

Preceding the riser in the lower left elbow there is a blob of black salt that appears to have slid down the riser. It sits just above a field of scattered metallic deposits interspersed with blobs of white and black salt, shown in Fig. 6.5. The capillary for Fiber B traverses the tube just below this field and it has some light crystal growth near its bottom. More dramatic crystal growth is found on the capillaries containing Fibers A and C, as shown in Fig. 6.6. Both of these fibers are in the center of the heated zone and should have been exposed to hot salt that was not expected to deposit anything. Yet, crystal growth on Fiber C and the T_{12} appears to be dense enough to obstruct flow and this may explain the behavior changes discussed in Section 5.2. Crystal growth continues up the riser from its the midpoint, growing along the center-line capillary for Fiber F in a tapering rope of tinsel that disappears prior to Fiber D and T_{14}. Neither of these instruments grew any crystals.

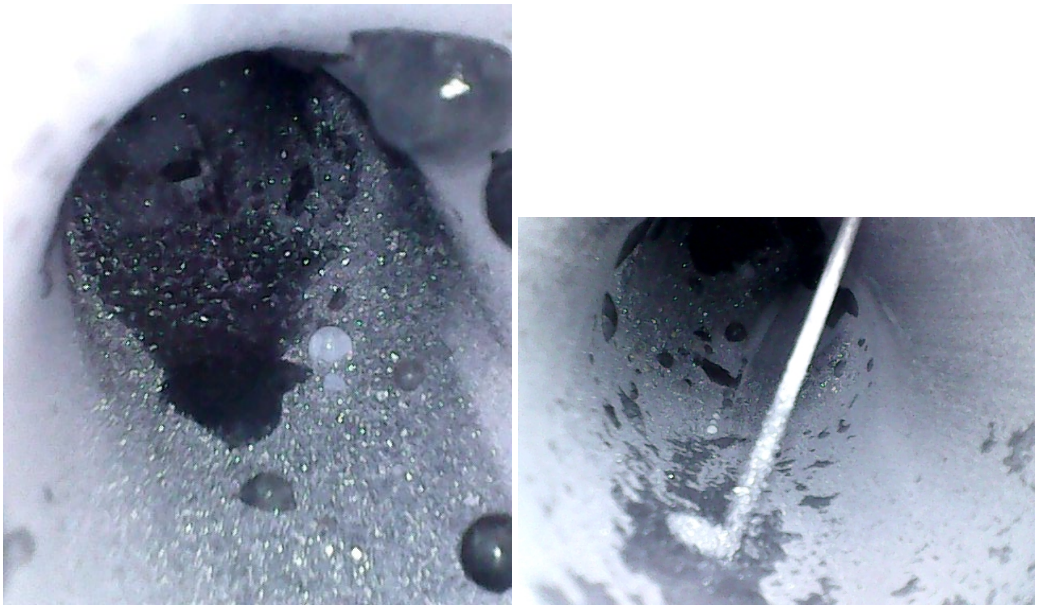

Figure 6.5: A view inside the lower left elbow at the start of the riser shows a layer of crystal growth on the outside of the bend (left) and light crystal growth on the capillary tube containing Fiber B (right).

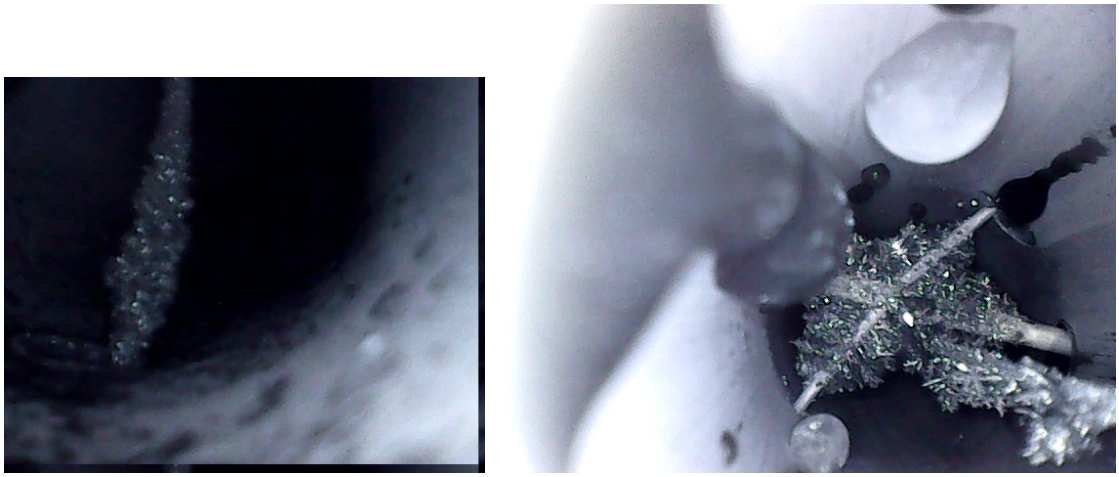

Figure 6.6: Capillary tubes protecting Fiber A (Left) and Fiber C & F (right) grew metallic crystals.

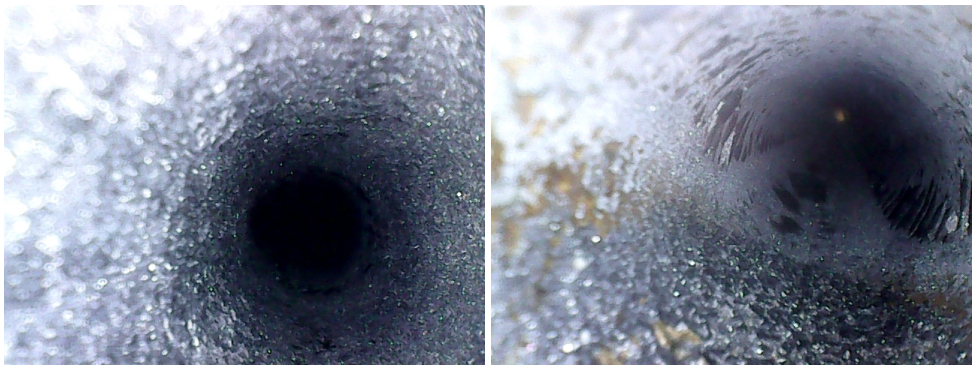

Figure 6.7: The top cross entrance (Left) and exit (right) showing a layer of metallic crystals.

When salt left the tanks, chromium plate out was anticipated as salt cooled inside the top cross cooler and down-comer. The findings indicate plate out occurred almost as soon as the air touched the tube, forming the myriad of crystals shown in Fig. 6.7. Initially the glittery deposits are azimuthally symmetric and completely covers the steel. These thin out a short distance later and preferentially grow along the tube bottom, leaving a mostly barren top with two black salt streaks running along both sides. Where air exit the cooler, there is another coating of crystals, as shown on the right of Fig. 6.7. Interspersed among these crystals however, are several rust-colored patches. It is assumed the shiny crystals are Cr and these patches are a for of iron oxide, but further analysis is needed to verify both findings, with potential implications for determining the oxide content of the NCFL FLiBe .

Rusty patches end as flow turns down the isothermal down-comer and although more crystal growth was expected, none was found. All of the three cold TCs and Fiber G are clear of deposits while the tube wall is lined with frozen salt nodules, shown in Fig. 6.8. Similar frozen droplets were observed in the riser, in Fig. 6.5, but the down-comer has far more. Images show three colors, black, white, and clear, with fewer clear salt nodules and far more dark black ones. These likely dripped down from the small tank after shutdown, since there is a flow-blocker to prevent circulation up the static leg that could have held-up salt until the down-comer tubing cooled near 460 °C.

Also similar to the riser, there is a mass of black salt in the lower elbow as flow bends toward the bottom cross. This is just upstream from the tube stalk that connects to the transfer line. Looking up into the elbow and down into the transfer line reveals more crystal growth,

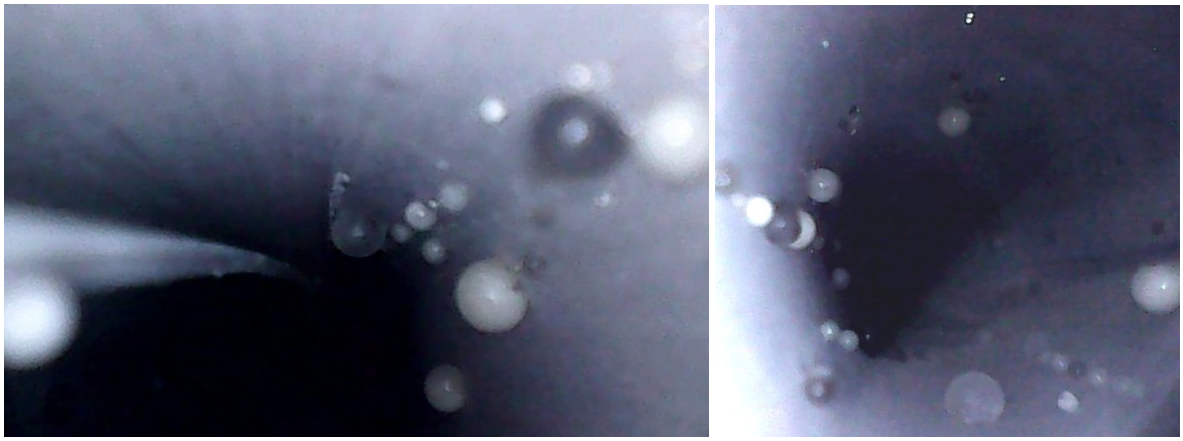

Figure 6.8: The inside of the down-comer is coated in small frozen salt nodules.

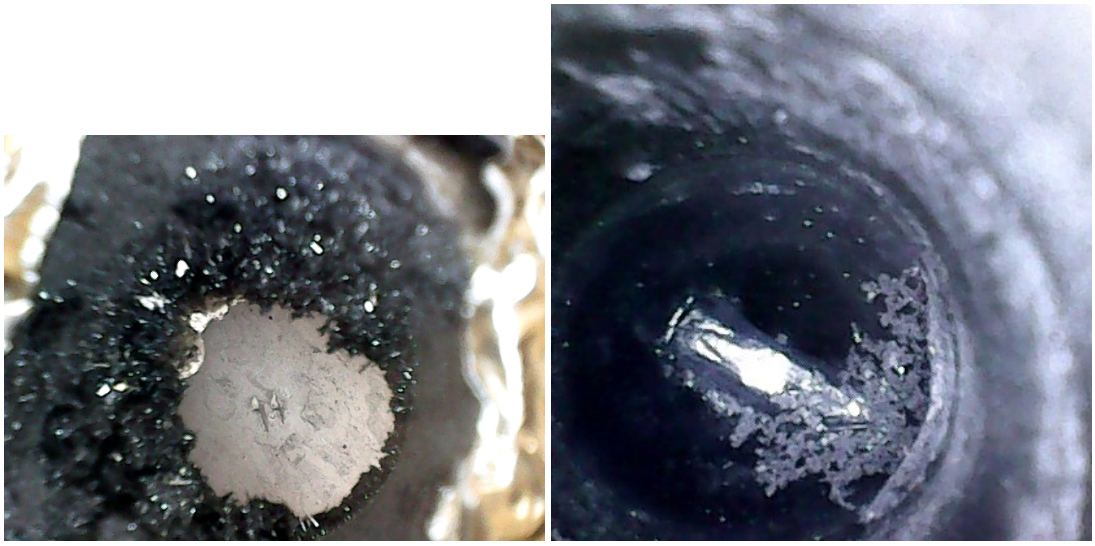

Figure 6.9: Crystal growth in the top (left) and bottom (right) of the vertical tube stalk leading to the transfer line.

including a plate-like structure on the right of Fig. 6.9.

7 CONCLUSIONS

From the initial goal of reinvigorating heat transfer work in molten fluoride salts, this study has successfully built, operated, analyzed, and decommissioned the first NC FLiBe loop in over 40 years. Covering 4600 h, the NCFL proved to be a versatile test-bed, with temperatures from 500 to 750 °C, $\Delta T_l = 50$ to 120 °C, and flow speeds <10 cm/s. Across this range, the NCFL showcased great stability and ease of operation. Its simplistic design allowed many instruments and methods to be developed for expanding molten salt research. Experience shows that gas-space equipment can be replaced easily and safely using a glovebag, whiile a sturdier double-ball valve system was necessary for online salt sampling. Additioanlly, the loop hosted a fiber level sensor, two electrochemistry probes, and several fiber sensors. The fiber sensors provided etailed temperature profiles crucial to understanding freezing, oscillations, and mixed convection behavior.

Studying mixed convection was crucial to the central thesis of this work; focused on FLiBe heat transfer. The anticipated behavior was for Nu to follow normal-fluid correlations, which the data upholds. Both the cooler and riser show strong developing flow trends and the riser agrees to a correlation from Shah and London to within 15 %. Mixed convection affects were prominent around the loop but especially impacted the bottom cross where data routinely showed heat transfer enhancement. Here, fiber sensors revealed a flow field more akin to turbulent behavior with short development lengths and temperature profiles that were insensitive to L^* . Data from campaigns 7 - 10 indicates that relying on developing flow correlations in this condition can under-predict heat transfer by at least 30 %.

Postmortem revealed a flow obstruction inside the riser that was likely responsible for the increasing wall temperatures in later campaigns. Crystal growth in the top cross was expected, but not in the riser, where thermal-gradient corrosion should have removed active elements. A detailed materials analysis is necessary to fully understand this, along with further analysis of the salt chemistry. Both salt tanks remain sealed under argon, keeping the remaining 16 kg of FLiBe for further analysis. It is hoped this can enhance understanding of the NCFL and ultimately support new developments in the molten salt community.

DIMENSIONLESS NUMBERS

Bo . . . Turbulent flow Buoyancy Parameter defined by [139]: $Bo = 8 \cdot 10^4 \frac{Gr_q}{Re^{3.425} Pr^{0.8}}$

Gr . . . Grashof Number based on temperature: $Gr = \frac{\vec{g}\beta\rho(T_{film}-T_{bulk})D^3}{\mu^2}$.

Gr* . . . Grashof Number based on heat flux: $Gr^* = \frac{g\,\beta\rho^2\,D_h^4\,Q''}{\mu^2\,k}$

Gz . . . Graetz number $Gz = \frac{D}{x} Re\, Pr$, measures laminar flow devlopment length

L* . . . Inverse Graetz number: $L^* = \frac{x}{D\, Re\, Pr}$, measures laminar flow devlopment length

Nu . . . Nusselt Number: $Nu = \frac{hD}{k}$

Pe . . . Péclet Number $Pe = Re * Pr$

Pr . . . Prandtl Number $Pr = \mu c_p/k$

Pw . . . Wall to fluid coduction relation: $Pw = Dk/t_w k_w$. Used for horizontal tubes with constant heat flux. The wall thickness is t_w and its conductivity is k_w.

Ra . . . Rayleigh Number: $Ra = Gr\, Pr$

Ra* . . . Rayleigh Number based on heat flux: $Ra = Gr^*\, Pr$

Ra_m . . Modified Rayleigh Number used by Ignatiev et al. in Table 2.1 to include characteristic height l_h and width δ, which was either the radius or annular gap (a): $Ra_m = Gr\, Pr\delta/l_h$

Re . . . Reynolds Number: $Re = \frac{\rho V D}{\mu}$

Ri . . . Richardson Number: $Ri = \frac{Gr}{Re^2}$ indicates relative importance of natural and forced convection. Mixed convection occurs for $Ri \approx \mathcal{O}(1)$

CORRELATIONS

Blasius Friction Correlation . A correlation for the Fanning friction factor

$f_{\mathfrak{F}} = 0.079 Re^{-0.25}$

Reference [117] recommends this for smooth pipes with $Re = 5000$ to $30\,000$.

Vriesema [54] used the Darcy-Weisbach form:

$f_{Darcy} = 4 * f_{\mathfrak{F}} = 0.3164 Re^{-0.25}$.

j-Factor . . . . . From the Chilton-Colburn Relation:

$j = 0.023\, Re^{2/3}$.

j is defined as: $j = St * Pr^{2/3}$, allowing the equation to be recast as: $Nu = 0.023\, Re^{0.8}\, Pr^{1/3}$.

Dittus-Boelter . . . . . A common heat transfer correlation: $Nu = 0.023 Re^{0.8} Pr^{n}$

$n = 0.3$ or 0.4 for cooled or heated fluids. ORNL reports often use this with $n = 0.4$, reffering to it as the McAdams equation, due to his initial publication in 1956.

Gnielinski . . . . . Heat transfer correlation for $Re \approx 2300$ to $1 \cdot 10^5$ or greater.

$Nu = \frac{(f_{\mathfrak{F}}/2)(Re-1000)Pr}{1+12.7\sqrt{(f_{\mathfrak{F}}/2)}(Pr^{2/3}-1)}$

Reference [117] recommends the Petukhov Correlation to obtain the Fanning friction factor.

Hausen . . . . . A heat transfer correlation for transition flow cited by Silverman as covering $Re \approx 2100$ to $15\,000$:

$Nu = 0.116(Re^{2/3} - 125)Pr^{1/3}\left(\frac{\mu_b}{\mu_w}\right)^{0.14}$

Petukhov Correlation . . . A heat transfer correlation for $Re \approx 2300$ to $1 \cdot 10^5$ or greater.

$Nu = \frac{Re\ Pr f_{\mathfrak{F}}/2}{1.07+12.7\left(Pr^{2/3}-1\right)\sqrt{(f_{\mathfrak{F}}/2)}}$

Reference [117] recommends the Petukhov Friction Correlation to obtain the Fanning friction factor.

Petukhov Friction Correlation A correlation for the Fanning friction factor:

$f_{\mathfrak{F}} = (1.58 \ln Re - 3.28)^{-2}$.

Seider-Tate . . . . . A Nusselt correlation that includes temperature dependent viscosity [140]:

$$Nu = 1.86\left[Re\, Pr\left(\frac{D}{L}\right)\right]^{1/3}\left(\frac{\mu_b}{\mu_w}\right)^{0.14} \qquad Re < 2300 \tag{7.1}$$

$$Nu = 0.027 Re^{0.8} Pr^{0.4}\left(\frac{\mu_b}{\mu_w}\right)^{n} \qquad Re > 10\,000 \tag{7.2}$$

n is often 0.14 but reference [117] recommends 0.11 for heating and 0.25 for cooling.

SALT MIXTURES

FLiBe . . . . . $LiF - BeF_2$ (66 − 34 mol/%) A popular nuclear coolant or fuel salt. Typically enriched in ^7Li

FLiNaK . . . . . $LiF - NaF - KF$ (46.5 − 11.5 − 42.0 mol%) A eutectic mixtured that is often studied as a surogate for other salts.

$LiF - NaF - KF - UF_4$ (45.3 − 11.2 − 41.0 − 2.5 mol%) . A FLiNaK variaent studied for heat transfer during the ANP Project.

$LiF - BeF_2 - UF_4$ (62 − 37 − 1 mol%) . . . . . An early beryllium fuel salt studied for during the ANP Project. Also known as Mixture 130.

$LiF - BeF_2 - UF_4 - ThF_4$ (67 − 18.5 − 0.5 − 14 mol%) . Early MSRE salt mixture, also called BULT-14

$LiF - BeF_2 - UF_4 - ThF_4$ (67.5 − 20 − 0.5 − 12 mol%) . Later MSRE fuel salt.

$LiF - BeF_2 - UF_4 - ThF_4$ (68 − 20 − 0.3 − 11.7 mol%) . Potential fuel salt for the MSBR.

$LiF - BeF_2 - UF_4 - ThF_4$ (72 − 16 − 0.3 − 11.7 mol%) . Potential fuel salt for the MSBR.

$NaF - ZrF_4$ . . . . . (59.5$NaF - 40.5ZrF_4$) Base zirconium salt during the ARE.

$NaF - ZrF_4 - UF_4$ (50 − 46 − 4 mol%) . . . . . Zirconium based salt studied for heat transer during the ANP Project. Also known as Mixture 30.

$NaF - ZrF_4 - UF_4$ (53.5 − 40 − 6.5) . . . . . One of two common uranum containing zirconium based fuel salts studied during the ANP. This variant was selected for the ARE fuel, which had a slightly different composition.

$NaF - ZrF_4 - UF_4$ (53.2 − 40.5 − 6.3mol%) . . . . . The final salt composition used in the Aircraft Reactor Experiment at Oak Ridge National Laboratory. [88]

Sodium Fluoroborate . . . . . $NaBF_4 - NaF$ (92 − 8 mol%) Potential coolant salt for the MSBR

GLOSSARY

316 SS . . . . . Type 316 Stainless Steel (ASTM UNS S31600) or or its low-carbon variant 316L SST (UNS S31603). This is a common corrosion resistant steel that is certified for nuclear use. Its nominal composition includes 16-18% chromium and 10-14% nickel. 316L SST permits a maximum of only 0.03% carbon, while the standard form allows up to 0.08%

316H SS . . . . . UNS: S31609. This high carbon variant of type 316 stainless steel permits up to 0.10% carbon, allowing it to operate at higher temperatures. The FHR project is considering this material for salt contacting piping or pressure vessels.

Hastelloy–B . . . . . A nickel based alloy on which Hastelloy–N was partially based. It has good corrosion resistance to molten salts [92].

Hastelloy–N . . . . . The comerciallized version of INOR-8 used in the MSRE and subsequent designs, like the MSBR. At least two modified version exist with additions of titanium and niobium due to issues with fission products like tellurium [66].

Inconel® . . . . . A class of nickel based alloys popular for high-temperature applications due to their superior strength at high-temperature. There are several variations, ORNL reffered only to "Inconel" in most reports, which has a composition similar to the "600" brand alloy. This alloy has 14 - 17% Cr, lower than 316 Stainles Steel.

Inconel-X® . . . . . An Inconel alloy with a composition very similar to Inconel 600. M. Grele and L. Gedeon used this alloy in their FLiNaK loop [49].

INOR–8 . . . . . One of several experimental low chrome nickel alloy materials developed at ORNL during the ANP and later during the MSRE, which became commercialized under the name Hastelloy–N. This alloy contains only 6 - 8% chromium, greatly improving its corrosion performance [66].

NaK . . . . . A eutectic alloy of sodium and potassium that is liquid at room temperature.

TRISO . . . . . **Tri**structural **iso**tropic nuclear fuel uses layers of ceramic and carbon to contain uranium oxide fuel. It was developed for high-temperature gas reactors and is being investigaed for FHRs.

TU Delft . . . . . Delft University of Technology. See work by B. Vriesema with $LiF - NaF - KF$ $(46.5 - 11.5 - 42.0\ mol\%)$ (FLiNaK) [54]

BIBLIOGRAPHY

[1] U. E. I. Administration, *Us electricity generator list 2017, eia-860*, Raw Spreadsheet Data, Sep. 2017. [Online]. Available: https://www.eia.gov/electricity/data/eia860/.

[2] ——, (Sep. 24, 2020). "Nuclear generation monthly capacity summary data," [Online]. Available: https://www.eia.gov/nuclear/data.php#nuclear (visited on 10/16/2020).

[3] ——, (Oct. 16, 2020). "Us electricity data browser 2001 - 2019," [Online]. Available: https://www.eia.gov/electricity/data/browser/#/topic/0?agg=2 (visited on 10/16/2020).

[4] J. M. Carrasco, L. G. Franquelo, J. T. Bialasiewicz, E. Galvan, M. A. M. Prats, J. I. Leon, and N. Moreno-Alfonso, "Power-electronic systems for the grid integration of renewable energy sources: A survey," *IEEE Transactions on Industrial Electronics*, vol. 53, no. 4, pp. 1002–1016, Jun. 2006, ISSN: 0278-0046. DOI: 10.1109/TIE.2006.878356.

[5] G. Barbose, N. Darghouth, D. Millstein, K. LaCommare, N. DiSanti, and R. Widiss. (2017). "Tracking the sun 10: The installed price of residential and non-residential photovoltaic systems in the united states."

[6] U.S. Nuclear Regulatory Commission. (Nov. 27, 2020). "List of power reactor units," [Online]. Available: https://www.nrc.gov/reactors/operating/list-power-reactor-units.html.

[7] World Nuclear Association. (Aug. 27, 2020). "Exelon announces early shutdown of four illinois reactors," [Online]. Available: https://world-nuclear-news.org/Articles/Exelon-announces-early-shutdown-of-four-Illinois-r.

[8] U. E. I. Administration, "Us 2017 annual energy outlook," US Energy Information Administration, Tech. Rep. AEO2020, Jan. 19, 2020, 81 pp. [Online]. Available: https://www.eia.gov/outlooks/aeo.

[9] MIT, "The future of nuclear energy in a carbon-constrained world: An interdisciplinary mit study," Massachusetts Institute of Technology, Research report, 2018, p. 275. [Online]. Available: http://energy.mit.edu/wp-content/uploads/2018/09/The-Future-of-Nuclear-Energy-in-a-Carbon-Constrained-World.pdf.

[10] R. Schmalensee, V. Bulovic, R. Amatya, F. Brushett, G. Kavlak, A. Maaurano, J. McNerney, T. Osedach, P. Rodilla, A. Rose, A. Sakti, E. Steinfeld, J. Trancik, and H. Tuller, "The future of solar energy," Massachusetts Institute of Technology, Boston, MA., Interdisciplinary Study, 2014, p. 327. [Online]. Available: http://energy.mit.edu/research/future-solar-energy/ (visited on 10/18/2017).

[11] G. F. I. Forum, "A technology roadmap for generation iv nuclear energy systems," United States Department of Energy, Tech. Rep. GIF-002-00, Dec. 2002, pp. 1–97. DOI: 10.2172/859029. [Online]. Available: http://www.osti.gov/servlets/purl/859029-304XRr/.

[12] GIF, *Gif portal - home*, 2018. [Online]. Available: https://www.gen-4.org/gif/jcms/c%7B%5C_%7D9260/public (visited on 12/27/2018).

[13] P. Sabjarwall, M. Ebner, M. Sohal, P. Sharpe, M. Anderson, K. Sridharan, J. Ambrosek, L. Olson, and P. Brooks, "Molten salts for high temperature reactors : University of wisconsin molten salt corrosion and flow loop experiments – issues identified and path forward," Idaho National Laboratory, Idaho Falls, ID, Tech. Rep. INL/EXT-10-8090, Mar. 2010, p. 43.

[14] M. Sohal, M. Ebner, P. Sabharwall, and P. Sharpe, "Engineering database of liquid salt thermophysical and thermochemical properties," Idaho National Laboratory, Idaho Falls, ID, Tech. Rep. INL/EXT-10-18297 Rev. 1, Jun. 2013, p. 71.

[15] P. F. Peterson and H. Zhao, "A flexible base-line design for the advanced high- temperature reactor utilizing metallic reactor internals (ahtr-mi)," in *Proceedings of ICAPP*, International Congress on Advanced Power Plants, Jun. 2006, pp. 8–9.

[16] T. Allen, S. Ball, E. Blandford, T. Downar, G. Flanagan, C. Forsberg, E. Greenspan, D. Holcomb, L.-W. Hu, R. Matzie, J. McGaha, D. Mears, M. Memmot, P. Peterson, J. Rushton, R. Schleicher, F. Silady, A. Stanculescu, C. Stoots, R. Wright, A. Cisneros, M. Laufer, R. Scarlat, N. Zweibaum, and J. Seifried, "Fluoride-salt-cooled, high-temperature reactor (fhr) subsystems definition, functional requirement definition, and licensing basis event (lbe) identification white paper," University of California, Berkeley, Berkeley, CA, Tech. Rep. UCBTH-12-001, Aug. 2013, p. 104.

[17] C. W. Forsberg, P. F. Peterson, and L. Ott, "The advanced high-temperature reactor (ahtr) for producing hydrogen to manufacture liquid fuels the advanced high-temperature reactor (ahtr) for producing hydrogen to manufacture liquid fuels," Oak Ridge National Laboratory, Miami Beach, Florida, Tech. Rep., Oct. 2004, pp. 1–13.

[18] C. Forsberg, P. Peterson, and T. Allen, "High-temperature salt-cooled reactor for power and process heat," Massachusetts Institute of Technology, Tech. Rep., 2011, p. 1. [Online]. Available: https://neup.inl.gov/SiteAssets/General%20Documents/11-3272%7B%5C_%7DTechnical%7B%5C_%7DAbstractMIT.pdf.

[19] J. W. Ambrosek, "Molten chloride salts for heat transfer in nuclear systems," PhD Thesis, University of Wisconsin - Madison, 2011.

[20] TerraPower, Ed. (May 14, 2020). "Molten chloride fast reactor technology," [Online]. Available: https://www.terrapower.com/our-work/molten-chloride-fast-reactor-technology/ (visited on 12/30/2017).

[21] K. Power. (May 14, 2020). "Home page," [Online]. Available: http://www.kairospower.com (visited on 06/22/2019).

[22] T. Power. (Sep. 13, 2019). "Thorcon power - home," [Online]. Available: http://thorconpower.com/ (visited on 12/30/2017).

[23] M. Energy. (May 14, 2020). "Stable salt reactors," [Online]. Available: http://www.moltexenergy.com/ (visited on 12/30/2017).

[24] E. Industries. (Oct. 16, 2020). "Elysium technology," [Online]. Available: http://www.elysiumindustries.com/technology (visited on 10/16/2020).

[25] F. E. Inc. (Sep. 23, 2020). "Technology | lftr overview," [Online]. Available: https://flibe-energy.com/technology.

[26] D. E. Holcomb and S. M. Cetiner, "An overview of liquid-fluoride-salt heat transport systems," Oak Ridge National Laboratory, Tech. Rep. ORNL–TM-2010-156, Sep. 2010, p. 88. DOI: 10.2172/990239. [Online]. Available: http://www.researchgate.net/publication/228742569%7B%5C_%7DAn%7B%5C_%7DOverview%7B%5C_%7Dof%7B%5C_%7DLiquid-Fluoride-Salt%7B%5C_%7DHeat%7B%5C_%7DTransport%7B%5C_%7DSystems.

[27] L. J. Mullins, "Plutonium electrorefining," Los Alamos Scientific Laboratory of the University of California, Tech. Rep., Feb. 1962. [Online]. Available: https://search.library.wisc.edu/catalog/9912646855002121.

[28] D. L. Grimmett, S. P. Fusselman, J. J. Roy, R. L. Gay, C. L. Krueger, T. S. Storvick, T. Inoue, T. Hijikata, and N. Takahashi, *Separation of actinides from lanthanides utilizing molten salt electrorefining*, English. Minerals, Metals and Materials Society, Warrendale, PA (United States), Oct. 1, 1996. [Online]. Available: https://www.osti.gov/biblio/372094.

[29] A. Kononov, S. Kuznetsov, and E. Polyakov, "Electrorefining in molten salts - an effective method of high purity tantalum, hafnium and scandium metal production," *Journal of Alloys and Compounds*, Jul. 8, 1994.

[30] J. B. Rosenbaum, *Electrowinning chromium metal*. U.S. Dept. of the Interior, Bureau of Mines, 1957. [Online]. Available: https://search.library.wisc.edu/catalog/9910054129302121.

[31] V. Nunes, C. Queirós, M. Lourenco, F. Santos, and C. Nieto de Castro, "Molten salts as engineering fluids – a review," *Applied Energy*, vol. 183, pp. 603–611, Dec. 2016, ISSN: 0306-2619. DOI: 10.1016/j.apenergy.2016.09.003.

[32] C. S. Turchi, J. Vidal, and M. Bauer, "Molten salt power towers operating at 600-650 c: Salt selection and cost benefits," *Solar Energy*, vol. 164, Mar. 2018. DOI: 10.1016/j.solener.2018.01.063.

[33] M. Liu, N. S. Tay, S. Bell, M. Belusko, R. Jacob, G. Will, W. Saman, and F. Bruno, "Review on concentrating solar power plants and new developments in high temperature thermal energy storage technologies," *Renewable and Sustainable Energy Reviews*, vol. 53, pp. 1411–1432, Jan. 2016. DOI: 10.1016/j.rser.2015.09.026.

[34] H. G. MacPherson, "The molten salt reactor adventure," *Nuclear Science and Engineering*, vol. 90, no. 4, pp. 374–380, 1985, ISSN: 0029-5639. DOI: 10.13182/NSE90-374.

[35] M. W. Rosenthal, P. R. Kasten, and R. B. Briggs, "Molten-salt reactors — history , status , and potential," *Nuclear Applied Technology*, vol. 8, p. 12, 1969.

[36] J. A. Lane, H. G. Macpherson, and F. Maslan, Eds., *Fluid Fuel Reactors*, English, 1st ed., ed. by J. Lane, ed. by F. Maslan, Library of Congress No. 58-12600. Reading, MA.: Addison-Wesley Publishing Co., 1958, p. 979.

[37] S. E. Beall, S. I. Kaplan, and D. B. Hall, "Design and construction of experimental homogeneous reactors," in *Fluid Fuel Reactors*, J. A. Lane, Ed., First, Oak Ridge, TN: Addison-Wesley Pub. Co., 1958, ch. 7, p. 68.

[38] H. Mochizuki, "Neutronics and thermal-hydraulics coupling analysis using the fluent code and the relap5-3d code for a molten salt fast reactor," *Nuclear Engineering and Design*, vol. 368, p. 110 793, Nov. 2020. DOI: 10.1016/j.nucengdes.2020.110793.

[39] C. Forsberg, L.-W. Hu, P. Peterson, and K. Sridharan, "Fluoride-salt-cooled high-temperature reactor (fhr) for power and process heat reactor concepts integrated research project," Massechusetts Institute of Technology, Tech. Rep. MIT-ANP-TR-157, 2014, p. 63. [Online]. Available: https://neup.inl.gov/SiteAssets/Final%20Reports/FY%202011/11-3272%20NEUP%20Final%20Report.pdf.

[40] C. W. Forsberg, N. Sepulveda, and K. Dawson, "Commercialization basis for fluoride-salt-cooled high-temperature reactors," Center for Advanced Nuclear Energy Systems, Massachusetts Institute of Technology, Cambridge, MA, Tech. Rep., Aug. 2018, p. 73.

[41] C. W. Forsberg, P. Peterson, K. Sridharan, L.-w. Hu, M. Fratoni, and A. Kant Prinja, "Integrated fhr technology development: Tritium management, materials testing, salt chemistry control, thermal hydraulics and neutronics, associated benchmarking and commercial basis," Massachusetts Institute of Technology, Cambridge, MA, Tech. Rep. MIT-ANP-TR-180, Oct. 2018, p. 534.

[42] T. Allen, S. Ball, E. Blandford, T. Downar, G. Flanagan, C. Forsberg, E. Greenspan, D. Holcomb, L.-W. Hu, R. Matzie, J. McGaha, D. Mears, M. Memmot, P. Peterson, J. Rushton, R. Schleicher, F. Silady, A. Stanculescu, C. Stoots, R. Wright, A. Cisneros, M. Laufer, R. Scarlat, N. Zweibaum, J. Seifried, G. Cao, T. Gerczak, B. Kelleher, G. Zheng, D. Carpenter, B. Romatoski, J. Stempien, A. Cisneros, and L. Huddar, "Fluoride-salt-cooled, high temperature reactor (fhr) materials, fuels and components white paper panel," University of Wisconsin - Madison, Madison, WI, Tech. Rep. UCBTH-12-003, Jul. 2013, p. 163.

[43] R. Hu, L. Zou, and G. Hu, "SAM user's guide," Argon National Laboratory, Tech. Rep. ANL/NSE-19/18, Aug. 2019, 166 pp.

[44] J. Ambrosek, M. Anderson, K. Sridharan, and T. Allen, "Current status of knowledge of the fluoride salt (flinak) heat transfer," *Nuclear Technology*, vol. 165, no. 2, pp. 166–173, 2009, ISSN: 0029-5450. DOI: 10.13182/NT165-166.

[45] A. Kuchibhotla, D. Banerjee, and V. Dhir, "Forced convection heat transfer of molten salts: A review," *Nuclear Engineering and Design*, vol. 362, p. 110 591, 2020, ISSN: 0029-5493. DOI: https://doi.org/10.1016/j.nucengdes.2020.110591. [Online]. Available: http://www.sciencedirect.com/science/article/pii/S0029549320300868.

[46] M. J. (Nielsen and C. B. (Ellis, "Aircraft nuclear propulsion project quarterly progress report for period ending may 31, 1950," Oak Ridge National Laboratory, Oak Ridge, Tennessee, Tech. Rep. ORNL-768, May 1950, p. 104.

[47] W. B. (Cottrell, "Aircraft nuclear propulsion project quarterly progress report for period ending december 10, 1952," Oak Ridge National Laboratory, Oak Ridge, Tennessee, Tech. Rep. ORNL-1439, Dec. 1952, p. 225.

[48] ——, "Aircraft nuclear propulsion project quarterly progress report for period ending december 10, 1953," Oak Ridge National Laboratory, Oak Ridge, Tennessee, Tech. Rep. ORNL-1649, Dec. 1953, p. 152.

[49] M. D. Grele and L. Gedeon, "Forced-convection heat-transfer characteristics of molten flinak flowing in an inconel x system," National Advisory Committee for Aeronautics, Cleveland, OH, Tech. Rep. RM-E53L18, Feb. 1954, p. 24. [Online]. Available: https://digital.library.unt.edu/ark:/67531/metadc59947/m1/2/%7B%5C#%7D.

[50] H. W. Hoffman and J. Lones, "Fused salt heat transfer-part ii. forced convection heat transfer in circular tubes containing naf-kf-lif eutectic," Oak Ridge National Laboratory (ORNL), Oak Ridge, Tennessee, Tech. Rep. ORNL-1777, Feb. 1955, p. 49. DOI: 10.2172/4016896. [Online]. Available: http://www.osti.gov/servlets/purl/4016896/.

[51] W. B. (Cottrell, "Aircraft nuclear propulsion project quarterly progress report for period ending june 10, 1953," Oak Ridge National Laboratory, Oak Ridge, Tennessee, Tech. Rep. ORNL-1556, Jun. 1953, p. 142.

[52] ——, "Aircraft nuclear propulsion project quarterly progress report for period ending september 10, 1953," Oak Ridge National Laboratory, Oak Ridge, Tennessee, Tech. Rep. ORNL-1609, Sep. 1953, p. 172.

[53] W. H. Jordan, S. J. Cromer, R. I. Strough, A. J. Miller, and A. W. (Savolainen, "Aircraft nuclear propulsion project quarterly progress report for period ending september 10, 1954," Oak Ridge National Laboratory, Tech. Rep. ORNL-1771, Sep. 1954, p. 185.

[54] B. Vriesema, "Aspects of molten fluorides as heat transfer agents for power generation," Doctoral Thesis, TU Delft, Feb. 1979, p. 294. [Online]. Available: https://repository.tudelft.nl/islandora/object/uuid%7B%5C%7D3A9e8deede-eebe-4621-b962-d4afcc2a5038.

[55] V. V. Ignatiev, S. V. Keronovskii, A. I. Surenkov, O. P. Shcherbanyuk, S. P. Manchkha, and Y. B. Smirnov, "Heat exchange during the flow of a melt of lif-naf-kf fluoride salts in a circular tube," *Soviet Atomic Energy*, vol. 57, no. 2, pp. 560–562, Aug. 1984, ISSN: 0038-531X. DOI: 10.1007/BF01123760.

[56] M. V. Smirnov, V. A. Khokhlov, and E. S. Filatov, "Thermal conductivity of molten alkali halides and their mixtures," *Electrochimica Acta*, vol. 32, no. 7, pp. 1019–1026, 1987, ISSN: 0013-4686. DOI: 10.1016/0013-4686(87)90027-2.

[57] M. W. Rosenthal, R. B. Briggs, and P. R. Kasten, "Molten-salt reactor program semiannual progress report for period ending february 28, 1967," Oak Ridge National Laboratory, Oak Ridge, TN (United States), Tech. Rep. ORNL-4119, Feb. 1967, p. 230.

[58] ——, "Molten-salt reactor program semiannual progress report for period ending august 31, 1967," Oak Ridge National Laboratory, Oak Ridge, TN (United States), Tech. Rep. ORNL-4191, Aug. 1967, p. 270.

[59] ——, "Molten-salt reactor program semiannual progress report for period ending february 29, 1968," Oak Ridge National Laboratory, Oak Ridge, Tennessee, USA, Tech. Rep. ORNL-4254, Feb. 1968, p. 302.

[60] ——, "Molten-salt reactor program semiannual progress report for period ending august 31, 1968," Oak Ridge National Laboratory, Oak Ridge, Tennessee, USA, Tech. Rep. ORNL-4344, Aug. 1968, p. 359.

[61] ——, "Molten-salt reactor program semiannual progress report for period ending february 28, 1970," Oak Ridge National Laboratory, Oak Ridge, Tennessee, USA, Tech. Rep. ORNL-4548, Feb. 1970, p. 364. DOI: 10.1016/S0140-6736(00)58800-X. [Online]. Available: http://linkinghub.elsevier.com/retrieve/pii/S014067360058800X.

[62] R. B. Briggs, "Molten-salt reactor program semiannular progress report for period ending august 31, 1966," Oak Ridge National Laboratory, Oak Ridge, TN (United States), Tech. Rep. ORNL-4037, Aug. 1966, p. 260.

[63] W. R. Huntley and P. A. Gnadt, "Design and operation of a forced-circulation corrosion test facility (msr-fcl-1) employing hastelloy n alloy and sodium fluoroborate salt," Oak Ridge National Lab, Tech. Rep. ORNL-TM-3863, Jan. 1973.

[64] M. D. Silverman, W. R. Huntley, and H. E. Robertson, "Heat transfer measurements in a forced convection loop with two molten-fluoride salts: Lif-bef2-thf2-ufq and eutectic nabf4-naf," Oak Ridge National Laboratory, Oak Ridge, TN, Tech. Rep. ORNL-TM-5335, 1976, p. 33.

[65] J. W. Cooke and B. Cox, "Forced-convection heat-transfer measurements with a molten fluoride salt mixture," Oak Ridge National Laboratory, Oak Ridge, TN, Tech. Rep. ORNL-TM-4079, Mar. 1973, p. 66.

[66] H. E. McCoy, "The inor-8 story," *Oak Ridge National Laboratory Review*, pp. 35–49, 1969.

[67] M. W. Rosenthal, R. B. Briggs, and P. N. Haubenreich, "Molten-salt reactor program semiannual progress report for period ending february 28, 1971," Oak Ridge National Laboratory, Oak Ridge, TN (United States), Tech. Rep. ORNL-4676, Feb. 1971, p. 301.

[68] H. Schlichting and K. Gersten, "Boundary layer theory," in, 9th ed. Springer-Verlag, Oct. 25, 2016, ch. 15. Onset of Turbulence (Stability Theory), pp. 415–497, ISBN: 978-3-662-52917-1. DOI: 10.1007/978-3-662-52919-5. [Online]. Available: https://www.ebook.de/de/product/26287559/hermann_schlichting_klaus_gersten_boundary_layer_theory.html.

[69] V. V. Ignatyev, V. M. Novikov, and A. I. Surenkov, "Heat transfer in closed thermosyphons as applied to molten salt reactor designs," *Kerntechnik*, vol. 54, no. 1, pp. 44–50, 1989.

[70] V. M. B. Nunes, M. J. V. Lourenco, F. J. V. Santos, and C. A. Nieto de Castro, "Importance of accurate data on viscosity and thermal conductivity in molten salts applications," *Journal of chemical and Engineering Data*, 2003. DOI: 10.1021/JE020160L.

[71] A. K. Das, M. M. Clark, B. C. Teigen, W. A. Fiveland, and M. H. Anderson, "Heat transfer behavior of molten nitrate salt," in *AIP Conference Proceedings*, vol. 1734, American Institute of Physics, 2016, p. 040 003, ISBN: 9780735413863. DOI: 10.1063/1.4949094.

[72] W. Yu-ting, L. Bin, M. Chong-fang, and G. Hang, "Convective heat transfer in the laminar-turbulent transition region with molten salt in a circular tube," *Experimental Thermal and Fluid Science*, vol. 33, no. 7, pp. 1128–1132, 2009. DOI: 10.1016/j.expthermflusci.2009.07.001.

[73] L. Bin, W. Yu-ting, M. Chong-fang, Y. Meng, and G. Hang, "Turbulent convective heat transfer with molten salt in a circular pipe," *International Communications in Heat and Mass Transfer*, vol. 36, no. 9, pp. 912–916, 2009, ISSN: 0735-1933. DOI: 10.1016/j.icheatmasstransfer.2009.06.003.

[74] J. Lu, X. Shen, D. Jing, P. Qiang, and Y. Wen, "Convective heat transfer of high temperature molten salt in transversely grooved tube," *Applied Thermal Engineering*, vol. 61, no. 2, pp. 157–162, 2013, ISSN: 1359-4311. DOI: 10.1016/j.applthermaleng.2013.07.037.

[75] J. Lu, S. He, J. Liang, J. Ding, and J. Yang, "Convective heat transfer in the laminar-turbulent transition region of molten salt in annular passage," *Experimental Thermal and Fluid Science*, vol. 51, pp. 71–76, 2013, ISSN: 0894-1777. DOI: 10.1016/j.expthermflusci.2013.07.002.

[76] H. Kim, H. Kim, S. Lee, and J. Kim, "A study on heat transfer characteristics of quinary molten salt mixture," *International Journal of Heat and Mass Transfer*, vol. 127, pp. 465–472, Dec. 2018, ISSN: 0017-9310. DOI: 10.1016/J.IJHEATMASSTRANSFER.2018.08.029. [Online]. Available: https://www-sciencedirect-com.ezproxy.library.wisc.edu/science/article/pii/S0017931018315333.

[77] B.-C. Du, Y.-L. He, Y. Qiu, Q. Liang, and Y.-P. Zhou, "Investigation on heat transfer characteristics of molten salt in a shell-and-tube heat exchanger," *International Communications in Heat and Mass Transfer*, vol. 96, pp. 61–68, Aug. 2018, ISSN: 0735-1933. DOI: 10.1016/J.ICHEATMASSTRANSFER.2018.05.020. [Online]. Available: https://www-sciencedirect-com.ezproxy.library.wisc.edu/science/article/pii/S0735193318301313.

[78] Y. Qiu, M.-J. Li, W.-Q. Wang, B.-C. Du, and K. Wang, "An experimental study on the heat transfer performance of a prototype molten-salt rod baffle heat exchanger for concentrated solar power," *Energy*, vol. 156, pp. 63–72, Aug. 2018, ISSN: 0360-5442. DOI: 10.1016/J.ENERGY.2018.05.040. [Online]. Available: https://www-sciencedirect-com.ezproxy.library.wisc.edu/science/article/pii/S0360544218308600.

[79] Z. Huang, Y. Zou, J. Ding, and J. Lu, "Experimental investigation of heat transfer in coiled tube type molten salt steam generator," *Applied Thermal Engineering*, vol. 148, pp. 1131–1138, Feb. 2019, ISSN: 1359-4311. DOI: 10.1016/J.APPLTHERMALENG.2018.11.118. [Online]. Available: https://www-sciencedirect-com.ezproxy.library.wisc.edu/science/article/pii/S1359431118348786.

[80] W. H. Jordan and A. W. (Savolainen, "Aircraft nuclear propulsion project quarterly progress report for period ending june 10, 1955," Oak Ridge National Laboratory, Oak Ridge, Tennessee, Tech. Rep. ORNL-1896, Jun. 1955, p. 248.

[81] ——, "Aircraft nuclear propulsion project quarterly progress report for period ending september 10, 1955," Oak Ridge National Laboratory, Oak Ridge, Tennessee, Tech. Rep. ORNL-1947, Sep. 1955, p. 238.

[82] W. H. Jordan, S. J. Cromer, A. J. Miller, and A. W. Savolainen, "Aircraft nuclear propulsion project quarterly progress report for period ending december 10, 1955," Oak Ridge National Laboratory, Tech. Rep. ORNL-2012, Dec. 1955, p. 247.

[83] E. S. Bettis, E. R. Cottrell W. B..and Mann, J. L. Meem, and G. D. Whitman, "The aircraft reactor experiment-operation," *Nuclear Science and Engineering*, vol. 2, pp. 841–853, Jun. 13, 1957.

[84] W. H. Jordan, S. J. Cromer, and A. J. Miller, "Aircraft nuclear purpolsion project quarterly progress report for period ending september 10, 1956," Oak Ridge National Laboratory, Oak Ridge, Tennessee, Tech. Rep. ORNL-2157, Sep. 1956, p. 330.

[85] ——, "Aircraft nuclear propulsion project quarterly progress report for period ending december 31, 1956," Oak Ridge National Laboratory, Oak Ridge, Tennessee, Tech. Rep. ORNL-2221, Dec. 1956, p. 398.

[86] J. C. Amos, R. E. MacPherson, and R. L. Senn, "Preliminary report of fused salt mixture no. 130 heat transfer coefficient test," Oak Ridge National Laboratory, Oak Ridge, Tennessee, USA, Tech. Rep. ORNL-CFN-58-4-23, Apr. 1958, p. 50.

[87] M. M. Yarosh, "Evaluation of the performance of liquid metal and molten salt heat exchangers," *Nuclear Science and Engineering*, vol. 8, no. 1, pp. 32–43, 1960. DOI: 10.13182/NSE8-1-32. eprint: https://doi.org/10.13182/NSE8-1-32. [Online]. Available: https://doi.org/10.13182/NSE8-1-32.

[88] W. H. Jordan, S. J. Cromer, R. I. Strough, A. J. Miller, and A. W. Savolainen, "Aircraft nuclear propulsion project quarterly progress report for period ending december 10, 1954," Oak Ridge National Laboratory, Tech. Rep. ORNL-1816, Dec. 1954, p. 179.

[89] D. F. Salmon, "Turbulent heat transfer from a molten fluoride salt mixture to sodium-potassium alloy in a double-tube heat exchanger," Oak Ridge National Laboratory (ORNL), Oak Ridge, TN (United States), Tech. Rep. ORNL-1716, Nov. 1954, p. 32. DOI: 10.2172/4224867. [Online]. Available: http://www.osti.gov/servlets/purl/4224867/.

[90] D. F. Williams, L. M. Toth, and K. T. Clarno, "Assessment of candidate molten salt coolants for the advanced high-temperature reactor," English, Oak Ridge National Laboratory, Nuclear Science and Technology Division, Tech. Rep. March, Mar. 2006, p. 86.

[91] G. M. Adamson, R. S. Crouse, and W. D. Manly, "Interim report on corrosion by zirconium-base fluorides: Work to may 1, 1953," English, Oak Ridge National Laboratory, Tennessee, Tech. Rep. ORNL-2337, Mar. 1959, p. 45.

[92] ——, "Interim report on corrosion by zirconium-base fluorides," English, Oak Ridge National Laboratory, Tennessee, Tech. Rep. ORNL-2338, Jan. 1961, p. 67.

[93] H. G. MacPherson, "Molten-salt reactor program quarterly progress report for periods ending january 31 and april 30, 1960," Oak Ridge National Laboratory, Oak Ridge, TN (United States), Tech. Rep. ORNL-2973, Apr. 1960, p. 104.

[94] L. McNeese, "Molten-salt reactor program semiannual progress report for period ending february 29, 1975," Oak Ridge National Laboratory, Oak Ridge, Tennessee, USA, Tech. Rep. ORNL-5047, Feb. 1975, p. 208.

[95] B. C. Kelleher, "Purification and chemical control of molten li2bef4 for a fluoride satl cooled reactor," Ph.D. dissertation, University of Wisconsin - Madison, 2015.

[96] L. E. McNeese, "Molten-salt reactor program semiannual progress report for period ending february 29, 1976," English, Oak Ridge National Laboratory, Tech. Rep. ORNL-5132, Feb. 1976, p. 218.

[97] R. R. Romatoski and L. W. Hu, "Fluoride salt coolant properties for nuclear reactor applications: A review," English, *Annals of Nuclear Energy*, vol. 109, pp. 635–647, 2017.

[98] G. Nellis and S. Klein, *Heat Transfer*, en, 1st ed. New York, NY: Cambridge University Press, 2010. [Online]. Available: http://www.cambridge.org/us/academic/subjects/engineering/thermal-fluids-engineering/heat-transfer (visited on 04/09/2018).

[99] R. Greif, Y. Zvirin, and M. A., "The transient and stability behavior of a natural circulation convection loop," *Journal of Heat Transfer*, vol. 101, pp. 684–688, Nov. 1979.

[100] K. Chen, "The optimum configuration of natural convection loops," *Solar Energy*, vol. 34, no. 4-5, pp. 407–416, Nov. 1985, ISSN: 0038-092X. DOI: 10.1016/0038-092X(85)90052-0.

[101] Y. Zvirin, "A review of naturall circulation loops in pressurized water reactors and other systems," *Nuclear Engineering and Design*, pp. 203–255, 67 Aug. 1981.

[102] M. Misale, "Overview on single-phase natural circulation loops," in *Proceedings of the Intational Conference on Advances In Mechanical And Automation Engineering*, 2014, pp. 1–12. DOI: 10.15224/978-1-63248-022-4-101.

[103] D. Ruiz, A. Cammi, and L. Luzzi, "Dynamic stability of natural circulation loops for single phase fluids with internal heat generation," *Chemical Engineering Science*, vol. 126, pp. 573–583, 2015, ISSN: 0009-2509. DOI: 10.1016/j.ces.2014.12.050. [Online]. Available: http://www.sciencedirect.com/science/article/pii/S0009250914007696.

[104] G. Song, D. Wu, R. Sun, Y. Liang, D. Zhang, J. Deng, G. Su, W. Tian, and S. Qiu, "Theoretical study of steady-state characteristics of natural circulation system," *Annals of Nuclear Energy*, vol. 147, p. 107 663, Nov. 2020. DOI: 10.1016/j.anucene.2020.107663.

[105] D. R. Oliver, "The effect of natural convection on viscous-flow heat transfer in horizontal tubes," *Chemical Engineering Schience*, vol. 17, pp. 335–350, 1962.

[106] C. A. Depew and S. E. August, "Heat transfer due to forced and free convection in a horizontal and isothermal tube," *Journal of Heat Transfer*, Nov. 1971. [Online]. Available: http://asmedigitalcollection.asme.org/.

[107] S. M. Morcos and A. E. Bergles, "Experimental investigation of combined forced and free laminar convection in horizontal tubes," *Journal of Heat Transfer*, vol. 97, no. 2, pp. 212–219, May 1975, ISSN: 0022-1481. DOI: 10.1115/1.3450343. eprint: https://asmedigitalcollection.asme.org/heattransfer/article-pdf/97/2/212/5909106/2121.pdf. [Online]. Available: https://doi.org/10.1115/1.3450343.

[108] S. W. Hong and A. E. Bergles, "Theoretical solutions for combined forced and free convection in horizontal tubes with temperature-dependent viscosity," *Journal of Heat Transfer*, vol. 98, no. 3, pp. 459–465, Aug. 1976, ISSN: 0022-1481. DOI: 10.1115/1.3450576. eprint: https://asmedigitalcollection.asme.org/heattransfer/article-pdf/98/3/459/5744375/4591.pdf. [Online]. Available: https://doi.org/10.1115/1.3450576.

[109] ". Meyer and M. Everts", ""single-phase mixed convection of developing and fully developed flow in smooth horizontal circular tubes in the laminar and transitional flow regimes"," *International journal of heat and mass transfer*, vol. 109, p. 109 890, Oct. 17, 2017, ISSN: "0894-1777". DOI: 10.1016/j.expthermflusci.2019.109890. [Online]. Available: http://www.sciencedirect.com/science/article/pii/S0894177719304315.

[110] J. Meyer, A. Bashir, and M. Everts, "Single-phase mixed convective heat transfer and pressure drop in the laminar and transitional flow regimes in smooth inclined tubes heated at a constant heat flux," *Experimental Thermal and Fluid Science*, vol. 109, p. 109 890, 2019, ISSN: 0894-1777. DOI: 10.1016/j.expthermflusci.2019.109890. [Online]. Available: http://www.sciencedirect.com/science/article/pii/S0894177719304315.

[111] J. P. Meyer and M. Everts, "A review of the recent developments in laminar, transitional, quasi-turbulent and turbulent forced and mixed convective flow through horizontal tubes," in *Advances in Heat Transfer*, Elsevier, 2019, pp. 131–205. DOI: 10.1016/bs.aiht.2019.07.001.

[112] J. D. Jackson, M. A. Cotton, and B. P. Axcell, "Studies of mixed convection in vertical tubes," *International Journal of Heat and Fluid Flow*, vol. 10, no. 1, pp. 2, 15, 1989, ISSN: 0142-727X. DOI: https://doi.org/10.1016/0142-727X(89)90049-0. [Online]. Available: http://www.sciencedirect.com/science/article/pii/0142727X89900490.

[113] T. Aicher and H. Martin, "New correlations for mixed turbulent natural and forced convection heat transfer in vertical tubes," *International Journal of Heat and Mass Transfer*, vol. 40, no. 15, pp. 3617–3626, 1997.

[114] W. Grassi and D. Testi, "Developing upward flow in a uniformly heated circular duct under transitional mixed convection," *International Journal of Thermal Sciences*, vol. 45, no. 9, pp. 932–937, Sep. 2006. DOI: 10.1016/j.ijthermalsci.2005.11.007.

[115] H. W. Hoffman, "Fused-salt heat transfer," Oak Ridge National Laboratory, Tech. Rep. CF-56-7-885, Nov. 1956.

[116] R. B. Briggs, "Molten-salt reactor program progress report for period from august 1, 1960, to february 28, 1961," English, Oak Ridge National Laboratory, Tech. Rep. ORNL-3122, Feb. 1961, p. 175.

[117] W. M. Kays and H. C. Perkins, "Forced convection, internal flow in ducts," in *Handbook of Heat Transfer Fundamentals*, W. M. Rohsenow, J. P. Hartnett, and E. N. Ganić, Eds., 2nd ed. New York, NY: McGraw-Hill, 1985, ch. 7, p. 180, ISBN: 0-07-053554-X.

[118] J. W. Koger, "Alloy compatibility with lif-bef2 salts containing thf4 and uf4," Oak Ridge National Laboratory, Tech. Rep. ORNL-TM-4286, Dec. 1972, 52 pp.

[119] L. Inc. (2017). "Odisi-b." en-US, Luna, [Online]. Available: http://lunainc.com/product/sensing-solutions/odisi/ (visited on 04/11/2018).

[120] M. T. Weathered, "Characterization of sodium thermal hydraulics with optical fiber temperature sensors," PhD, University of Wisconsin - Madison, 2017, p. 295.

[121] M. Weathered, J. Rein, M. Anderson, P. Brooks, and B. Coddington, "Characterization of thermal striping in liquid sodium with optical fiber sensors," *Journal of Nuclear Engineering and Radiation Science*, vol. 3, no. 4, Oct. 2017. DOI: 10.1115/1.4037118.

[122] M. T. Weathered and M. H. Anderson, "On the development of a robust optical fiber-based level sensor," *IEEE Sensors Journal*, vol. 18, no. 2, pp. 583–588, Jan. 2018. DOI: 10.1109/jsen.2017.2777801.

[123] H. Doniger William, "Electrochemistry for corrosion prevention in molten li2bef4 (flibe) salt for fluoride salt-cooled reactors," Masters of Science, University of Wisconsin - Madison, May 2018.

[124] C. Poresky, "Frequency response testing in the CIET facility," M.S. thesis, University of California - Berkeley, 2017.

[125] D. de Wet, P. F. Peterson, and M. S. Greenwood, "A frequency response approach to model validation for the compact integral effects test facility in transform," English, in *Proceedings of the 18th International Topical Meeting on Nuclear Reactor Thermal Hudraulics*, United States, Aug. 1, 2019. [Online]. Available: https://www.osti.gov/biblio/1570910.

[126] D. de Wet and K. Britsch, "Frequency reponse of the uw ncfl email communication," Email, Sep. 17, 2018.

[127] K. P. Dolan, "Redox potential measurement and control for the fluoride-salt-cooled high-temperature reactor," M.S. thesis, University of Wisconsin - Madison, 2015. [Online]. Available: https://search.library.wisc.edu/catalog/9912182343802121.

[128] W. H. Doniger and K. Sridharan, "Application of voltammetry for quantitative analysis of chromium in molten 2lif-bef2 (flibe) salt," *Journal of Electroanalytical Chemistry*, vol. 838, pp. 73–81, Apr. 2019. DOI: 10.1016/j.jelechem.2019.02.048.

[129] T. J. Chrobak, "Corrosion of candidate materials in molten flibe salt for application in fluoride-salt cooled reactors," M.S. thesis, University of Wisconsin – Madison, Jan. 2018, 215 pp.

[130] P. Brooks, "Dip salt sampler," AutoCad Drawing, Sep. 1, 2020.

[131] MATLAB, *version 9.7.0 (R2019b Update 3)*. Natick, Massachusetts: The Mathworks Inc, Sep. 2019. [Online]. Available: https://www.mathworks.com/help/stats/index.html?s_tid=CRUX_lftnav.

[132] S. A. Klein, *Ees engineering equation solver*, 10th ed., F-Chart Software, F-Chart Software, 2018, p. 344. [Online]. Available: http://www.fchart.com/ees/.

[133] ANSYS. (Feb. 2020). "Fluent r 19.0," ANSYS, [Online]. Available: https://www.ansys.com/products/fluids/ansys-fluent.

[134] A. Inc., "Fluent theory guide," in. ANSYS Inc, 2019, ch. 4.6.1 Transition SST Model, p. 4, Online accessed 2020-02-27. [Online]. Available: https://ansyshelp.ansys.com/account/secured?returnurl=/Views/Secured/corp/v190/flu_th/flu_th_sec_turb_transition.html.

[135] G. Cao, S. Weber, S. Martin, K. Sridharan, M. Anderson, and T. Allen, "Spectral emissivity of candidate alloys for very high temperature reactors in high temperature air environment," *Journal of Nuclear Materials*, vol. 441, no. 1, pp. 667–673, 2013, ISSN: 0022-3115. DOI: https://doi.org/10.1016/j.jnucmat.2013.04.083. [Online]. Available: http://www.sciencedirect.com/science/article/pii/S0022311513007010.

[136] MTLAB, *Statistics and Machine Learning Toolbox*. Natick, Massachusetts: The Mathworks Inc, Sep. 2019. [Online]. Available: https://www.mathworks.com/help/stats/index.html?s_tid=CRUX_lftnav.

[137] W. Derdeyn, M. Abou Dbai, R. O. Scarlat, and M. Trujillo, "Flibe radiative heat transfer," in *Transactions of the American Nuclear Society*, vol. 118, Philadelphia, PA: American Nuclear Society, 2018, pp. 1075–1078.

[138] C. Coyle, E. Baglietto, and C. Forsberg, "Advancing radiative heat transfer modeling in high-temperature liquid salts," *Nuclear Science and Engineering*, vol. 0, no. 0, pp. 1–11, 2020. DOI: 10.1080/00295639.2020.1723993. eprint: https://doi.org/10.1080/00295639.2020.1723993. [Online]. Available: https://doi.org/10.1080/00295639.2020.1723993.

[139] G. P. Celata, F. Dannibale, A. Chiardadia, and M. Cumo, "Upfow turbulent mixed convection heat transfer in vertical pipes," *International Journal of Heat and Mass Transfer*, vol. 41, pp. 4037–4054, Apr. 29, 1998.

[140] E. N. Sieder and G. E. Tate, "Heat transfer and pressure drop of liquids in tubes," *Heat transfer and pressure drop of liquids in tubes*, vol. 28, no. 12, pp. 1429–1435, Dec. 1936.

[141] P. T. C. S. Committee, "Test uncertainty," American Society of Mechanical Engieers, Tech. Rep. AMSE PTC 19.1-2005, version 2005, Oct. 13, 2006, 92 pp., Electronic.

[142] J. T. Nakos, "Uncertainty analysis of thermocouple measurements used in normal and abnormal thermal environment experiments at sandias radiant heat facility and lurance canyon burn site.," en, Sandia National Laboratory, Tech. Rep. SAND2004-1023, 918777, Apr. 2004. DOI: 10.2172/918777. [Online]. Available: http://www.osti.gov/servlets/purl/918777-6up8yW/ (visited on 06/26/2018).

[143] Y. Ho C and K. Chu T, "Electrical resistivity and thermal conductivity of nine selected aisi stainless steels," Center for Information, Numerical Data Analysis, and Synthesis, Purdue Industrial Research Park 2595 Yeager Road West Lafayatte, IN, 47906, Tech. Rep., Sep. 1977.

[144] *High temperature heaters - ceramic fiber heaters*, Watlow, 2016.

[145] *Flexible aerogel insulation for industrial applications*, Aspen Aerogels, 30 Forbes Rd Bldg B Northborough, MA 01532 USA, 2017.

[146] *High temperature microporous insulation*, Promat International N.V., Bormstraat 24 B-2830 Tisselt Belgium, May 2014.

[147] "Kaowool blanket," Morgan Advanced Materials, Tech. Rep., 2018.

[148] Kanthal, *Kanthal a-1*, Web, Feb. 2020. [Online]. Available: https://www.kanthal.com/en/products/material-datasheets/wire/resistance-heating-wire-and-resistance-wire/kanthal-a-1/.

A CALCULATIONS

A.1 Uncertainty

Measurement uncertainty is calculated following the recommendations of the American Society of Mechanical Engineers standard *Test Uncertainty: ASAME PTC 19.1-2005* [141]. For each instrument this starts by combining multiple sources in quadrature:

$$\eta = \sqrt{\sigma^2 + \epsilon_1^2 + \cdots + \epsilon_N^2}.$$

Here, σ is the measurement standard deviation and ϵ_n represent additional sources of uncertainty that are summarized for instruments in Table A.1, or are provided with the property correlations from Romatoski and Hu [97]. K-Type thermocouples additionally follow the recommendations of [142] and include contributions from the thermocouple standard-limits-of-error and a an additional 1.1 °C to account for the special-limits-of-error extension-wire. For air flow transducers, the manufacturer specifies their accuracy, which has been validated in a wind tunnel.

Calculating steady-state power input from radiant mode heaters relies on the observed variance of input voltage and resistance, which are 2 V and 1 Ω because there is no online monitoring. The coiled DC heaters are monitored, so therefore have a σ. Additionally, each "heater" is composed of six sub-coils run in parallel off one power supply. Each coil has uncertainty in length and a manufacturer specified tolerance for bulk resistivity. The DC power supplies were calibrated using a calibrated shunt and Agilent 34401A digital multi-meter, with the combined results for voltage and current reported in Table A.1 as the $I * V$ accuracy.

For the average heater surface temperatures, values, like the heater surface temperatures, the or mean salt temperature, the uncertainty uses the RMS average to capture the distance from a linear-trend prediction at that value [141]:

$$\eta_{RMS} = \sqrt{1/N \sum (\eta_n)^2}. \tag{A.1}$$

All other error-propagation is handled by EES, using numeric differentiation of function outputs

Table A.1: Measurement uncertainty in the NCFL.

Value	Sources	η Range
T_s	0.75% + 1.1 °C	4 to 9 °C
$T_{a,in}$	2.2 °C + 1.1 °C	2.5 °C
v_s	max(σ, 14%)	0.4 to 2.4 cm/s
$\dot{m}_a$	2.0%	0.18 to 0.80 g/s
$Q_{htr,Rad}$	5 %	43 to 87 W
Coiled contact heaters		
L	3.175 mm	2.168 to 2.175 m
ρ_e	5 %	2.437 to 2.452 Ω
$(I * V)_{P.S.}$	0.64 %	8.02 to 28.2 V A
Q_{htr}	5.29 %	60 to 200 W

(Y_n) with respect to input variables (X_n):

$$\eta_{EES} = \sqrt{\sum_n \left(\frac{\partial Y_n}{\partial X_n}\right)^2 \eta_{X_n}^2}. \tag{A.2}$$

A.2 Heat Balance and Conduction

Radial Conduction

Radial conduction is used to calculate temperature changes across tubing and the insulation as well as to estimate the thickness of a frozen salt layers. The equation used for all these calculations is:

$$Q = \frac{(T_o - T_i)}{R_n} \tag{A.3}$$

$$R_n = \frac{\ln (r_o/r_i)_n}{2\pi L\ k(\bar{T}_n)} \tag{A.4}$$

Typically, the unknown value is the temperature at the inner, T_i or outer T_o edge of a cylindrical shell n. This value is solved iteratively from Eq. (A.3), with the thermal conductivity of the material, k, evaluated at the average shell temperature, $\bar{T}_n = (T_o + T_i)/2$.

In the top cross cooler, calculations require the frozen layer thickness, knowing the wall temperature, T_o, and the salt freezing point, T_i. This permits solving the equation for the inner

radius, r_i.

Insulation Heat Losses

Insulation losses use the discretized cylindrical conduction equations to account for varying thermal conductivity of the insulation at temperature. This requires a iterative approach across discretized shells, bounded by the measured inner surface temperature, T_1, and the room air at T_∞. The constant heat loss , Q_{insul}, through all shells couples equations as:

$$Q_{insul} = \frac{(T_1 - T_2)}{R_1} \cdots = \frac{(T_n - T_{n+1})}{R_n}$$
$$Q_{insul} = \frac{(T_{insul,o} - T_\infty)}{h_\infty A_{s,o}}$$

Where the conduction resistance, R_n is given in Eq. (A.4), with the appropriate k from [143]–[147], evaluated at the average temperature for shell n, $(T_n + T_(n-1))/2$. The final T_N from the last shell is the insulation surface temperature, $T_{insul,o}$. This is used to calculate the free-convection coefficient, h_∞, from the horizontal or vertical cylinder correlations provided in Nellis and Klein [98]. As a final step in the calculation, $T_{insul,o}$ is verified against surface mounted TCs and infrared camera images, like those in Fig. C.7.

Fin conduction losses

In several locations along the heated side of the loop, conduction along instrument ports must be accounted for. This uses a simple infinite fin assumption from Nellis and Klein [98]

$$Q_{fin} = (T_b - T_\infty)\sqrt{\pi D\, h_\infty k_{316SS} A_c} \tag{A.5}$$

where h_∞ and T_∞ are the convection coefficient and temperature of the room air. The cross sectional area A_c is for the tube wall only, omitting any solid salt because the conductivity of the stainless steel tube (k_{316}) is more than $10\times$ greater. The base temperature is taken from the closest TC to the fin, which for the heaters applies to several surface TCs mounted directly at the instrument port base. These TCs and their locations are given in Tables B.3 and B.4

Cooler Heat Balance

Corrections to the top cross heat balance come from two sources, the fin-like end caps and air expansion. The end caps were treated as annular rectangular fins with an adiabatic tip

and a base temperature from T_{20} and T_{23} located on the wall upstream and downstream of the cooler. They convect energy to the inlet or outlet air temperature at the air speed as it enters the annulus.

$$Q_{fin,in} = h_{a,in} A_s (T_{a,in} - T_{20}) \eta_{fin} \tag{A.6}$$

$$Q_{fin,out} = h_{a,out} A_s (T_{a,out} - T_{23}) \eta_{fin} \tag{A.7}$$

η_{fin} is the appropriate fin effectiveness and the heat transfer coefficient is from the external plate correlation, both taken from [98]. Conduction along the tube is negligible at $<5\,W$.

The air expansion is also accounted for in the change in stagnation enthalpy

$$\Delta Q_0 = \dot{m}_a \left(v_{a,out}^2 - v_{a,in}^2 \right) / 2 \tag{A.8}$$

Heater Input Power

Power input from the radiant mode heaters is calculated from the control-percentage $(\%_{Htr})$ of the maximum power, as:

$$Q_{Htr,n} = 2 * \frac{E^2}{R_e(T)} * \%_{Htr}. \tag{A.9}$$

The equation is doubled to account for the two clamshell halves that make up each heater and operate in parallel. The supply voltage (E) is $208 \pm 2\,V$ and the cold resistance for each half (R_e) is $50 \pm 1\,\Omega$. At high temperatures, the temperature coefficient of resistance is used to correct $R_e(T)$, with a range of 1 to 1.04 between 400 to 1000 °C [148]

Radiation Heat Transfer

Radiation heat transfer in the heaters is calculated from

$$Q_{rad} = \frac{A_o \sigma_B (T_{htr,i,K}^4 - T_{w,o,K}^4)}{\frac{1}{\epsilon_{rad,1}} + \frac{1}{\epsilon_{rad,2}} - 1} \tag{A.10}$$

where the temperature values are converted to Kelvin scale, as denoted by the subscript K. The steel surface emissivity, $\epsilon_{rad,steel} = 0.5$ from a measurement of air oxidized stainless by Cao et. al. [135]. For heaters, $\epsilon_{rad,htrs} = 0.6$, from the heater manual [144].

B DIMENSIONS AND INSTRUMENTATION

B.1 Instrument and Sample Locations

Loop dimensions are given in Fig. B.5 and Table B.2 provides the distances used to calculate velocity. Table B.1 provides observed operating range across all tests.

Table B.1: Operating range

Value	Min	Max	Unit
$T_{s,hot}$	541	736	°C
$T_{s,cold}$	482	684	°C
$\bar{v}_s$	2.5	7.1	cm/s
ΔT_g	49	120	°C
$\dot{m}_{salt}$	14	44	g/s
$\dot{m}_{air}$	3.66	32.6	g/s
Radiant Heaters (2 per leg)			
Q	865	1731	W
Q''	7.35	14.7	MW/m^2
T_{face}	541	736	°C
Coiled heaters (1 per leg)			
Q	1276	4320	W
Q''	4.69	16.2	MW/m^2
T	541	1000	°C

Table B.2: Distances between TCs used in heat-pulse velocity calculations.

Start TC	End TC	Distance m
24	32	0.479
24	35	1.87
32	35	1.47

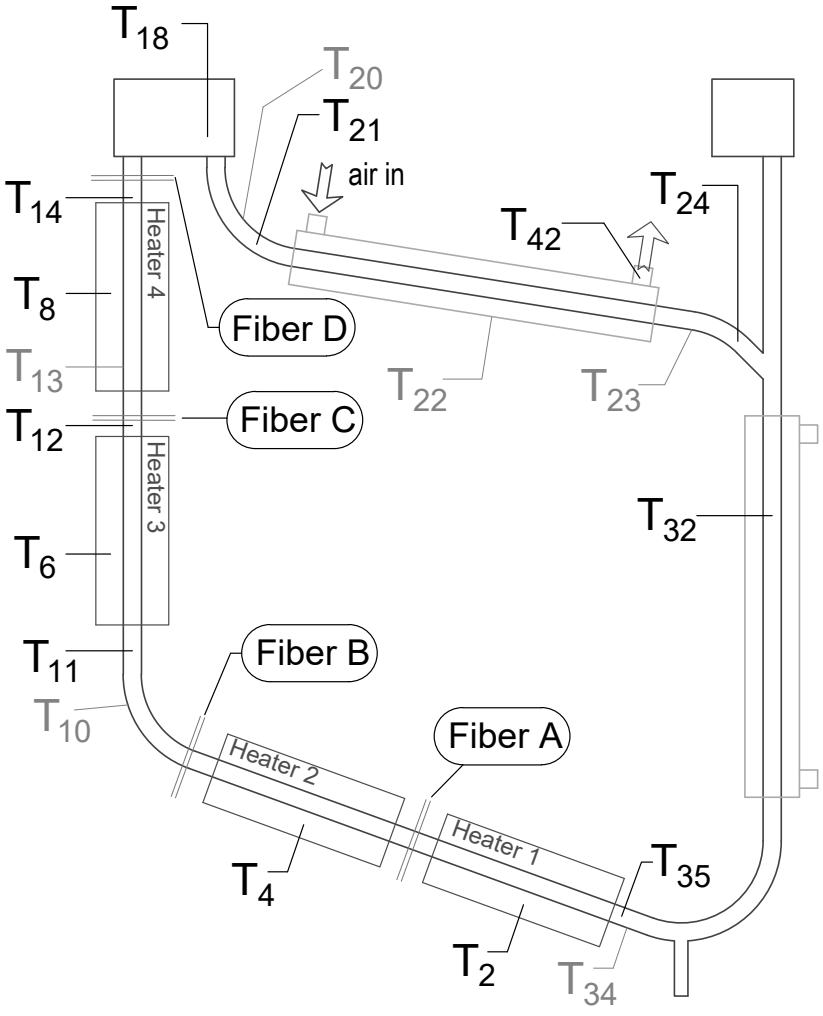

Figure B.1: Wetted thermocouples for all loop configurations and radiant heater TCs used up to C1 - C6.

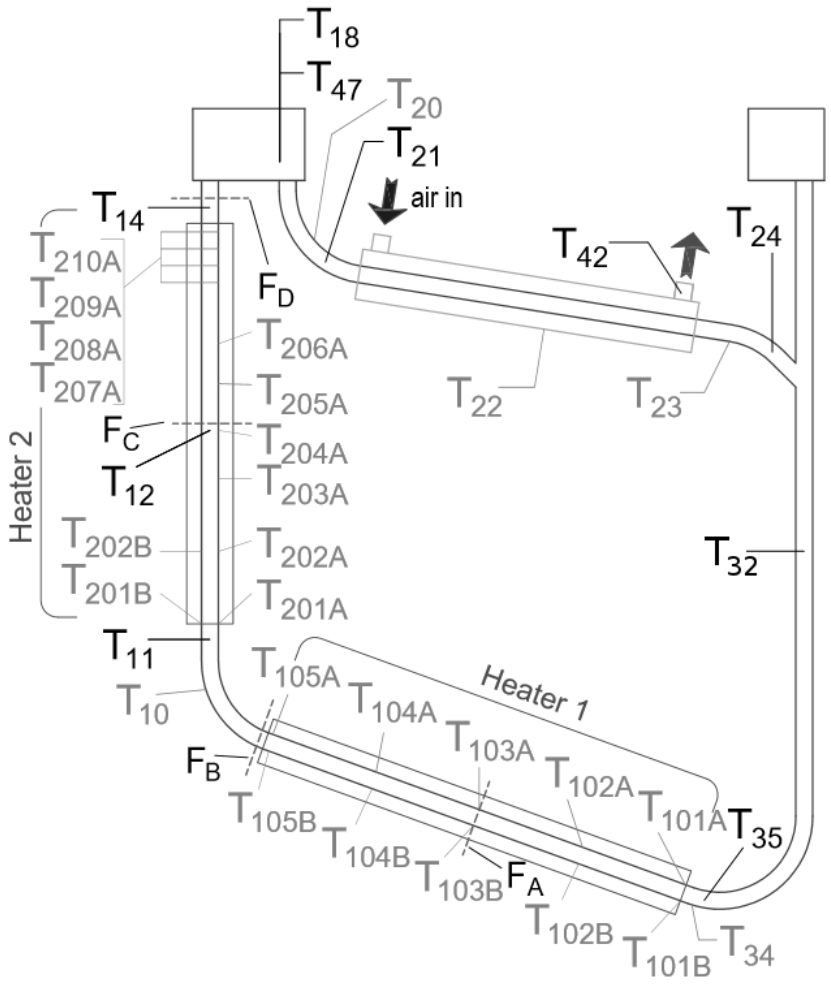

Figure B.2: New TC layout for heat transfer measurements during C7 to C9.

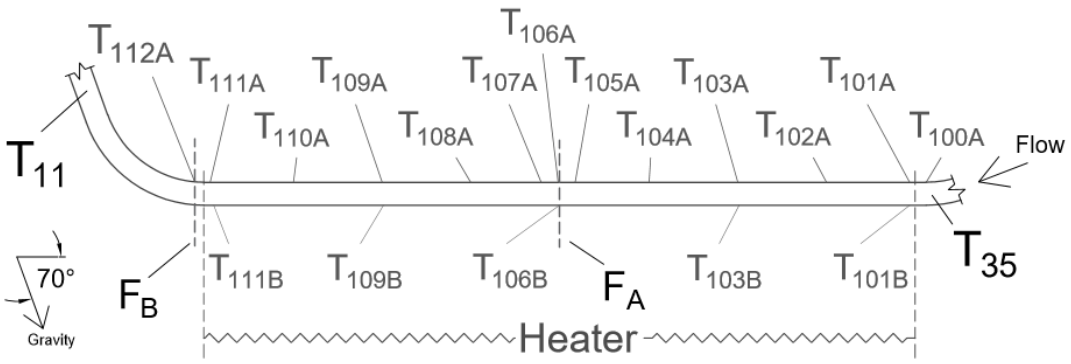

Figure B.3: Surface TCs for the bottom cross heater during Campaign 10.

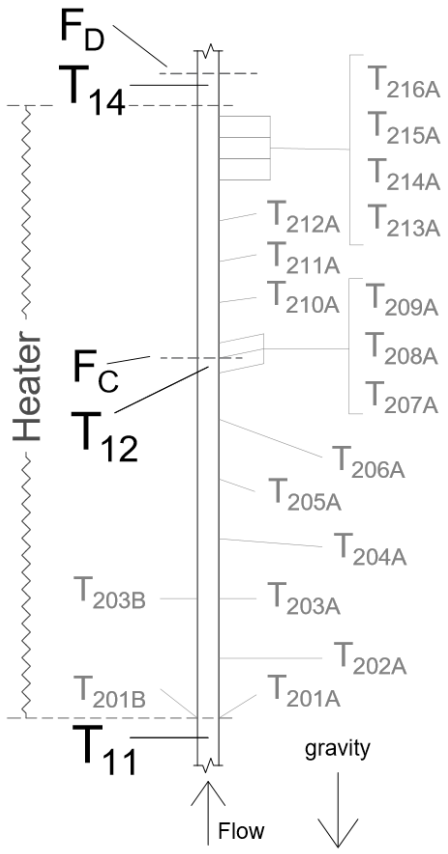

Figure B.4: Surface TCs on the riser heater during C10

B.2 As-built dimensions

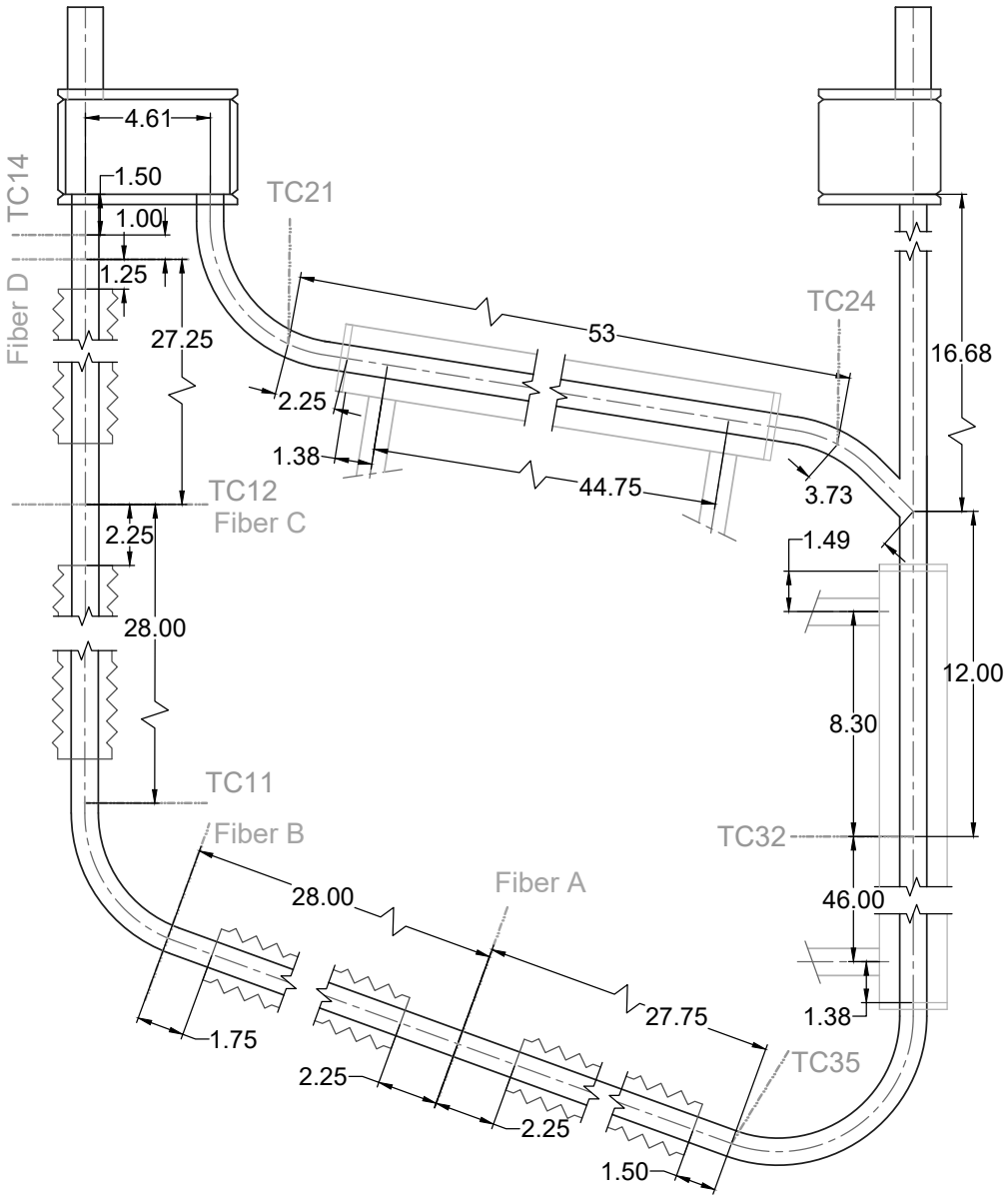

Figure B.5: As-built dimensions of the NC FLiBe Loop. All bends have a 12.7 cm (5 in) centerline radius. Heater positions are valid for the radiant mode heaters used through C6.

Table B.3: TC locations along the flow path (s) for Campaign 7 - 9. TCs A and B are on top vs. bottom of the bottom cross or the front/back of the riser.

Bottom Cross			Riser		
TC #	Alias #	s [cm]	TC #	Alias #	s [cm]
TC 34		0.000	TC10		0.000
TC 35		1.905	TC11		3.175
TC 2	101A	6.985	TC61	201A	6.033
TC 52	101B	6.985	TC62	201B	8.573
TC 53	103A	40.01	TC63	203A	28.58
TC 54	103B	39.05	TC64	205B	28.73
Fiber A		73.34	TC65	205A	51.44
TC55	106A	73.34	Fiber C		74.30
TC56	106B	73.34	TC66	208A	74.30
TC57	109A	106.0	TC12		74.93
TC58	109B	106.0	TC13	210A	88.90
TC59	111A	139.1	TC67	211A	99.70
TC60	111B	139.7	TC68	213A	125.1
Fiber B		144.8	TC4	214A	130.2
TC10		157.5	TC6	215A	135.6
			TC8	216A	140.3
			Fiber D		143.8
			TC14		145.1
			Tank Bottom		149.2

Table B.4: TC locations along the flow path for Campaign 10

Bottom Cross			Riser		
TC #	Alias #	s [cm]	TC #	Alias #	s [cm]
TC34		0.000	TC 10		0.000
TC 2	100A	2.381	TC 11		3.175
TC 52	101A	7.460	TC 69	201A	5.715
TC 53	101B	7.303	TC 70	201B	5.080
TC 54	102A	23.65	TC 71	202A	16.51
TC 55	103A	40.32	TC 72	203A	27.94
TC 56	103B	40.01	TC 73	203B	27.94
TC 57	104A	56.52	TC 74	204A	39.37
TC 58	105A	71.12	TC 75	205A	50.80
TC 59	106A	73.34	TC 76	206A	62.23
Fiber A		73.34	TC 77	207A	71.76
TC 60	106B	73.34	Fiber C		74.30
TC 61	107A	74.77	TC 78	208A	74.30
TC 62	108A	89.37	TC12		74.93
TC 63	109A	105.7	TC 79	209A	75.57
TC 64	109B	105.9	TC 80	210A	88.90
TC 65	110A	122.2	TC13		88.90
TC 66	111A	138.7	TC 81	211A	101.6
TC 67	111B	138.4	TC 82	212A	114.0
TC 68	112A	144.8	TC 83	213A	126.7
Fiber B		144.8	TC 4	214A	131.4
TC10		157.5	TC 6	215A	136.5
			TC 8	216A	141.6
			Fiber D		143.8
			TC 14		145.1
			Tank bottom		149.2

Table B.5: TC measurements that were inaccurate and corrected when calculating $\overline{T}_{w,o}$. Campaign 7 and 8 numbers are shown in Fig. B.2 at positions given in Table B.3, while C10 positions are shown in Figs. B.3 and B.4 at the positions given in Table B.4.

	C7 & C8	C10
BC - Top	106A	100A, 101A, 102A, 105A
BC - Bottom	106B	106B, 111B
Riser - Front	201A, 208A, 210A,	201A, 204A, 206A, 208A, 213A
Riser - Back	201B	201B

C IMAGES

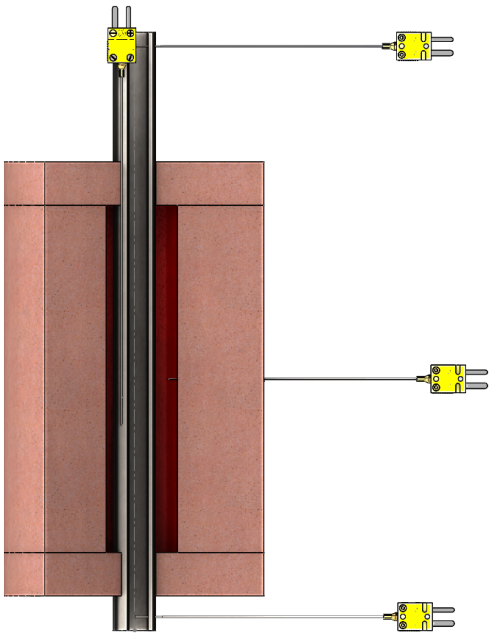

Figure C.1: Temperature measurements in the radiant mode heaters.

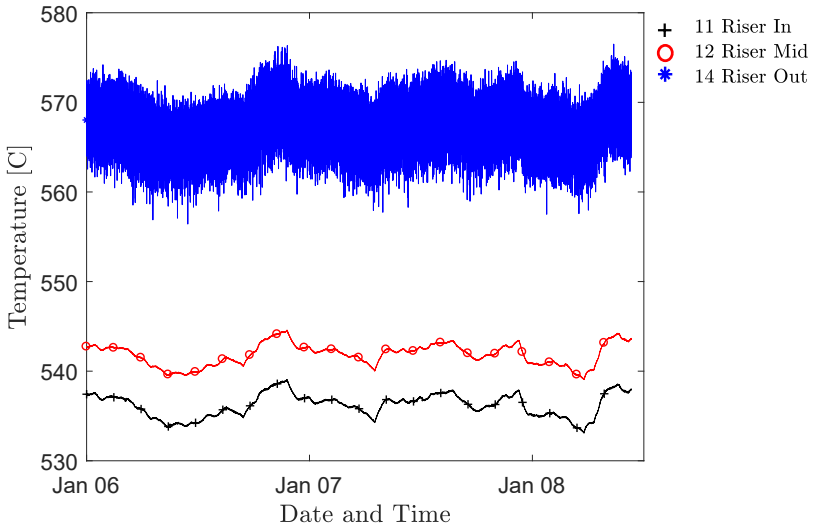

Figure C.2: A comparison of typical temperature readings showing the TC14 noise band.

Figure C.3: A temporary gap in the insulation for time-of-flight measurements using transients generated with a blow torch.

Figure C.4: The loop metal survived the blow torch test with minor discoloration.

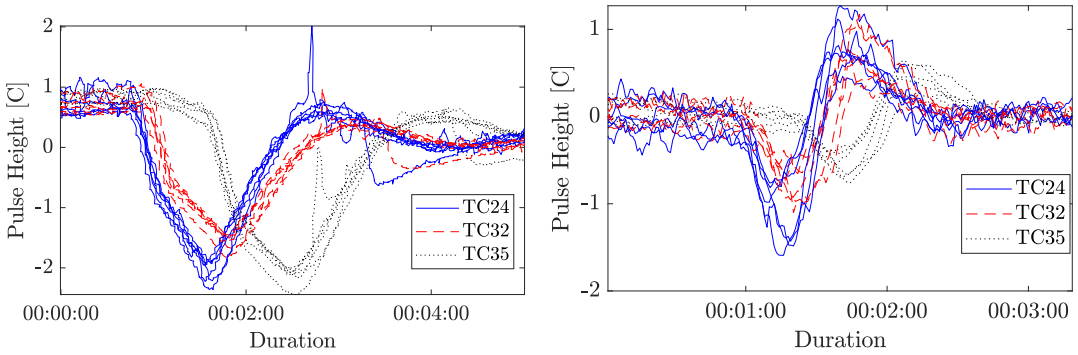

Figure C.5: Comparison of repeated blower-generated velocity pulses. On the left the flow speed is 3.3 cm/s while on the right, it is 7.3 cm/s.

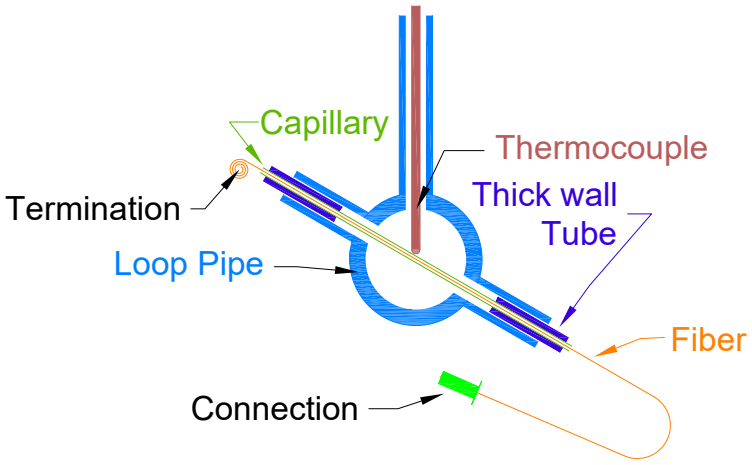

Figure C.6: Fiber C passing through the loop inside a capillary tube with TC12 sitting just above it.

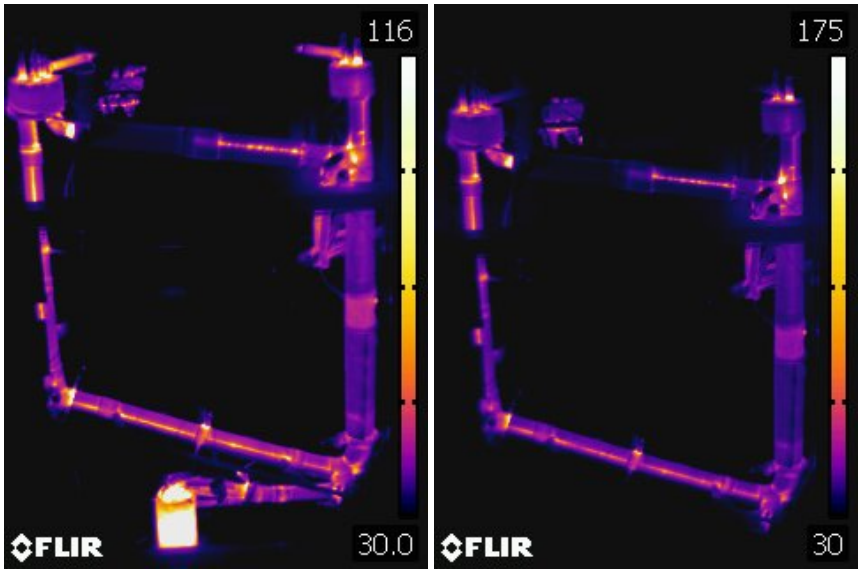

Figure C.7: IR images of the insulation surface temperatures during C7 used to verify loss calculations. On the left, heaters are operating at 1.8 kW and on the right, at 3.1 kW.

Figure C.8: Stainless oxide collecting at the bottom of heater 3 along the riser.

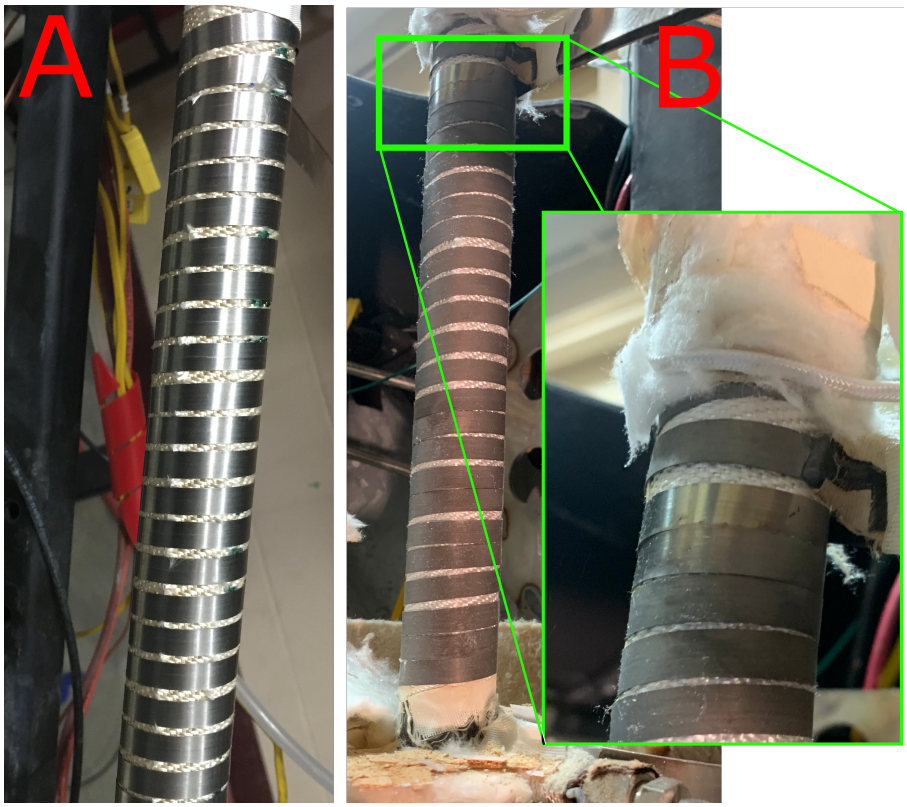

Figure C.9: Heater coils before (A) and after (B) operation. The zoomed in region clearly shows were the coils were shorted together and did not form an oxide.

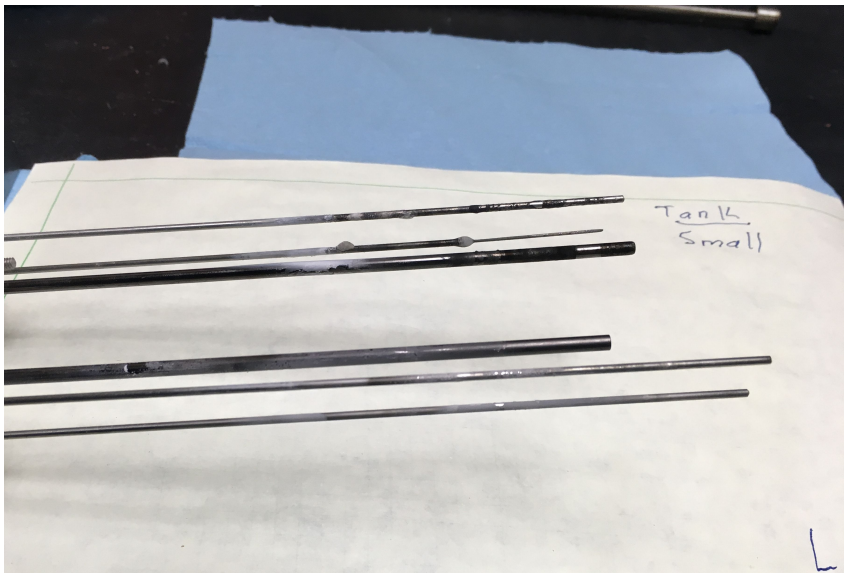

Figure C.10: First generation electrochemistry probes showing the deplated molybdenum electrode from the small tank.

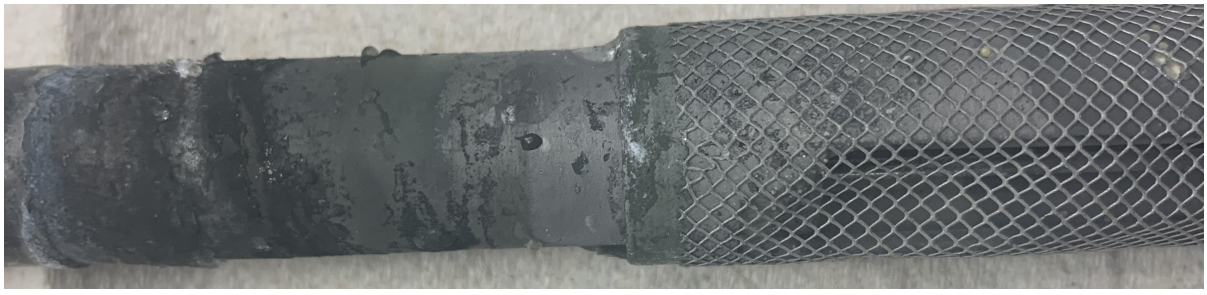

Figure C.11: Second generation electrochemistry probe with a nickel mesh that appears unaffected by the salt compared to the darker stainless steel tube.

Figure C.12: Post-operation loop metal.

D DATA

D.1 Result Data

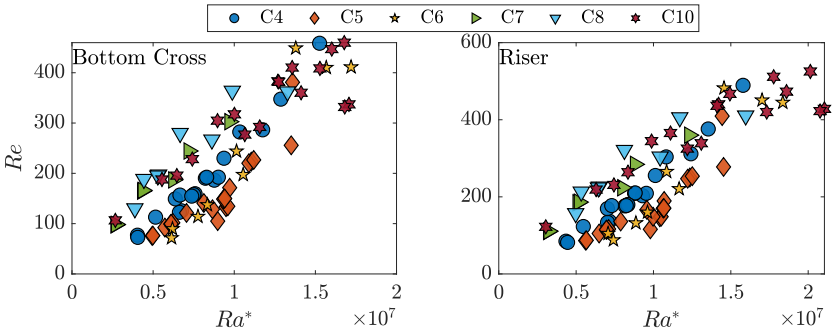

Figure D.1: Coupling ties Ra and Re across all campaigns.

Table D.1: RMS distance of Nu_{exp} from correlations in the top cross cooler.

Cooled:	All	Ra $\geqslant$ 1.5
Shah - Temp	3.36	2.06
Shah - Q″	2.09	1.03
Meyer and Everts	2.11	0.96

Table D.2: RMS Nu distance of heated Nu_s from correlations.

	BC			Riser		
Campaign	Hornbeck	Meyer	Sieder-Tate	Hornbeck	Hallman	Sieder-Tate
4	4.45	4.76	4.8271	1.12	0.85	1.26
5	0.90	0.74	0.952	0.81	2.02	0.566
6	0.77	0.76	0.874	0.84	1.63	0.849
7	9.31	9.69	9.85	2.90	2.94	3.50
8	10.43	10.82	10.9	3.81	4.07	4.39
10	5.36	5.82	5.80	0.65	0.66	1.01

Table D.3: RMS percent uncertainty in heated Nusselt for each campaign.

Campaign	BC (%)	R (%)
4	27.7	17.8
5	16.6	14.9
6	19.1	16.9
7	33.77	24.0
8	27.3	20.8
10	20.0	16.4

D.2 Exposure Times

Table D.4: Operational times including duration above 300 °C, duration with salt in the loop, and time spent with salt circulating. FA indicates a heated run to anneal fibers without any salt fill.

Campaign	Start time	Fill time	Dump	Cool down	Hot time	Filled time	Flowing Salt
1	6/1/17 10:00	6/2/17 11:30	6/3/17 14:45	6/3/17 16:45	54:45:00	27:15:00	NA
2	6/11/17 23:24	6/12/17 15:27	6/12/17 20:45	6/12/17 23:10	23:46:00	5:18:00	5:18:00
FA	8/9/17 16:28	NA	NA	8/11/17 0:26	31:58:00	NA	NA
3	8/12/17 19:00	8/13/17 15:21	8/15/17 9:57	8/15/17 12:22	65:22:00	42:35:40	42:35:40
FA	9/1/17 10:49	N A	NA	9/3/17 13:01	50:12:00	NA	NA
4	9/4/17 15:05	9/5/17 11:20	9/21/17 16:38	9/21/17 18:39	411:34:00	389:18:20	389:18:20
FA	12/4/17 18:10	NA	NA	12/7/17 13:03	66:53:00	NA	NA
5	1/3/18 11:15	1/3/18 18:39	1/31/18 19:02	1/31/18 21:27	682:12:00	672:23:08	672:23:08
6	7/23/18 14:49	7/23/18 20:51	9/2/18 18:00	9/2/18 20:00	989:11:00	981:09:00	981:09:00
7	1/21/20 9:15	1/21/20 15:32	2/3/20 18:41	2/3/20 19:33	322:18:00	315:09:00	315:09:00
8	6/19/20 19:14	6/19/20 19:23	7/2/20 18:40	7/2/20 20:04	312:50:00	311:17:00	311:17:00
9	7/14/20 11:34	7/14/20 16:15	7/18/20 9:50	7/18/20 10:40	95:06:00	89:35:00	NA
10	9/6/20 11:00	9/6/20 16:45	9/6/20 17:00	9/6/20 18:30	7:30:00	0:15:00	NA
	9/8/20 10:00	9/8/20 16:15	11/9/20 13:44	11/9/20 15:00	1493:00:00	1485:29:00	1485:29:00
					4606:37:00	4319:44:08	4202:39:08

Table D.5: Time-averagd temperatures per campaign for each material sample give in Fig. D.2.

Sample		Campaign Temperature [°C]									
		1	2	3	4	5	6	7	8	9	10
A	Surface	530	370	547	574	546	652	618	646	530	667
	Fluid	481	375	555	604	558	656	591	629	529	640
B	Surface	361	368	522	599	598	658	669	687	534	680
	Fluid	384	374	534	617	611	670	607	646	526	684
C	Surface	484	481	626	700	699	766	695	729	601	778
	Fluid	455	432	574	645	627	753	688	691	525	719
D	Surface	489	414	557	622	625	677	630	646	530	685
	Fluid	484	416	559	647	631	751	687	690	543	718
E	Surface	395	370	522	593	556	656	591	629	525	643
	Fluid	397	371	525	599	574	658	591	629	526	644
F	Surface	458	418	579	609	594	676	595	617	532	598
	Fluid	467	414	564	619	594	672	594	630	529	598
G	Surface	484	481	626	700	699	766	684	691	544	727
	Fluid	433	439	559	625	622	685	641	670	529	686

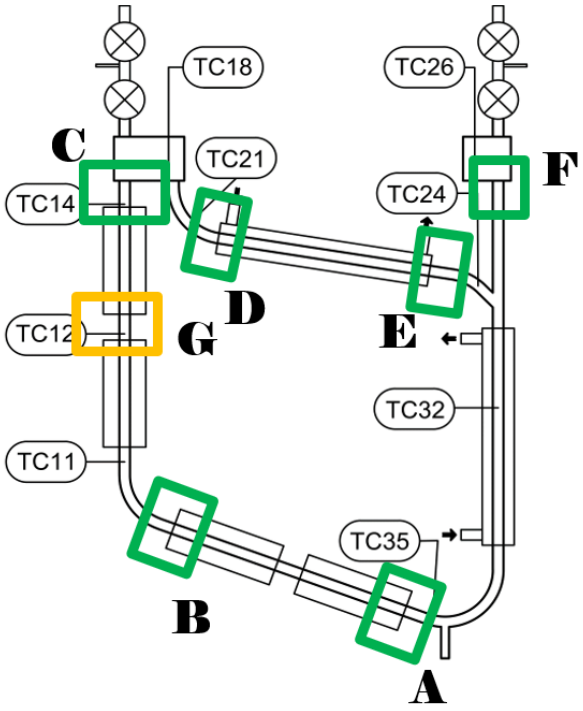

Figure D.2: Material sample locations

D.3 Salt Impurities

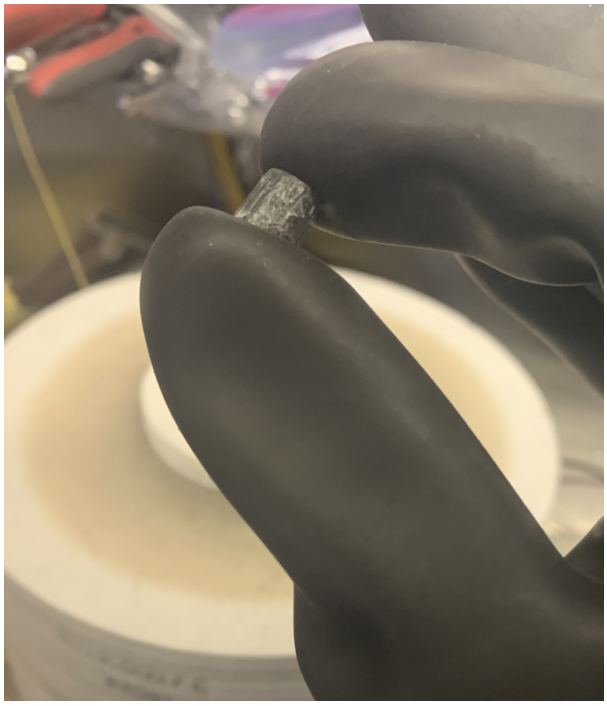

Figure D.3: Campaign 10 salt sample taken with dip tube, showing a uniform dark hue from impurities.

Table D.6: Salt impurity levels measured in ppm. Comparison data is provided in marked rows † and ‡ is of the first batch of salt used through Campaign 7. † from analysis by Brian Kelleher [95], data in row ‡ from analysis by W. Doniger [123]. Data in row ⋆ is the salt used in Campaigns 8 - 10, from a UWcollaboration with Kairos Power [21]. The C6 duplicate is solid pieces broken off the sample in Fig. 5.17, with (C) being the ground-up remains that clearly suffered contamination from processing.

Date	C	T_{Hot}	T_{Cold}	Al	Ca	Cr	Fe	Mg	Mn	Mo	Ni	K	Na
				Optical Emission Spectrometry									
2014	†	NA	NA	28.0	132.0	53.3	NaN	139.0	3.9	0.0	10.7	544.0	469.0
2017	‡	NA	450	33.7	114.3	6.4	NaN	136.3	4.2	0.0	14.5	448.3	493.7
9/1/2017	3	NA	450	29.9	0.0	556.6	280.0	171.4	49.2	0.0	28.3	2622.3	1992.0
11/1/2017	4	NA	450	74.4	108.0	121.1	325.6	130.4	21.2	0.0	14.8	370.6	394.5
				Mass Spectrometry									
9/1/2018	6 (A)	720	630	115.0	194.0	489.0	67.0	259.0	59.0	0.0	8.0	470.0	410.0
9/1/2018	6 (B)	720	630	68.0	162.0	103.0	95.5	232.0	45.5	0.1	0.3	399.0	334.0
9/1/2018	6 (C)	720	630	1250.0	205.0	533.0	805.0	247.0	75.0	10.0	63.0	469.0	417.0
1/22/2020	7	625	566	701.0	122.0	153.0	0.0	136.0	34.4	0.0	13.9	512.0	339.0
1/29/2020	7	633	566	9180.0	0.0	111.0	565.0	0.0	68.4	0.0	36.3	920.0	568.0
1/31/2020	7	650	603	2680.0	258.0	146.0	278.0	338.0	80.4	0.0	21.1	1050.0	706.0
2/3/2020	7	650	573	571.0	10.0	196.0	0.0	131.0	32.8	0.0	12.0	681.0	379.0
1/14/2019	⋆	NA	NA	41.0	158.0	297.0	253.0	169.0	45.0	3.0	12.0	338.0	299.0
6/25/2020	8	625	566	3700.0	132.0	8.6	244.0	106.0	15.0	1.7	10.8	351.0	2220.0
6/25/2020	8	625	566	1890.0	235.0	3.8	152.0	90.0	20.1	0.0	9.8	580.0	4060.0
9/10/2020	10	550	501	33.7	115.0	94.9	127.0	88.6	11.8	0.0	7.3	240.0	1720.0
9/12/2020	10	660	603	31.4	107.0	135.0	147.0	79.6	12.4	0.0	7.5	222.0	1580.0
9/14/2020	10	595	533	37.5	113.0	121.0	119.0	84.0	12.1	0.0	7.2	228.0	1690.0
9/16/2020	10	625	563	30.1	102.0	126.0	109.0	81.2	12.8	0.0	7.4	232.0	1740.0
9/18/2020	10	600	535	29.7	101.0	128.0	96.6	79.8	13.1	0.0	7.3	226.0	1690.0
9/24/2020	10	725	654	24.5	87.5	253.0	0.0	65.9	16.5	0.0	6.7	189.0	1440.0
9/30/2020	10	690	615	30.1	103.0	281.0	0.0	0.0	0.0	0.0	6.9	226.0	1700.0
10/6/2020	10	715	644	31.8	109.0	308.0	0.0	82.5	22.9	0.0	7.4	227.0	1720.0

D.4 Campaigns 4 and 5

NCFL data from Campaigns 4 and 5 for the ten selected tests referenced in Section 3.2.

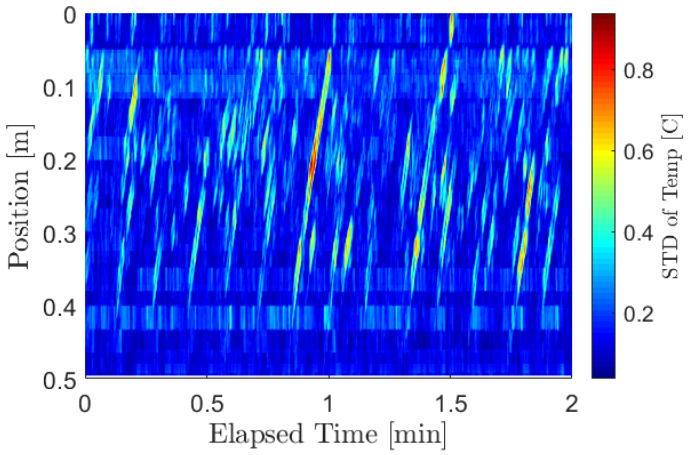

Figure D.4: Standard-deviation of the temperature history of Fiber F, during Test 3, showing eddies moving upward from the midpoint of Heater 4.

Table D.7: Fiber temperature gradients for the ten test conditions in °C/cm. Fibers A and B report the different gradients between the top wall and centerline and the centerline to bottom wall. Fibers C and D have symmetric average gradients.

Test	**Fiber A**		**Fiber B**		**Fiber C**	**Fiber D**
	Top	Bottom	Top	Bottom		
2	41.5	-9.45	37.6	-23.5	30.3	21.7
3	50.3	-10.6	42.7	-29.6	41.0	-4.02
4						33.8
5	40.0	-2.53	57.4	-26.9	46.7	19.5
6			54.8	-24.4	48.9	21.6
7	42.9	-0.981	60.3	-17.8	38.4	65.1
9	48.3	6.73				82.8

Table D.8: Summary of data from ten selected tests. $\overline{Re}$, and $\overline{Pr}$ are calculated at $\overline{T}$, which is the Hot-to-Cold average of TC21 and TC35.

Test	Duration	P_{heater}	v_{air}	$\overline{v}_{salt}$	$\overline{T}_{salt}$	ΔT	$\overline{Re}$	$\overline{Pr}$
	h	W	m/s	cm/s	°C	°C	[-]	[-]
1	5.02	952	2.23	2.75 ± 0.07	513 ± 9	59	79	31
2	16.77	1125	2.19	3.48 ± 0.64	574 ± 10	54	138	22
3	18.78	1298	2.19	5.76 ± 0.51	643 ± 11	50	313	15
4	20.43	1298	6.49	3.59 ± 0.11	534 ± 10	74	117	27
5	20.50	1471	2.16	6.72 ± 0.42	693 ± 13	55	448	12
6	17.42	1471	6.49	5.49 ± 0.65	593 ± 12	67	240	20
7	15.40	1471	9.19	5.07 ± 0.85	546 ± 10	75	175	25
8	17.78	1644	6.52	5.43 ± 1.8	606 ± 11	70	252	18
9	18.10	1644	9.17	4.31 ± 0.81	574 ± 10	76	172	22
10	8.05	1644	12.8	4.75 ± 0.27	547 ± 9	85	166	26

Table D.9: Air-flow conditions through the top-cross annular cooler.

Test #	v_{gap}	T_{in}	T_{out}	$T_{out\text{-}wall}$
	m/s	°C	°C	°C
1	2.23 ± 0.06	24.4 ± 3.1	301.2 ± 3.3	122.2 ± 3.1
2	2.19 ± 0.06	24.6 ± 3.1	360.4 ± 3.8	155.2 ± 3.3
3	2.19 ± 0.27	25.1 ± 3.1	430.7 ± 6.0	197.3 ± 3.7
4	6.49 ± 0.08	26.7 ± 3.1	193.5 ± 3.2	76.7 ± 3.1
5	2.16 ± 0.09	25.1 ± 3.1	490.3 ± 5.8	238.6 ± 4.2
6	6.49 ± 0.14	27.0 ± 3.1	226.2 ± 3.6	93.8 ± 3.2
7	9.19 ± 0.11	29.4 ± 3.1	158.0 ± 3.3	69.0 ± 3.2
8	6.52 ± 0.08	27.3 ± 3.1	240.5 ± 3.4	98.2 ± 3.2
9	9.17 ± 0.08	29.3 ± 3.1	183.9 ± 3.2	76.2 ± 3.1
10	12.8 ± 0.08	33.7 ± 3.1	144.1 ± 3.2	64.9 ± 3.1

Table D.10: Heat input from heaters

Test #	P_{heater} W	$T_{Face\ 1}$ °C	$T_{Face\ 2}$ °C	$T_{Face\ 3}$ °C	$T_{Face\ 4}$ °C	$T_{Tube\ Surf\ 4}$ °C
1	952	608 ± 5.1	631 ± 5.3	642 ± 5.4	656 ± 5.4	575 ± 4.9
2	1125	676 ± 5.8	699 ± 5.9	712 ± 6	724 ± 6.1	640 ± 5.5
3	1298	751 ± 6.5	771 ± 6.6	791 ± 6.8	798 ± 6.8	713 ± 6.2
4	1298	683 ± 5.8	716 ± 6.0	717 ± 6.0	713 ± 6.0	621 ± 5.3
5	1471	806 ± 7.4	831 ± 7.5	846 ± 7.6	845 ± 7.6	772 ± 7.1
6	1471	763 ± 7.7	769 ± 7.5	800 ± 7.9	802 ± 7.8	682 ± 7.0
7	1471	726 ± 6.3	731 ± 6.2	761 ± 6.5	765 ± 6.5	636 ± 5.5
8	1644	766 ± 6.5	808 ± 6.7	805 ± 6.7	793 ± 6.5	704 ± 6.0
9	1644	749 ± 6.3	791 ± 6.5	787 ± 6.4	779 ± 6.4	675 ± 5.6
10	1644	735 ± 6.1	779 ± 6.4	773 ± 6.3	762 ± 6.2	653 ± 5.4

Table D.11: Average non-dimensional terms for top-cross cooler. Preliminary Nu data is included for Campaign 4 and 5, denoted C4 and C5

Re	Pr	Gr	Gz	Nu C4	Nu C5
79.9	29.3	2.16E+04	38.9	3.59	
140	20.8	8.72E+04	48.4	3.06	
315	15.1	2.58E+05	78.8	5.41	
117	26.0	3.72E+04	50.6		3.74
453	12.1	5.16E+05	90.7	6.26	5.45
240	19.1	1.19E+05	76.1	4.59	
174	24.5	4.71E+04	71.2	3.89	
251	17.9	1.47E+05	75.1		4.85
170	21.2	8.26E+04	60.1		3.51
161	24.8	4.47E+04	66.9		5.36

Table D.12: Average non-dimensional terms for heat transfer on the hot side of the loop. Preliminary Nu data is included for Campaign 4 and 5, denoted C4 and C5

	Bottom-Cross						Riser					
Test	Re	Pr	Gr	Gz	Nu C4	Nu C5	Re	Pr	Gr	Gz	Nu C4	Nu C5
1	72.1	32.7	1.22E+04	31.3	6.55		83.0	28.2	1.62E+04	30.6	6.34	
2	129	22.7	2.67E+04	38.9	7.94		143	20.3	3.78E+04	38.1	6.95	
3	293	16.2	6.01E+04	63.4	8.50		322	14.7	7.61E+04	61.9	7.67	
4	105	29.1	3.58E+04	40.5	3.98		125	24.3	3.70E+04	39.6	5.16	
5	424	13.0	1.20E+05	72.9	9.65	4.75	465	11.8	1.37E+05	71.2	8.39	5.60
6	219	21.0	5.05E+04	61.1	8.13		249	18.4	6.73E+04	59.7	7.93	
7	158	27.3	3.10E+04	57.1	7.54		184	23.2	4.31E+04	55.8	7.67	
8	230	19.8	9.24E+04	60.3		4.19	262	17.2	9.16E+04	58.8		5.23
9	154	23.6	6.71E+04	48.2		4.41	178	20.3	7.08E+04	47.1		5.40
10	147	27.5	5.31E+04	53.5		4.13	177	22.6	5.48E+04	52.1		5.50

Table D.13: Measured salt temperatures for each of the ten tests in °C. The standard deviation of the measured value over each test highlights the degree of noise that occurred on some thermocouples.

Test #	TC11	std	TC12	std	TC14	std	TC21	std	TC24	std	TC32	std	TC35	std
1	514.1±4.5	0.9	520.8±4.5	0.8	535.9±4.7	1.2	542.3±4.7	0.7	490.4±4.4	0.8	487.9±4.4	0.8	483.4±4.3	0.8
2	576.3±5.0	1.3	580.4±5.1	1.3	592.0±5.1	1.3	600.9±5.2	1.3	553.1±4.9	1.4	550.4±4.9	1.4	546.7±4.9	1.5
3	638.5±5.6	1.9	645.9±5.7	2.0	669.1±6.0	2.4	667.6±5.9	2.1	620.9±5.4	1.6	619.0±5.7	2.4	617.4±5.5	2.1
4	538.6±4.7	0.0	543.8±4.8	0.1	569.9±5.4	2.1	571.4±4.9	0.1	502.1±4.5	0.1	496.8±4.5	0.1	497.4±4.5	0.1
5	692.2±6.6	2.5	699.8±6.6	2.4	722.0±6.9	3.2	720.5±6.7	2.7	672.7±6.7	2.9	675.7±6.6	2.8	665.7±6.4	2.5
6	590.7±6.0	3.3	597.6±6.2	3.6	623.0±8.8	7.1	626.8±6.1	3.3	562.3±5.9	3.4	560.8±5.8	3.3	560.2±6.2	4.0
7	548.8±4.8	1.3	553.8±4.9	1.3	572.7±5.8	3.1	583.4±5.1	1.4	510.2±5.1	2.5	509.5±4.7	1.7	508.2±4.7	1.6
8	603.9±5.3	0.1	611.5±5.4	0.1	638.7±6.7	3.7	641.4±5.6	0.6	572.6±5.3	0.1	567.2±5.3	0.1	571.3±5.2	0.1
9	572.5±4.9	0.1	578.9±4.9	0.1	600.2±6.6	4.2	612.0±5.2	0.3	536.2±4.7	0.1	529.3±4.8	0.1	535.6±4.7	0.1
10	549.9±4.7	0.1	556.0±4.8	0.1	587.0±6.1	3.6	589.8±5.0	0.2	499.2±4.6	0.2	500.0±4.4	0.1	504.6±4.4	0.1

D.5 Heat Transfer Data Campaigns 4 - 6

Table D.14: Heat balance data in kW.

#	$\dot{m}_s$	$\dot{m}_a$	Cooler		Q_{Htr}	Bottom Cross		Riser		C#
	g/s	g/s	Q_{ext}	ΔQ_s		Q_{ext}	ΔQ_s	Q_{ext}	ΔQ_s	
1	15.7 ± 2.2	3.68	1.87 ± 0.095	−1.76 ± 0.33	0.865	1.48 ± 0.087	0.881 ± 0.33	1.46 ± 0.087	0.655 ± 0.25	4
2	19.6 ± 2.8	3.67	2.03 ± 0.097	−2.14 ± 0.42	0.952	1.62 ± 0.095	1.12 ± 0.43	1.59 ± 0.095	0.696 ± 0.31	4
3	16.4 ± 2.3	5.69	2.12 ± 0.082	−2.17 ± 0.38	0.952	1.64 ± 0.095	1.05 ± 0.34	1.61 ± 0.095	0.856 ± 0.26	4
4	19.5 ± 3.4	5.63	2.63 ± 0.10	−2.39 ± 0.51	1.13	1.91 ± 0.11	1.21 ± 0.46	1.87 ± 0.11	0.733 ± 0.33	4
5	19.5 ± 3.4	5.59	2.57 ± 0.15	−2.40 ± 0.52	1.13	1.91 ± 0.11	1.23 ± 0.49	1.88 ± 0.11	0.726 ± 0.34	4
6	15.5 ± 6.3	5.60	2.52 ± 0.11	−2.10 ± 0.88	1.13	1.92 ± 0.11	1.58 ± 0.72	1.89 ± 0.11	1.43 ± 0.63	6
7	16.6 ± 2.3	10.1	2.58 ± 0.099	−2.55 ± 0.44	1.13	1.94 ± 0.11	1.32 ± 0.40	1.93 ± 0.11	1.26 ± 0.32	5
8	16.6 ± 2.3	10.2	2.62 ± 0.095	−2.57 ± 0.43	1.13	1.94 ± 0.11	1.32 ± 0.36	1.92 ± 0.11	1.26 ± 0.30	5
9	14.5 ± 3.3	9.87	2.94 ± 0.11	−2.61 ± 0.65	1.21	2.06 ± 0.12	1.66 ± 0.51	2.04 ± 0.12	1.61 ± 0.45	6
10	19.8 ± 4.3	12.2	2.89 ± 0.11	−3.15 ± 0.75	1.21	2.09 ± 0.12	1.57 ± 0.52	2.07 ± 0.12	1.40 ± 0.43	5
11	32.0 ± 4.5	5.59	3.27 ± 0.39	−3.73 ± 0.78	1.30	2.17 ± 0.13	1.48 ± 0.83	2.12 ± 0.13	2.33 ± 0.67	4
12	28.8 ± 15	5.49	3.20 ± 0.18	−2.61 ± 1.5	1.30	2.15 ± 0.13	1.76 ± 1.1	2.13 ± 0.13	2.19 ± 1.2	6
13	25.7 ± 6.8	7.64	3.28 ± 0.12	−3.41 ± 1.00	1.30	2.19 ± 0.13	1.49 ± 0.68	2.15 ± 0.13	1.24 ± 0.54	4
14	25.9 ± 6.9	7.67	2.96 ± 0.23	−3.82 ± 1.1	1.30	2.21 ± 0.13	1.73 ± 0.75	2.17 ± 0.13	1.78 ± 0.65	4
15	25.6 ± 6.8	7.54	3.33 ± 0.13	−3.38 ± 1.0	1.30	2.19 ± 0.13	1.45 ± 0.78	2.14 ± 0.13	1.29 ± 0.63	4
16	28.0 ± 3.9	9.79	3.40 ± 0.10	−4.01 ± 0.73	1.30	2.20 ± 0.13	1.86 ± 0.69	2.15 ± 0.13	1.38 ± 0.53	4
17	27.9 ± 3.9	9.77	3.41 ± 0.11	−3.86 ± 0.76	1.30	2.19 ± 0.13	1.71 ± 0.77	2.15 ± 0.13	1.42 ± 0.63	4
18	19.1 ± 2.7	9.77	3.27 ± 0.16	−2.91 ± 0.52	1.30	2.19 ± 0.13	1.92 ± 0.51	2.17 ± 0.13	1.82 ± 0.43	6
19	21.1 ± 2.9	12.2	3.27 ± 0.12	−3.32 ± 0.57	1.30	2.21 ± 0.13	1.73 ± 0.52	2.20 ± 0.13	1.41 ± 0.43	5
20	20.2 ± 2.8	16.2	3.27 ± 0.12	−3.49 ± 0.58	1.30	2.23 ± 0.13	1.90 ± 0.50	2.22 ± 0.13	1.52 ± 0.40	5
21	20.2 ± 2.8	16.7	3.30 ± 0.12	−3.54 ± 0.57	1.30	2.23 ± 0.13	1.96 ± 0.48	2.22 ± 0.13	1.53 ± 0.38	5
22	20.2 ± 2.8	16.5	3.31 ± 0.12	−3.51 ± 0.57	1.30	2.23 ± 0.13	1.94 ± 0.48	2.22 ± 0.13	1.50 ± 0.38	5
23	29.1 ± 4.1	18.9	3.27 ± 0.13	−4.83 ± 0.81	1.30	2.22 ± 0.13	2.55 ± 0.69	2.18 ± 0.13	1.55 ± 0.52	4
24	29.1 ± 4.1	18.9	3.43 ± 0.13	−4.84 ± 0.81	1.30	2.21 ± 0.13	2.51 ± 0.70	2.17 ± 0.13	1.50 ± 0.52	4
25	15.1 ± 2.1	5.78	2.89 ± 0.11	−2.29 ± 0.40	1.38	2.34 ± 0.14	0.953 ± 0.36	2.32 ± 0.14	1.34 ± 0.32	5
26	38.6 ± 5.4	5.41	3.97 ± 0.23	−4.48 ± 1.2	1.47	2.42 ± 0.15	1.86 ± 1.4	2.35 ± 0.15	2.72 ± 1.0	4
27	36.7 ± 5.1	5.61	3.65 ± 0.16	−4.48 ± 0.91	1.47	2.45 ± 0.15	1.88 ± 0.95	2.42 ± 0.15	2.64 ± 0.77	5
28	41.1 ± 11	5.43	3.66 ± 0.17	−3.35 ± 1.3	1.47	2.43 ± 0.15	2.20 ± 1.5	2.41 ± 0.15	3.16 ± 1.4	6
29	35.7 ± 5.0	7.57	4.02 ± 0.15	−4.47 ± 0.90	1.47	2.46 ± 0.15	1.76 ± 0.92	2.40 ± 0.15	2.74 ± 0.76	4
30	19.3 ± 8.7	6.50	3.04 ± 0.11	−3.05 ± 1.4	1.47	2.51 ± 0.15	1.24 ± 0.70	2.49 ± 0.15	1.78 ± 0.87	5
31	19.2 ± 8.7	6.50	3.05 ± 0.10	−2.99 ± 1.4	1.47	2.51 ± 0.15	1.19 ± 0.68	2.48 ± 0.15	1.76 ± 0.86	5
32	32.7 ± 4.6	9.84	4.12 ± 0.14	−4.30 ± 0.83	1.47	2.47 ± 0.15	1.63 ± 0.81	2.41 ± 0.15	2.65 ± 0.69	4
33	29.1 ± 4.1	9.78	3.79 ± 0.14	−3.70 ± 0.74	1.47	2.48 ± 0.15	2.02 ± 0.81	2.46 ± 0.15	2.35 ± 0.74	6
34	25.7 ± 3.6	12.1	3.86 ± 0.13	−3.99 ± 0.70	1.47	2.50 ± 0.15	1.75 ± 0.59	2.49 ± 0.15	1.88 ± 0.50	5
35	33.8 ± 5.0	16.5	4.00 ± 0.16	−5.34 ± 1.0	1.47	2.50 ± 0.15	2.39 ± 0.98	2.45 ± 0.15	2.61 ± 0.92	4
36	23.7 ± 3.3	16.3	3.77 ± 0.14	−3.87 ± 0.67	1.47	2.51 ± 0.15	2.47 ± 0.64	2.50 ± 0.15	2.15 ± 0.49	6
37	29.8 ± 4.2	23.1	3.49 ± 0.16	−5.29 ± 0.88	1.47	2.54 ± 0.15	2.79 ± 0.77	2.50 ± 0.15	1.68 ± 0.56	4
38	29.8 ± 4.2	23.1	3.50 ± 0.15	−5.27 ± 0.88	1.47	2.54 ± 0.15	2.77 ± 0.75	2.50 ± 0.15	1.66 ± 0.55	4
39	29.8 ± 4.2	23.2	3.46 ± 0.14	−5.35 ± 0.87	1.47	2.55 ± 0.15	2.86 ± 0.73	2.50 ± 0.15	1.76 ± 0.55	4
40	28.9 ± 8.8	7.74	4.04 ± 0.16	−3.88 ± 1.3	1.56	2.62 ± 0.16	1.50 ± 0.87	2.59 ± 0.16	2.11 ± 0.86	5
41	31.0 ± 7.7	16.5	4.33 ± 0.16	−5.32 ± 1.5	1.64	2.81 ± 0.16	2.49 ± 1.0	2.79 ± 0.16	2.58 ± 0.91	5
42	31.0 ± 7.7	16.6	4.30 ± 0.15	−5.38 ± 1.4	1.64	2.81 ± 0.16	2.54 ± 0.93	2.80 ± 0.16	2.54 ± 0.86	5
43	31.0 ± 7.7	16.5	4.37 ± 0.15	−5.26 ± 1.4	1.64	2.80 ± 0.16	2.43 ± 0.91	2.79 ± 0.16	2.60 ± 0.86	5
44	24.8 ± 3.5	23.1	4.23 ± 0.16	−4.68 ± 0.77	1.64	2.83 ± 0.16	2.30 ± 0.63	2.82 ± 0.16	1.64 ± 0.52	5
45	24.8 ± 3.5	23.0	4.21 ± 0.16	−4.70 ± 0.76	1.64	2.83 ± 0.16	2.34 ± 0.62	2.82 ± 0.16	1.65 ± 0.52	5
46	24.8 ± 3.5	23.2	4.26 ± 0.16	−4.66 ± 0.75	1.64	2.83 ± 0.16	2.27 ± 0.60	2.81 ± 0.16	1.64 ± 0.51	5
47	23.4 ± 3.3	27.5	4.15 ± 0.17	−4.56 ± 0.73	1.64	2.84 ± 0.16	2.34 ± 0.58	2.83 ± 0.16	1.87 ± 0.50	5
48	28.0 ± 3.9	31.7	4.11 ± 0.19	−5.95 ± 0.93	1.64	2.84 ± 0.16	3.19 ± 0.70	2.84 ± 0.16	2.43 ± 0.58	5
49	36.0 ± 9.6	9.54	4.94 ± 0.17	−3.63 ± 1.2	1.73	2.88 ± 0.17	2.13 ± 1.1	2.85 ± 0.17	2.94 ± 1.1	6
50	40.9 ± 5.7	11.7	4.90 ± 0.17	−4.56 ± 1.0	1.73	2.90 ± 0.17	2.50 ± 1.1	2.88 ± 0.17	3.45 ± 0.94	6

Table D.15: Temperature readings around the loop in °C. $T_\infty = 26\,°C$

#	$T_{a,in}$	$T_{a,out}$	T_{11}	T_{12}	T_{13}	T_{14}	T_{18}	T_{21}	T_{24}	T_{32}	T_{35}
1	24.1	373 ± 3.2	530 ± 4.2	535 ± 4.3	581 ± 4.6	547 ± 4.4	553 ± 4.4	553 ± 4.4	509 ± 4.1	507 ± 4.1	503 ± 4.1
2	24.4	400 ± 3.3	557 ± 4.4	562 ± 4.4	610 ± 4.8	572 ± 4.5	579 ± 4.6	579 ± 4.6	536 ± 4.3	534 ± 4.2	530 ± 4.2
3	24.4	301 ± 2.7	514 ± 4.1	521 ± 4.1	575 ± 4.5	536 ± 4.3	543 ± 4.3	542 ± 4.3	490 ± 3.9	488 ± 3.9	483 ± 3.9
4	24.5	361 ± 3.1	578 ± 4.6	583 ± 4.6	643 ± 5.1	594 ± 4.7	605 ± 4.8	603 ± 4.8	555 ± 4.4	553 ± 4.4	549 ± 4.4
5	24.8	359 ± 3.5	574 ± 4.7	578 ± 4.8	637 ± 5.2	590 ± 4.9	600 ± 4.9	599 ± 4.9	551 ± 4.6	548 ± 4.7	544 ± 4.7
6	24.9	349 ± 3.4	568 ± 4.7	577 ± 4.7	634 ± 5.2	606 ± 5.0	562 ± 4.8	601 ± 4.9	530 ± 4.5	526 ± 4.5	519 ± 4.6
7	24.1	230 ± 3.3	522 ± 4.7	529 ± 4.5	594 ± 4.9	554 ± 4.9	553 ± 4.6	553 ± 4.6	495 ± 4.3	488 ± 4.3	484 ± 4.5
8	24.1	231 ± 2.5	524 ± 4.1	531 ± 4.1	596 ± 4.6	556 ± 4.6	556 ± 4.3	555 ± 4.3	496 ± 3.9	490 ± 3.8	485 ± 3.8
9	24.9	259 ± 3.0	557 ± 4.9	571 ± 4.9	637 ± 5.4	607 ± 5.3	562 ± 4.5	600 ± 5.1	511 ± 4.8	505 ± 4.8	500 ± 5.1
10	24.4	217 ± 3.4	536 ± 4.4	542 ± 4.4	612 ± 4.9	568 ± 4.8	568 ± 4.6	568 ± 4.6	506 ± 4.3	500 ± 4.2	498 ± 4.2
11	25.1	431 ± 5.7	639 ± 5.3	646 ± 5.4	713 ± 5.9	669 ± 5.7	669 ± 5.5	668 ± 5.5	621 ± 5.0	619 ± 5.4	617 ± 5.2
12	24.8	428 ± 4.0	637 ± 5.2	644 ± 5.2	711 ± 5.7	670 ± 5.6	631 ± 5.0	667 ± 5.4	614 ± 5.1	613 ± 5.5	608 ± 5.2
13	25.4	344 ± 2.9	602 ± 4.7	608 ± 4.7	679 ± 5.2	623 ± 5.3	634 ± 4.9	633 ± 4.9	578 ± 4.5	578 ± 4.5	576 ± 4.5
14	25.8	317 ± 3.5	573 ± 4.8	579 ± 4.9	652 ± 5.6	602 ± 5.7	607 ± 5.2	606 ± 5.2	548 ± 5.0	549 ± 4.8	536 ± 4.8
15	25.7	352 ± 3.8	608 ± 5.5	615 ± 5.7	686 ± 6.4	630 ± 6.7	640 ± 5.8	639 ± 5.8	584 ± 5.5	586 ± 5.6	583 ± 5.6
16	25.3	294 ± 2.8	590 ± 4.9	596 ± 4.9	669 ± 5.6	611 ± 5.7	623 ± 5.2	622 ± 5.2	563 ± 4.7	562 ± 4.8	561 ± 4.8
17	25.4	295 ± 3.4	591 ± 5.4	597 ± 5.6	670 ± 6.3	612 ± 7.0	624 ± 5.8	623 ± 5.9	567 ± 5.5	566 ± 5.4	563 ± 5.6
18	25.3	286 ± 3.1	587 ± 5.0	594 ± 5.0	665 ± 5.6	629 ± 5.7	588 ± 5.1	623 ± 5.3	546 ± 4.8	541 ± 4.8	538 ± 4.7
19	24.3	241 ± 3.1	563 ± 4.7	567 ± 4.7	643 ± 5.3	591 ± 5.9	595 ± 4.9	594 ± 4.9	533 ± 4.5	525 ± 4.4	527 ± 4.5
20	26.1	194 ± 2.8	541 ± 4.6	546 ± 4.6	624 ± 5.2	572 ± 5.2	574 ± 4.8	574 ± 4.8	506 ± 4.4	499 ± 4.3	500 ± 4.4
21	26.8	192 ± 2.5	537 ± 4.2	543 ± 4.2	620 ± 4.8	569 ± 4.8	570 ± 4.4	570 ± 4.4	499 ± 4.0	495 ± 3.9	496 ± 3.9
22	27.2	194 ± 2.5	538 ± 4.3	543 ± 4.3	620 ± 4.9	569 ± 5.0	571 ± 4.5	570 ± 4.5	501 ± 4.0	496 ± 3.9	496 ± 4.0
23	27.5	174 ± 2.6	543 ± 4.4	548 ± 4.4	625 ± 5.1	566 ± 5.3	577 ± 4.7	576 ± 4.7	509 ± 4.2	507 ± 4.1	503 ± 4.2
24	27.5	180 ± 2.7	552 ± 4.5	557 ± 4.5	636 ± 5.2	574 ± 5.2	586 ± 4.8	585 ± 4.7	518 ± 4.3	516 ± 4.3	513 ± 4.3
25	24.6	381 ± 3.3	594 ± 4.7	601 ± 4.8	679 ± 5.4	631 ± 5.2	631 ± 5.0	631 ± 5.0	575 ± 4.6	571 ± 4.6	556 ± 4.5
26	25.9	512 ± 7.0	708 ± 7.3	716 ± 7.3	786 ± 7.9	738 ± 7.6	737 ± 7.4	736 ± 7.4	689 ± 7.6	690 ± 7.5	685 ± 7.2
27	24.3	468 ± 3.8	676 ± 5.3	684 ± 5.3	757 ± 5.8	706 ± 5.6	707 ± 5.5	705 ± 5.5	657 ± 5.1	661 ± 5.1	646 ± 5.1
28	25.0	478 ± 6.4	679 ± 6.5	687 ± 6.6	758 ± 7.1	710 ± 6.6	676 ± 6.7	708 ± 6.7	658 ± 6.2	663 ± 6.6	652 ± 7.1
29	25.7	406 ± 3.5	661 ± 5.2	670 ± 5.3	744 ± 5.9	693 ± 5.6	693 ± 5.5	692 ± 5.4	641 ± 5.1	641 ± 5.3	639 ± 5.1
30	24.8	365 ± 3.1	592 ± 4.6	600 ± 4.7	681 ± 5.3	631 ± 5.2	632 ± 4.9	631 ± 4.9	573 ± 4.5	570 ± 4.5	552 ± 4.4
31	24.8	366 ± 3.0	594 ± 4.6	602 ± 4.7	684 ± 5.3	633 ± 5.2	634 ± 4.9	633 ± 4.9	576 ± 4.5	573 ± 4.5	555 ± 4.3
32	25.3	339 ± 3.3	638 ± 5.1	647 ± 5.1	726 ± 5.7	672 ± 5.5	673 ± 5.3	672 ± 5.3	617 ± 4.9	619 ± 4.9	616 ± 4.9
33	25.5	320 ± 3.4	619 ± 5.3	627 ± 5.4	705 ± 6.0	658 ± 5.9	622 ± 5.3	656 ± 5.6	588 ± 5.2	587 ± 5.4	583 ± 5.4
34	25.1	277 ± 2.7	600 ± 4.7	605 ± 4.8	688 ± 5.4	632 ± 5.5	635 ± 5.0	633 ± 5.0	573 ± 4.6	565 ± 4.5	569 ± 4.5
35	27.0	226 ± 3.1	591 ± 5.6	598 ± 5.9	682 ± 6.7	623 ± 8.6	628 ± 6.0	627 ± 5.8	562 ± 5.6	561 ± 5.5	560 ± 5.9
36	27.0	217 ± 2.8	575 ± 4.7	582 ± 4.8	664 ± 5.5	614 ± 5.2	583 ± 4.8	613 ± 5.0	533 ± 4.8	529 ± 5.0	527 ± 4.9
37	29.3	158 ± 2.7	549 ± 4.5	554 ± 4.6	637 ± 5.3	573 ± 5.4	585 ± 4.8	584 ± 4.8	511 ± 5.1	510 ± 4.4	509 ± 4.4
38	29.3	159 ± 2.6	550 ± 4.5	555 ± 4.5	638 ± 5.2	573 ± 5.4	586 ± 4.8	585 ± 4.7	513 ± 4.8	511 ± 4.5	510 ± 4.3
39	29.6	157 ± 2.6	547 ± 4.4	552 ± 4.4	634 ± 5.1	572 ± 5.4	583 ± 4.7	582 ± 4.6	507 ± 4.3	508 ± 4.2	506 ± 4.1
40	24.8	401 ± 3.9	659 ± 5.5	668 ± 5.6	747 ± 6.2	693 ± 5.9	693 ± 5.7	691 ± 5.7	636 ± 5.5	640 ± 5.8	631 ± 5.5
41	27.4	241 ± 3.4	604 ± 5.4	611 ± 5.5	704 ± 6.2	639 ± 6.8	643 ± 5.6	641 ± 5.6	572 ± 5.7	567 ± 5.8	571 ± 5.4
42	27.4	238 ± 2.5	601 ± 4.7	609 ± 4.8	701 ± 5.4	636 ± 6.4	641 ± 5.0	639 ± 5.0	569 ± 4.6	563 ± 4.5	568 ± 4.5
43	27.3	243 ± 2.6	607 ± 4.7	614 ± 4.8	707 ± 5.5	642 ± 6.1	646 ± 5.0	644 ± 5.0	576 ± 4.6	571 ± 4.6	574 ± 4.5
44	29.4	184 ± 2.6	573 ± 4.6	579 ± 4.6	675 ± 5.4	600 ± 6.4	614 ± 4.9	612 ± 4.9	536 ± 4.4	529 ± 4.6	536 ± 4.5
45	29.2	184 ± 2.6	572 ± 4.5	578 ± 4.6	674 ± 5.3	600 ± 6.3	613 ± 4.8	611 ± 4.8	535 ± 4.3	528 ± 4.4	535 ± 4.3
46	29.4	184 ± 2.5	573 ± 4.5	579 ± 4.5	676 ± 5.2	601 ± 6.3	614 ± 4.8	613 ± 4.8	537 ± 4.2	531 ± 4.2	537 ± 4.2
47	31.2	159 ± 2.6	559 ± 4.5	565 ± 4.5	662 ± 5.3	592 ± 6.3	599 ± 4.8	598 ± 4.8	518 ± 4.2	513 ± 4.2	519 ± 4.3
48	33.7	144 ± 2.6	550 ± 4.3	556 ± 4.4	653 ± 5.1	587 ± 5.8	591 ± 4.6	590 ± 4.6	499 ± 4.2	500 ± 4.0	505 ± 4.0
49	26.0	401 ± 3.8	695 ± 5.7	704 ± 5.8	788 ± 6.4	729 ± 6.2	697 ± 5.7	729 ± 6.0	667 ± 5.6	677 ± 5.7	669 ± 5.5
50	26.3	343 ± 3.4	670 ± 5.5	681 ± 5.6	768 ± 6.2	706 ± 6.2	676 ± 5.5	708 ± 5.8	642 ± 5.5	649 ± 5.6	644 ± 5.3

Table D.16: Heat transfer Nu data. Properties at $\overline{T}_s$.

#	Cooler				Bottom Cross				Riser			
	Re	Pr	Gr $1{\cdot}10^3$	Nu	Re	Pr	Gr $1{\cdot}10^3$	Nu	Re	Pr	Gr $1{\cdot}10^3$	Nu
1	79.9	27.1	28.4 ± 3.7	6.42 ± 0.73	77.0	29.0	8.89 ± 3.2	15.4 ± 6.2	84.9	26.2	15.9 ± 3.0	8.89 ± 1.9
2	120	23.3	51.5 ± 5.5	5.91 ± 0.98	113	24.7	12.6 ± 4.6	16.3 ± 6.6	123	22.6	22.9 ± 4.3	9.41 ± 2.1
3	68.6	29.5	13.5 ± 1.6	9.21 ± 1.0	72.7	32.2	10.3 ± 2.5	12.0 ± 3.5	81.9	28.5	16.7 ± 2.5	7.96 ± 1.5
4	134	20.7	78.0 ± 7.2	6.36 ± 0.91	126	22.2	23.2 ± 6.0	12.9 ± 3.9	137	20.3	38.3 ± 5.4	8.41 ± 1.6
5	131	21.2	76.4 ± 16	6.05 ± 2.0	123	22.7	21.5 ± 5.9	13.3 ± 4.2	134	20.7	35.7 ± 5.4	8.68 ± 1.7
6	93.1	23.7	49.4 ± 5.9	7.50 ± 1.3	89.7	24.6	29.1 ± 4.8	8.45 ± 1.8	105	20.9	36.1 ± 5.2	7.82 ± 1.4
7	66.2	28.4	12.7 ± 1.8	10.1 ± 1.1	75.5	31.3	22.0 ± 2.8	7.07 ± 1.3	86.4	27.2	27.0 ± 2.9	6.78 ± 1.1
8	67.6	28.1	13.9 ± 1.7	9.92 ± 1.1	76.3	30.9	22.8 ± 2.7	6.93 ± 1.2	87.2	26.9	27.9 ± 2.7	6.70 ± 1.0
9	75.6	25.0	34.2 ± 3.6	8.41 ± 0.90	71.5	26.8	34.0 ± 4.2	6.58 ± 1.2	88.0	21.6	39.7 ± 5.0	6.90 ± 1.1
10	87.3	26.3	19.4 ± 2.5	9.24 ± 1.00	92.2	28.9	29.1 ± 3.3	6.72 ± 1.1	105	25.2	34.8 ± 3.3	6.71 ± 1.0
11	301	15.1	145 ± 29	7.92 ± 2.7	282	16.2	50.4 ± 13	12.5 ± 3.7	304	15.0	81.7 ± 11	7.74 ± 1.4
12	256	16.1	117 ± 14	8.65 ± 1.6	244	16.5	78.1 ± 11	7.66 ± 1.5	265	15.1	84.9 ± 11	7.51 ± 1.3
13	202	18.1	111 ± 11	7.32 ± 1.1	186	19.5	38.7 ± 7.9	11.4 ± 2.8	203	17.8	61.2 ± 7.1	7.67 ± 1.3
14	175	21.0	84.6 ± 15	6.44 ± 2.5	160	23.0	29.3 ± 6.1	11.0 ± 2.8	177	20.7	47.8 ± 5.6	7.46 ± 1.3
15	208	17.5	120 ± 14	7.37 ± 1.2	192	18.9	41.4 ± 10	11.3 ± 3.3	209	17.3	65.5 ± 9.1	7.55 ± 1.4
16	206	19.3	111 ± 10	6.65 ± 0.83	190	21.0	36.8 ± 7.2	10.4 ± 2.5	209	19.0	57.4 ± 6.7	7.33 ± 1.2
17	208	19.1	112 ± 11	6.75 ± 0.86	192	20.7	37.0 ± 8.3	10.6 ± 2.9	210	18.9	58.1 ± 7.5	7.31 ± 1.3
18	128	21.2	81.8 ± 8.2	6.87 ± 1.8	114	22.3	50.3 ± 6.2	6.75 ± 1.2	132	19.1	55.9 ± 6.6	7.31 ± 1.2
19	121	22.7	49.4 ± 4.6	7.71 ± 0.80	121	24.7	43.6 ± 4.8	6.43 ± 1.1	136	21.9	49.5 ± 4.7	6.70 ± 1.0
20	91.1	25.8	21.2 ± 2.6	10.0 ± 1.1	102	28.4	34.6 ± 3.6	6.21 ± 1.0	117	24.6	40.2 ± 3.6	6.58 ± 0.99
21	89.3	26.5	19.2 ± 2.3	10.7 ± 1.1	99.2	29.1	31.5 ± 3.2	6.51 ± 1.0	114	25.1	37.0 ± 3.3	6.86 ± 1.0
22	90.2	26.4	20.0 ± 2.3	10.7 ± 1.1	99.7	29.0	30.4 ± 3.3	6.80 ± 1.1	115	25.1	36.5 ± 3.3	6.97 ± 1.1
23	127	25.3	19.3 ± 2.6	9.59 ± 1.0	149	27.8	24.1 ± 3.8	9.28 ± 1.9	169	24.4	37.1 ± 3.7	7.17 ± 1.1
24	140	24.0	27.8 ± 4.0	9.04 ± 0.94	157	26.4	27.8 ± 4.3	8.85 ± 1.8	177	23.2	42.4 ± 4.1	6.85 ± 1.1
25	115	18.6	94.7 ± 8.8	7.14 ± 0.98	105	20.4	57.8 ± 7.1	7.45 ± 1.3	116	18.4	67.6 ± 6.7	7.01 ± 1.1
26	483	12.0	260 ± 36	9.42 ± 1.9	459	12.0	97.8 ± 30	12.8 ± 4.5	489	11.2	155 ± 26	8.00 ± 1.7
27	404	12.9	205 ± 32	8.57 ± 1.7	381	13.7	113 ± 17	8.62 ± 1.7	410	12.7	133 ± 15	7.56 ± 1.2
28	443	13.2	172 ± 20	9.86 ± 1.7	449	13.6	118 ± 20	8.42 ± 1.9	482	12.6	128 ± 19	7.96 ± 1.5
29	371	13.7	190 ± 19	9.11 ± 1.4	348	14.7	75.4 ± 15	11.4 ± 2.8	376	13.5	115 ± 14	7.54 ± 1.3
30	146	18.7	97.0 ± 8.5	7.26 ± 0.99	133	20.7	59.4 ± 6.9	7.60 ± 1.3	147	18.6	69.9 ± 6.5	7.15 ± 1.1
31	148	18.5	101 ± 10	7.17 ± 0.97	135	20.4	60.7 ± 7.0	7.61 ± 1.3	149	18.4	71.7 ± 6.6	7.10 ± 1.1
32	308	15.0	170 ± 12	8.66 ± 1.1	287	16.3	66.5 ± 12	10.6 ± 2.5	312	14.9	102 ± 11	7.14 ± 1.1
33	237	17.5	118 ± 13	8.58 ± 1.3	197	18.3	78.4 ± 9.7	7.17 ± 1.3	221	16.3	85.0 ± 9.5	7.42 ± 1.2
34	198	18.4	124 ± 9.9	7.44 ± 0.97	171	20.1	68.1 ± 7.4	7.00 ± 1.2	189	18.1	78.5 ± 6.9	6.89 ± 1.0
35	241	19.1	104 ± 9.5	7.12 ± 0.74	230	21.0	46.2 ± 8.6	9.46 ± 2.2	255	18.8	69.9 ± 8.0	6.97 ± 1.2
36	140	22.3	53.8 ± 5.0	8.66 ± 0.90	137	23.8	51.7 ± 5.4	6.64 ± 1.1	160	20.3	57.7 ± 5.6	7.33 ± 1.1
37	134	24.5	22.1 ± 3.2	9.57 ± 1.0	157	27.1	28.3 ± 4.2	9.56 ± 1.9	179	23.5	43.0 ± 4.1	7.59 ± 1.2
38	135	24.4	22.7 ± 3.1	9.49 ± 1.0	158	26.9	28.6 ± 4.2	9.55 ± 1.9	180	23.4	43.5 ± 4.1	7.56 ± 1.2
39	131	24.8	20.3 ± 2.8	9.77 ± 1.0	155	27.5	27.3 ± 3.9	9.62 ± 1.9	177	23.8	41.6 ± 3.9	7.68 ± 1.2
40	297	13.8	184 ± 21	9.31 ± 1.6	256	14.9	107 ± 15	8.34 ± 1.6	278	13.6	126 ± 14	7.48 ± 1.2
41	244	18.0	145 ± 9.4	7.07 ± 0.72	223	19.8	84.4 ± 8.5	6.51 ± 1.0	250	17.6	94.0 ± 8.3	6.78 ± 1.0
42	241	18.3	138 ± 7.7	7.15 ± 0.72	220	20.1	81.1 ± 7.4	6.59 ± 1.0	247	17.8	90.8 ± 7.1	6.85 ± 0.97
43	248	17.7	153 ± 9.0	6.99 ± 1.4	227	19.5	87.8 ± 7.9	6.44 ± 0.97	254	17.3	97.3 ± 7.6	6.71 ± 0.95
44	150	21.2	60.1 ± 5.6	8.91 ± 0.92	150	23.7	60.5 ± 5.5	6.45 ± 0.97	171	20.6	69.6 ± 5.4	6.83 ± 0.96
45	148	21.4	58.3 ± 5.4	8.94 ± 0.92	149	23.8	59.7 ± 5.3	6.47 ± 0.96	170	20.7	68.8 ± 5.2	6.86 ± 0.96
46	151	21.2	61.3 ± 5.6	8.91 ± 0.92	150	23.6	61.1 ± 5.3	6.43 ± 0.95	171	20.6	70.0 ± 5.2	6.81 ± 0.95
47	123	23.1	38.1 ± 4.3	10.2 ± 1.1	129	25.8	54.0 ± 4.6	6.10 ± 0.89	148	22.3	61.7 ± 4.6	6.70 ± 0.93
48	137	24.7	28.1 ± 3.6	11.4 ± 1.2	141	27.7	48.7 ± 3.9	5.93 ± 0.84	166	23.3	56.3 ± 4.0	6.73 ± 0.92
49	417	12.3	220 ± 22	12.1 ± 1.8	411	12.8	161 ± 21	8.24 ± 1.5	445	11.8	174 ± 19	7.93 ± 1.3
50	428	13.6	198 ± 19	11.0 ± 1.6	410	14.2	138 ± 17	7.85 ± 1.4	451	12.9	150 ± 16	7.64 ± 1.2

D.6 Heat Transfer Data Campaigns 7 - 10

Table D.17: Heat balance data in k*W*.

#	$\dot{m}_s$	$\dot{m}_a$	V_{Htr}	Bottom Cross			Riser			C#
	g/s	g/s	V	A_{htr} A	Q_{ext}	ΔQ_s	A_{htr} A	Q_{ext}	ΔQ_s	
1	14.4 ± 1.4	3.40 ± 0.0995	19.2	49.3 ± 2.6	0.855 ± 0.050	0.624 ± 0.065	50.1 ± 2.7	0.870 ± 0.051	1.11 ± 0.12	7
2	14.4 ± 1.4	3.25 ± 0.119	19.2	49.3 ± 2.6	0.854 ± 0.050	0.617 ± 0.10	50.1 ± 2.7	0.870 ± 0.051	1.10 ± 0.12	7
3	24.6 ± 2.3	3.37 ± 0.104	24.0	61.6 ± 3.3	1.39 ± 0.078	1.02 ± 0.10	62.7 ± 3.3	1.41 ± 0.080	1.72 ± 0.17	7
4	24.6 ± 2.3	3.26 ± 0.131	24.0	61.6 ± 3.3	1.39 ± 0.078	1.02 ± 0.10	63.2 ± 3.3	1.42 ± 0.080	1.76 ± 0.18	7
5	35.2 ± 4.9	3.13 ± 0.102	30.0	77.4 ± 4.1	2.23 ± 0.12	2.02 ± 0.30	78.9 ± 4.2	2.27 ± 0.13	3.35 ± 0.48	7
6	41.8 ± 5.7	3.17 ± 0.102	34.0	87.7 ± 4.6	2.88 ± 0.16	3.07 ± 0.46	90.7 ± 4.8	2.98 ± 0.16	4.45 ± 0.63	7
7	31.4 ± 5.4	3.35 ± 0.106	30.0	77.5 ± 4.1	2.24 ± 0.12	2.03 ± 0.36	80.3 ± 4.2	2.31 ± 0.13	3.29 ± 0.58	7
8	27.7 ± 6.4	3.42 ± 0.150	24.0	62.0 ± 3.3	1.40 ± 0.079	1.42 ± 0.34	63.8 ± 3.4	1.44 ± 0.081	1.96 ± 0.46	8
9	28.4 ± 8.6	3.40 ± 0.127	26.0	67.2 ± 3.6	1.65 ± 0.092	1.75 ± 0.53	69.1 ± 3.7	1.70 ± 0.095	2.15 ± 0.65	8
10	28.4 ± 8.6	3.53 ± 0.108	26.0	67.1 ± 3.6	1.65 ± 0.092	1.69 ± 0.51	69.1 ± 3.7	1.70 ± 0.095	2.19 ± 0.66	8
11	37.6 ± 12	3.53 ± 0.107	28.0	72.3 ± 3.8	1.93 ± 0.11	2.41 ± 0.77	74.3 ± 3.9	1.98 ± 0.11	2.98 ± 0.95	8
12	31.7 ± 11	3.50 ± 0.106	30.0	77.4 ± 4.1	2.22 ± 0.12	2.16 ± 0.75	79.6 ± 4.2	2.28 ± 0.13	2.42 ± 0.84	8
13	37.3 ± 7.0	3.38 ± 0.285	30.0	77.4 ± 4.1	2.21 ± 0.12	2.37 ± 0.45	79.6 ± 4.2	2.28 ± 0.13	2.47 ± 0.47	8
14	26.4 ± 5.2	3.53 ± 0.106	26.0	67.3 ± 3.6	1.67 ± 0.093	1.90 ± 0.38	69.2 ± 3.7	1.71 ± 0.095	2.43 ± 0.49	8
15	35.8 ± 6.4	3.42 ± 0.132	34.0	87.7 ± 4.6	2.87 ± 0.16	2.83 ± 0.52	90.2 ± 4.8	2.95 ± 0.16	2.60 ± 0.47	8
16	22.7 ± 8.2	3.27 ± 0.105	22.0	58.4 ± 3.1	1.19 ± 0.068	0.895 ± 0.33	57.6 ± 3.0	1.16 ± 0.067	1.72 ± 0.63	10
17	36.4 ± 5.1	3.30 ± 0.0856	30.0	80.7 ± 4.3	2.30 ± 0.13	2.54 ± 0.37	78.0 ± 4.1	2.20 ± 0.12	2.39 ± 0.35	10
18	32.2 ± 5.4	3.16 ± 0.0851	28.0	75.5 ± 4.0	2.01 ± 0.11	1.95 ± 0.34	73.0 ± 3.9	1.92 ± 0.11	2.64 ± 0.45	10
19	33.5 ± 5.7	3.15 ± 0.0837	30.0	80.8 ± 4.3	2.31 ± 0.13	2.31 ± 0.41	78.2 ± 4.1	2.21 ± 0.12	2.55 ± 0.44	10
20	33.3 ± 6.6	3.07 ± 0.0792	30.0	80.9 ± 4.3	2.32 ± 0.13	2.31 ± 0.46	78.3 ± 4.1	2.22 ± 0.12	2.87 ± 0.58	10
21	36.6 ± 7.5	3.01 ± 0.0749	34.0	91.7 ± 4.9	3.00 ± 0.16	2.96 ± 0.62	88.6 ± 4.7	2.87 ± 0.16	3.21 ± 0.67	10
22	35.3 ± 4.9	3.05 ± 0.0757	34.0	91.8 ± 4.9	3.00 ± 0.17	2.92 ± 0.42	88.7 ± 4.7	2.87 ± 0.16	2.89 ± 0.42	10
23	42.0 ± 7.4	3.09 ± 0.0768	34.0	91.9 ± 4.9	3.00 ± 0.17	3.60 ± 0.64	88.7 ± 4.7	2.87 ± 0.16	3.14 ± 0.56	10
24	43.0 ± 5.9	3.03 ± 0.0865	36.9	98.0 ± 5.2	3.41 ± 0.19	3.80 ± 0.54	98.0 ± 5.2	3.52 ± 0.21	3.39 ± 0.48	10
25	42.2 ± 7.2	3.10 ± 0.0828	36.8	98.0 ± 5.2	3.41 ± 0.19	3.92 ± 0.70	98.0 ± 5.2	3.52 ± 0.19	3.46 ± 0.61	10
26	40.4 ± 5.6	3.08 ± 0.0770	36.8	98.0 ± 5.2	3.41 ± 0.19	3.60 ± 0.54	98.0 ± 5.2	3.52 ± 0.19	3.51 ± 0.52	10
27	38.8 ± 16	3.01 ± 0.0922	40.0	109 ± 5.7	4.22 ± 0.23	5.18 ± 2.1	104 ± 5.5	4.02 ± 0.22	5.59 ± 2.3	10
28	38.9 ± 16	3.02 ± 0.0763	40.0	109 ± 5.7	4.22 ± 0.23	5.36 ± 2.2	104 ± 5.5	4.02 ± 0.22	5.44 ± 2.2	10
29	42.0 ± 7.4	3.38 ± 0.0781	34.0	92.5 ± 4.9	3.02 ± 0.17	3.36 ± 0.60	88.9 ± 4.7	2.87 ± 0.16	3.05 ± 0.55	10
30	43.6 ± 8.4	3.22 ± 0.0916	36.0	97.8 ± 5.2	3.39 ± 0.19	4.15 ± 0.83	94.0 ± 5.0	3.22 ± 0.18	3.08 ± 0.62	10
31	42.2 ± 8.9	3.11 ± 0.0827	34.0	92.6 ± 4.9	3.02 ± 0.17	3.67 ± 0.82	88.8 ± 4.7	2.87 ± 0.16	2.85 ± 0.64	10
32	39.8 ± 5.8	3.09 ± 0.0965	32.0	87.6 ± 4.6	2.69 ± 0.15	3.17 ± 0.49	83.7 ± 4.4	2.54 ± 0.14	2.91 ± 0.45	10

Table D.18: Temperature readings around the loop in °C.

									Bottom Cross			Riser						
#	T_{11}	T_{12}	T_{14}	T_{18}	T_{21}	T_{24}	T_{32}	T_{35}	$T_{s,BC,in}$	$\bar{T}_{w,o,BC}$	$\bar{T}_{s,BC}$	$\bar{T}_{w,o,R}$	$\bar{T}_{s,R}$	$T_{s,R,out}$	$T_{a,in}$	± 2.2	$T_{a,out}$	T_∞
1	583 ± 5.0	603 ± 5.1	620 ± 5.3	614 ± 5.2	603 ± 5.1	594 ± 5.1	591 ± 5.1	565 ± 4.9	565 ± 0.14	588 ± 4.8	574 ± 0.087	620 ± 5.2	600 ± 0.10	616 ± 0.52	23.4	± 2.2	438	24.6
2	585 ± 5.0	604 ± 5.2	622 ± 5.3	616 ± 5.2	604 ± 5.2	595 ± 5.1	593 ± 5.6	567 ± 5.4	567 ± 2.4	590 ± 5.2	576 ± 1.2	621 ± 5.6	601 ± 0.26	617 ± 0.84	23.3	± 2.2	441	24.3
3	581 ± 5.0	595 ± 5.1	606 ± 5.2	614 ± 5.2	595 ± 5.1	570 ± 4.9	570 ± 4.9	564 ± 4.9	564 ± 0.089	590 ± 4.8	573 ± 0.072	628 ± 5.5	596 ± 0.11	611 ± 0.44	24.0	± 2.2	436	24.9
4	583 ± 5.0	597 ± 5.1	609 ± 5.3	616 ± 5.2	597 ± 5.1	571 ± 5.0	572 ± 5.0	566 ± 4.9	566 ± 0.34	592 ± 4.8	574 ± 0.25	629 ± 5.5	598 ± 0.29	613 ± 1.3	24.0	± 2.2	438	25.0
5	592 ± 5.1	605 ± 5.2	631 ± 5.5	633 ± 5.4	605 ± 5.2	568 ± 5.1	574 ± 5.1	568 ± 5.0	568 ± 0.91	609 ± 5.5	580 ± 0.55	659 ± 6.4	612 ± 0.41	632 ± 1.4	26.3	± 2.2	254	25.6
6	604 ± 5.2	614 ± 5.3	647 ± 5.7	650 ± 5.5	614 ± 5.3	571 ± 5.4	579 ± 5.1	573 ± 5.1	573 ± 1.3	626 ± 6.2	588 ± 0.80	684 ± 7.3	626 ± 0.58	648 ± 1.7	31.6	± 2.2	189	26.1
7	565 ± 4.9	580 ± 5.0	608 ± 5.4	610 ± 5.2	580 ± 5.0	542 ± 4.8	543 ± 4.8	538 ± 4.8	538 ± 0.89	582 ± 5.4	551 ± 0.57	635 ± 6.4	587 ± 0.45	609 ± 1.4	27.8	± 2.2	204	25.5
8	587 ± 5.1	599 ± 5.1	617 ± 5.4	617 ± 5.3	599 ± 5.1	577 ± 5.0	574 ± 5.0	565 ± 4.9	565 ± 0.58	595 ± 4.8	576 ± 0.34	631 ± 5.4	602 ± 0.28	617 ± 1.2	25.1	± 2.2	444	26.5
9	593 ± 5.1	604 ± 5.2	623 ± 5.6	626 ± 5.3	604 ± 5.2	579 ± 5.0	577 ± 5.1	567 ± 5.0	567 ± 0.82	603 ± 5.0	580 ± 0.47	643 ± 5.7	609 ± 0.41	624 ± 2.0	24.8	± 2.2	393	25.7
10	590 ± 5.1	602 ± 5.1	622 ± 5.4	623 ± 5.3	602 ± 5.1	576 ± 5.0	574 ± 5.0	565 ± 4.9	565 ± 0.65	601 ± 4.9	578 ± 0.33	641 ± 5.7	606 ± 0.22	623 ± 1.3	24.6	± 2.2	388	25.6
11	607 ± 5.2	617 ± 5.2	640 ± 5.6	641 ± 5.4	617 ± 5.2	590 ± 5.1	591 ± 5.1	580 ± 5.0	580 ± 0.34	619 ± 5.1	594 ± 0.19	663 ± 6.0	624 ± 0.26	641 ± 1.4	24.9	± 2.2	357	25.7
12	633 ± 5.4	639 ± 5.4	665 ± 5.8	666 ± 5.6	639 ± 5.4	610 ± 5.2	615 ± 5.2	605 ± 5.2	605 ± 0.36	645 ± 5.6	619 ± 0.25	692 ± 6.4	649 ± 0.33	665 ± 1.6	25.4	± 2.2	340	26.2
13	664 ± 5.6	668 ± 5.6	692 ± 5.9	693 ± 5.8	668 ± 5.6	641 ± 5.4	643 ± 5.5	638 ± 5.4	638 ± 0.51	675 ± 5.5	651 ± 0.35	718 ± 6.4	678 ± 0.35	692 ± 1.4	26.6	± 2.2	410	28.5
14	533 ± 4.7	550 ± 4.8	570 ± 5.2	573 ± 5.0	550 ± 4.8	517 ± 4.6	512 ± 4.6	503 ± 4.5	503 ± 0.40	545 ± 4.6	518 ± 0.21	591 ± 5.4	552 ± 0.29	572 ± 1.6	25.0	± 2.2	258	25.4
15	677 ± 5.6	678 ± 5.7	706 ± 6.0	708 ± 5.9	678 ± 5.7	645 ± 5.4	648 ± 5.6	643 ± 5.4	643 ± 0.40	691 ± 5.9	660 ± 0.24	741 ± 6.9	692 ± 0.25	707 ± 1.2	29.6	± 2.2	293	29.6
16	518 ± 4.6	536 ± 4.7	547 ± 5.0	552 ± 4.8	552 ± 4.8	510 ± 4.6	507 ± 4.5	502 ± 4.5	502 ± 0.40	532 ± 4.9	510 ± 0.25	572 ± 6.0	534 ± 0.28	550 ± 1.3	24.1	± 2.2	377	24.8
17	632 ± 5.4	639 ± 5.4	655 ± 6.0	664 ± 5.6	661 ± 5.6	606 ± 5.2	605 ± 5.2	603 ± 5.2	603 ± 0.44	654 ± 6.1	618 ± 0.31	703 ± 6.7	646 ± 0.49	660 ± 2.5	25.2	± 2.2	341	25.2
18	560 ± 4.9	575 ± 5.0	585 ± 5.1	599 ± 5.1	598 ± 5.2	538 ± 4.8	538 ± 4.8	534 ± 4.7	535 ± 0.60	584 ± 5.6	547 ± 0.43	633 ± 6.1	577 ± 0.34	594 ± 0.49	25.2	± 2.2	254	24.7
19	591 ± 5.1	602 ± 5.2	613 ± 5.3	629 ± 5.4	625 ± 5.4	565 ± 5.2	565 ± 5.0	562 ± 4.9	562 ± 0.69	617 ± 5.9	576 ± 0.48	668 ± 6.5	607 ± 0.39	623 ± 0.67	26.0	± 2.2	251	25.2
20	563 ± 4.9	578 ± 5.0	589 ± 5.1	606 ± 5.2	603 ± 5.2	537 ± 4.7	538 ± 4.7	534 ± 4.7	534 ± 0.25	591 ± 5.8	549 ± 0.19	645 ± 6.4	581 ± 0.19	599 ± 0.40	27.5	± 2.2	197	25.8
21	614 ± 5.2	621 ± 5.3	649 ± 5.8	652 ± 5.5	651 ± 5.5	578 ± 5.3	579 ± 5.1	580 ± 5.0	580 ± 0.26	646 ± 6.5	597 ± 0.19	705 ± 7.2	633 ± 0.38	651 ± 2.0	31.3	± 2.2	184	26.8
22	633 ± 5.4	637 ± 5.4	666 ± 5.9	668 ± 5.6	666 ± 5.6	598 ± 5.2	599 ± 5.2	598 ± 5.1	598 ± 0.47	664 ± 6.6	615 ± 0.30	720 ± 7.3	650 ± 0.37	667 ± 1.8	29.2	± 2.2	212	26.2
23	654 ± 5.5	658 ± 5.5	686 ± 5.8	687 ± 5.7	685 ± 5.7	622 ± 5.3	625 ± 5.4	618 ± 5.3	619 ± 0.42	684 ± 6.7	637 ± 0.26	738 ± 7.4	670 ± 0.27	686 ± 1.1	27.6	± 2.2	253	26.1
24	692 ± 5.7	696 ± 5.8	724 ± 6.4	726 ± 6.0	724 ± 6.0	656 ± 6.1	662 ± 5.6	655 ± 5.5	655 ± 0.32	725 ± 7.2	673 ± 0.21	792 ± 9.3	708 ± 0.43	725 ± 2.4	29.8	± 2.2	254	27.4
25	669 ± 5.7	673 ± 5.7	703 ± 6.1	705 ± 5.9	703 ± 5.9	629 ± 5.8	637 ± 5.8	630 ± 5.5	631 ± 1.5	703 ± 7.2	650 ± 0.94	767 ± 8.0	687 ± 0.68	704 ± 1.7	32.1	± 2.2	223	27.6
26	650 ± 5.6	654 ± 5.6	686 ± 6.0	687 ± 5.8	686 ± 5.8	608 ± 5.6	620 ± 6.5	613 ± 5.4	613 ± 1.3	685 ± 7.1	631 ± 0.86	750 ± 7.9	668 ± 0.71	686 ± 1.9	35.9	± 2.2	200	29.1
27	654 ± 6.0	673 ± 6.1	715 ± 6.5	716 ± 6.3	713 ± 6.3	656 ± 5.7	652 ± 5.8	598 ± 6.6	598 ± 4.1	695 ± 8.4	626 ± 2.4	776 ± 8.2	685 ± 1.4	715 ± 2.6	31.9	± 2.2	396	32.1
28	652 ± 5.5	669 ± 5.6	710 ± 6.0	711 ± 5.9	709 ± 5.9	651 ± 5.5	647 ± 5.5	594 ± 6.1	594 ± 3.4	694 ± 8.2	623 ± 1.7	773 ± 8.1	681 ± 0.37	710 ± 1.4	29.9	± 2.2	356	28.6
29	653 ± 5.5	657 ± 5.5	682 ± 6.1	685 ± 5.7	683 ± 5.7	621 ± 5.3	621 ± 5.3	619 ± 5.3	619 ± 0.31	682 ± 6.8	636 ± 0.19	737 ± 7.3	668 ± 0.37	683 ± 2.1	29.7	± 2.2	256	29.2
30	683 ± 5.8	686 ± 5.8	712 ± 6.2	714 ± 6.0	712 ± 6.0	644 ± 5.6	652 ± 5.8	643 ± 5.6	643 ± 1.5	715 ± 7.3	663 ± 0.97	772 ± 7.8	698 ± 0.78	713 ± 2.1	29.9	± 2.2	265	29.0
31	669 ± 5.9	672 ± 5.9	696 ± 6.4	699 ± 6.0	697 ± 6.0	633 ± 5.6	639 ± 5.7	632 ± 5.6	632 ± 1.8	698 ± 7.1	651 ± 1.3	751 ± 7.5	683 ± 1.1	697 ± 2.8	27.9	± 2.2	293	27.7
32	625 ± 5.3	631 ± 5.4	650 ± 6.3	659 ± 5.5	657 ± 5.6	594 ± 5.2	593 ± 5.4	591 ± 5.2	591 ± 1.2	653 ± 6.5	608 ± 0.73	704 ± 6.9	640 ± 0.68	655 ± 3.2	27.6	± 2.2	260	27.2

Table D.19: Heat transfer Nu data. Properties at $\overline{T}_s$.

#	Bottom Cross					Riser				
	Re	Pr	Gr $1{\cdot}10^3$	Gr* $1{\cdot}10^3$	Nu	Re	Pr	Gr $1{\cdot}10^3$	Gr* $1{\cdot}10^3$	Nu
1	97.5 ± 22	21.1 ± 4.8	8.89 ± 5.0	127 ± 54	14.3 ± 6.1	110 ± 25	18.6 ± 4.2	17.6 ± 8.7	172 ± 73	9.75 ± 3.0
2	98.5 ± 22	20.9 ± 4.7	9.11 ± 5.4	130 ± 55	14.3 ± 6.7	111 ± 25	18.4 ± 4.2	17.9 ± 9.0	175 ± 74	9.77 ± 3.2
3	165 ± 37	21.3 ± 4.8	11.1 ± 5.7	203 ± 86	18.3 ± 6.2	185 ± 41	18.9 ± 4.3	26.6 ± 12	270 ± 110	10.1 ± 2.2
4	166 ± 37	21.1 ± 4.8	11.2 ± 5.8	207 ± 88	18.5 ± 6.3	186 ± 41	18.7 ± 4.2	26.7 ± 12	277 ± 120	10.4 ± 2.3
5	244 ± 60	20.5 ± 4.6	19.7 ± 9.1	350 ± 150	17.8 ± 4.5	284 ± 70	17.5 ± 4.0	46.5 ± 20	503 ± 210	10.8 ± 2.0
6	303 ± 74	19.7 ± 4.4	28.0 ± 13	494 ± 210	17.6 ± 3.9	360 ± 88	16.4 ± 3.7	64.3 ± 28	752 ± 320	11.7 ± 2.1
7	187 ± 50	23.9 ± 5.4	15.9 ± 7.2	261 ± 110	16.4 ± 3.8	224 ± 59	19.8 ± 4.5	36.8 ± 16	403 ± 170	11.0 ± 2.0
8	189 ± 58	20.9 ± 4.7	12.2 ± 6.1	212 ± 90	17.3 ± 5.6	213 ± 66	18.4 ± 4.2	25.9 ± 12	290 ± 120	11.2 ± 2.6
9	197 ± 72	20.6 ± 4.6	15.8 ± 7.5	260 ± 110	16.5 ± 4.5	226 ± 82	17.8 ± 4.0	32.9 ± 15	365 ± 160	11.1 ± 2.4
10	195 ± 71	20.8 ± 4.7	15.4 ± 7.3	255 ± 110	16.6 ± 4.5	224 ± 81	18.0 ± 4.1	32.1 ± 14	358 ± 150	11.1 ± 2.4
11	280 ± 110	19.1 ± 4.3	19.6 ± 9.2	348 ± 150	17.8 ± 4.7	321 ± 120	16.6 ± 3.7	42.7 ± 19	491 ± 210	11.5 ± 2.3
12	267 ± 110	16.9 ± 3.8	26.1 ± 12	509 ± 220	19.5 ± 5.3	304 ± 120	14.8 ± 3.3	57.4 ± 25	707 ± 300	12.3 ± 2.5
13	364 ± 100	14.6 ± 3.3	30.4 ± 15	675 ± 290	22.2 ± 6.7	406 ± 110	13.0 ± 2.9	67.6 ± 30	898 ± 380	13.3 ± 2.8
14	130 ± 37	29.0 ± 6.5	9.58 ± 4.3	134 ± 57	14.0 ± 3.1	157 ± 44	23.8 ± 5.4	20.6 ± 9.0	209 ± 89	10.2 ± 2.0
15	363 ± 98	14.1 ± 3.2	43.7 ± 20	944 ± 400	21.6 ± 5.3	411 ± 110	12.3 ± 2.8	94.2 ± 41	1290 ± 550	13.8 ± 2.6
16	107 ± 44	30.4 ± 6.9	7.14 ± 3.4	87.9 ± 37	12.3 ± 3.4	122 ± 51	26.3 ± 5.9	17.0 ± 7.5	115 ± 49	6.78 ± 1.4
17	305 ± 75	17.0 ± 3.8	37.0 ± 17	527 ± 220	14.3 ± 3.1	345 ± 85	15.0 ± 3.4	77.0 ± 33	660 ± 280	8.57 ± 1.5
18	188 ± 49	24.5 ± 5.5	18.4 ± 8.1	227 ± 96	12.3 ± 2.5	219 ± 57	20.9 ± 4.7	39.4 ± 17	302 ± 130	7.66 ± 1.3
19	228 ± 60	20.9 ± 4.7	27.4 ± 12	354 ± 150	12.9 ± 2.6	264 ± 70	18.0 ± 4.1	58.2 ± 25	465 ± 200	7.99 ± 1.3
20	196 ± 55	24.3 ± 5.5	21.8 ± 9.5	266 ± 110	12.2 ± 2.3	231 ± 65	20.4 ± 4.6	46.8 ± 20	365 ± 160	7.80 ± 1.2
21	277 ± 80	18.8 ± 4.2	41.0 ± 18	566 ± 240	13.8 ± 2.6	325 ± 94	15.9 ± 3.6	86.3 ± 36	767 ± 330	8.88 ± 1.4
22	292 ± 72	17.2 ± 3.9	47.7 ± 21	672 ± 290	14.1 ± 2.7	339 ± 83	14.7 ± 3.3	97.4 ± 41	890 ± 380	9.14 ± 1.5
23	383 ± 100	15.6 ± 3.5	56.8 ± 25	813 ± 350	14.3 ± 2.8	440 ± 120	13.5 ± 3.0	111 ± 47	1050 ± 450	9.50 ± 1.6
24	460 ± 110	13.3 ± 3.0	83.9 ± 37	1260 ± 540	15.0 ± 2.9	525 ± 130	11.6 ± 2.6	185 ± 79	1740 ± 740	9.41 ± 1.6
25	409 ± 110	14.7 ± 3.3	70.7 ± 31	1040 ± 440	14.7 ± 2.8	473 ± 120	12.6 ± 2.8	150 ± 63	1480 ± 630	9.84 ± 1.6
26	360 ± 88	16.0 ± 3.6	61.0 ± 26	883 ± 370	14.5 ± 2.7	420 ± 100	13.6 ± 3.1	132 ± 56	1270 ± 540	9.63 ± 1.5
27	337 ± 150	16.4 ± 3.7	75.5 ± 32	1040 ± 440	13.8 ± 2.5	428 ± 190	12.7 ± 2.9	168 ± 70	1660 ± 700	9.89 ± 1.5
28	332 ± 150	16.6 ± 3.8	75.6 ± 32	1010 ± 430	13.4 ± 2.3	423 ± 190	12.9 ± 2.9	164 ± 69	1610 ± 680	9.83 ± 1.5
29	382 ± 100	15.7 ± 3.5	55.3 ± 24	814 ± 350	14.7 ± 2.9	436 ± 120	13.6 ± 3.1	111 ± 47	1040 ± 440	9.32 ± 1.5
30	447 ± 120	13.9 ± 3.1	78.4 ± 34	1150 ± 490	14.7 ± 2.9	512 ± 140	12.0 ± 2.7	151 ± 64	1480 ± 630	9.75 ± 1.6
31	410 ± 120	14.7 ± 3.3	63.8 ± 28	926 ± 390	14.5 ± 3.0	467 ± 140	12.8 ± 2.9	124 ± 53	1170 ± 500	9.47 ± 1.6
32	317 ± 79	17.9 ± 4.0	42.3 ± 18	560 ± 240	13.3 ± 2.6	366 ± 91	15.4 ± 3.5	82.2 ± 35	722 ± 310	8.78 ± 1.4

INDEX

COLOPHON

This document was typeset using Gyre Pagella by pdfLaTeX 2_ε. The layout is in accordance with the rules of the Wisconsin Dissertation Template, by Will Benton as modified by Steven Baumgart. Reference are handled using biber.